

Observing and Modeling Arctic Clouds: Exploring the Connections Between Cloud
Phase, Precipitation, and Surface Radiation

By
Elin A. McILHATTAN

A dissertation submitted in partial fulfillment of
the requirements for the degree of

Doctor of Philosophy
(Atmospheric and Oceanic Sciences)

at the
UNIVERSITY OF WISCONSIN-MADISON
2019

Date of final oral examination: 11/18/2019

The dissertation is approved by the following members of the Final Oral Committee:
Tristan S. L'Ecuyer, Associate Professor, Atmospheric and Oceanic Sciences
Matthew, H Hitchman, Professor, Atmospheric and Oceanic Sciences
Jonathan E. Martin, Professor, Atmospheric and Oceanic Sciences
Daniel J. Vimont, Professor, Atmospheric and Oceanic Sciences
Norman B. Wood, Research Scientist, Space Science and Engineering Center

Abstract

Observing and Modeling Arctic Clouds: Exploring the Connections Between Cloud Phase, Precipitation, and Surface Radiation

by Elin A. McILHATTAN

Clouds are the primary modulator of radiation and moisture received by the Arctic surface. Long term, large scale, and detailed observations of Arctic clouds are required to connect particular cloud macro- and microphysical characteristics to their influence on the varied surfaces of the Arctic. Constraining that influence is key to accurate projections of future climate, particularly sea level rise. Prior to the launch of CloudSat and CALIPSO in 2006, Arctic cloud observations were limited in either time (field campaigns), space (individual research stations), or sensitivity (passive satellites). CloudSat's Cloud Profiling Radar (CPR) and CALIPSO's Cloud-Aerosol Lidar with Orthogonal Polarization (CALIOP) have provided detailed information on the location, phase, and vertical structure of Arctic clouds. This study leverages data from these two instruments to explore the connections between Arctic cloud phase, precipitation, and surface radiation.

First, the connection between cloud phase and precipitation is documented over the Greenland Ice Sheet (GIS). Partitioning snowfall observed over the GIS into two regimes — snowfall produced by ice-phase clouds and snowfall produced by Arctic mixed-phase clouds — reveals that the two regimes are distinct beyond the cloud phase that defines them, including differing seasonal and regional frequency, snowfall rates, geometric cloud depth, and air mass origins. Next, Arctic cloud representation is compared between two

versions of the Community Earth System Model (CESM), with CloudSat and CALIPSO observations used to provide physically reasonable benchmarks. The updated version of CESM has a markedly different mean state than the previous version, having addressed a known bias in Arctic mixed-phase clouds. Finally, the connection to surface radiation is examined using the Cloud Impact on Surface Radiation Ratio (CISRR). CISRR shows that over the icy surfaces of the Arctic, on average the warming effect of a cloud is at minimum twice as strong as its cooling effect.

*This work is dedicated to my grandmother, Mary Alice Parr,
who sparked my love for science and nature during our many
forest walks.*

Acknowledgements

Thanks first to my advisor, Tristan, for many years of encouragement, advice, fieldwork opportunities, and kindness. I chose to come to the University of Wisconsin because I thought he would be an amazing advisor and I was right.

My research group has been wonderful both personally and professionally. Thanks to everyone in the L'Ecuyer group for your help with classes, research, and navigating the marathon that is graduate school. I know I will have many long lasting friends and colleagues. In particular, Anne, Julia, and Marian in the Polar Coffee group and my many officemates in 1339 have been great sources of support over the years.

Thank you to my committee for helping to shape my research. Their input and guidance along the way has made me a better scientist. Thanks also to Jen Kay and Mark Kulie, who weren't officially on my committee, but provided invaluable mentorship and advice all the same.

Thank you to all of the AOS staff for their efforts in keeping the department organized, functioning, and fun. Pete in particular has rescued me from certain computer disaster on more than one occasion.

A huge thank you to Walter, Ethan, and Aronne for teaching me to program. Without their patient help, I could not have completed the research presented in this dissertation.

My fieldwork experiences were highlights of my graduate experience. Thanks to Carol, Dave, and Lee for making my time in Antarctica such a joyful one. Thanks to Andrew and the whole ORACLES team for adventures in Namibia and out over the South Atlantic.

Science Breakfast with Claire, Erin, Elena, and Alex kept me smiling and laughing through the process. As did my walks with Caitlin, yoga with Jamie, knitting with Hobbes, book discussions with Ritodhi, bike rides with Jude, Kerri, Kate, Branden,

Zach, and Dan, my visits and letters from Anna, Bridge School with Tucker, farm visits with Tyson, and board games with Andy, Hillary, Sam, and Wil.

Thank you to my family for their unwavering love and support. It took a village to get me to the finish line, and I am very lucky to have such a cheerful, joyous, and helpful village in mom, dad, Owen, Ali, Bea, and my little Reilly.

I received funding from NASA as an Earth and Space Science Fellow, which allowed flexibility to pursue research questions that interested me.

I enjoyed my time living in the midwest, exploring Wisconsin's many lakes, forests, and corn mazes, catching fireflies and skating on frozen ponds, marveling at ice caves and making new friends. Thank you, Wisconsin.

Contents

Abstract	i
Dedication	iii
Acknowledgements	iv
Contents	vi
List of Figures	viii
List of Tables	xiv
Abbreviations	xv
1 Introduction*	1
1.1 Background and Motivation	1
1.1.1 Clouds and their role in the Arctic system	1
1.1.2 Clouds Phase	2
1.1.3 Modeling Arctic Clouds	3
1.1.4 The Transformative Role of Active Space-borne Observations	4
1.2 To be Investigated	5
1.3 Copyrights	6
2 Satellite Observations of Snowfall Regimes over the Greenland Ice Sheet*	10
2.1 Introduction	10
2.2 Datasets and Methods	16
2.2.1 Satellite Data	16
2.2.2 Z_{path}	20
2.2.3 Ground-based Data	21
2.2.4 Reanalyses	23
2.3 Quantifying Snowfall Detectability from Space	23
2.4 IC and CLW Regime Characteristics	27
2.4.1 Snowfall Frequency and Accumulation	27

2.4.2	Cloud Characteristics	32
2.4.3	Associated Atmospheric Circulations	37
2.5	Conclusions	42
2.6	Author Contributions	45
3	Arctic Clouds and Precipitation in the Community Earth System Model Version 2*	60
3.1	Introduction	60
3.2	Methods	65
3.2.1	CESM	65
3.2.1.1	CESM1	65
3.2.1.2	CESM2	66
3.2.2	Satellite Observations	66
3.2.3	Comparing Model Output and Observational Data	67
3.3	Results and Discussion	69
3.3.1	Cloud Representation	69
3.3.2	Surface Radiative Fluxes and Temperature	71
3.3.2.1	Downwelling Radiation at the Surface	72
3.3.2.2	Surface Temperature	74
3.3.3	Precipitation	75
3.3.3.1	Snowpack on Sea and Land Ice	77
3.3.3.2	Snowfall	78
3.3.3.3	Rainfall	79
3.3.4	Cloud Liquid Tendencies	80
3.4	Conclusions	81
4	Global Observations of Cloud Impact on Surface Radiation Ratio (CISRR)	94
4.1	Introduction	94
4.2	Methods and Datasets	99
4.3	Datasets	99
4.3.1	Satellite Observations	99
4.3.2	Model Data	100
4.3.3	Ground-based Observations	100
4.4	Results	101
4.4.1	Observed Global CISRR	101
4.4.2	GCM Comparison	103
4.4.3	A Closer Look at the Greenland Ice Sheet	104
4.4.4	A Closer Look at the Stratocumulus off the Coast of Africa	106
4.5	Conclusions	108
5	Synthesis	116
5.1	Summary of Results	116

List of Figures

- 1.1 Simple cartoon depicting cloud impacts on radiation over ice surfaces; SW is depicted in yellow arrows, LW in orange. In a cloudless sky (**left**), incoming solar SW radiation reaches the surface unobstructed, with some reflected back to space depending on the surface albedo. Outgoing terrestrial radiation emits towards space, with only a small amount of downwelling LW radiation being emitted towards the surface by the low emissivity atmosphere. When an ice cloud is introduced (**center**), incoming SW is reflected by the cloud, reducing the amount reaching the surface. The increased emissivity of the cloud relative to clear sky also acts to increase the amount of downwelling LW reaching the surface. Relative to the all ice cloud, a liquid-containing cloud is ‘brighter’, reflects additional SW, and traps additional LW (**right**). Reproduced from McIlhattan (2016) 8
- 1.2 Top left: The Arctic region of analysis for Chapter 3 and 4 observations is outlined by the parallels at $\sim 66.91^\circ\text{N}$ and $\sim 81.99^\circ\text{N}$ (thick black lines). Sixteen days of overpasses are plotted as a gradient, ranging from black (the first overpass of day one) to white (the last overpass of day 16). Summit Station, Greenland is marked with a red star, with the region of overpass comparisons used in Chapter 4 outlined in blue. Bottom left: The path of the data plotted in the bottom figure. Right: Sample A-Train overpass from July 23, 2009. The plotted curtain passes over Greenland, which is shown in grey in Panels a-d. **Panel (a)** shows the reflectivity measured by CloudSat’s CPR, with values less than -20 dBz masked. Note that the high reflectivity values near the surface are due to ground clutter, and are not representative of atmospheric properties. **Panel (b)** contains snowfall rates from the 2C-SNOW-PROFILE data product. **Panel (c)** shows the downwelling LW radiative flux from the 2B-FLXHR-LIDAR data product. **Panel (d)** shows the locations and phases of the clouds within the curtain, as identified by the 2B-CLDCLASS-LIDAR data product. **Panel (e)** contains the total attenuated backscatter for the CALIOP 532 nm wavelength. Figure and caption reproduced from McIlhattan et al. (2017) 9

- 2.1 A summary of the CloudSat/CALIPSO satellite observations collected over the Greenland Ice Sheet (GIS). The GIS is divided into drainage basins as defined and numbered by the Ice Altimetry group at Goddard Space Flight Center. The color scale represents the total number of satellite overpasses in each basin during the full study period, January 2007 through August 2016. During that period, there were 14,703,887 individual satellite observations, 2,438,817 of which contained snowfall. 47
- 2.2 Snowfall frequency over the GIS defined as observations of snowfall divided by total observations in each gridbox. **(a)** is annual mean snowfall frequency using all observations from the study period, **(b)** is the percentage of total snowfall observations that were coincident with ice phase clouds, and **(c)** is the percentage of the total snowfall observations that were coincident with clouds containing liquid water. **(b)** and **(c)** sum to 100. **(d)** is winter mean snowfall frequency (Oct-Apr), with **(e)** and **(f)** the percentages of winter snowfall coincident with ice phase clouds and clouds containing liquid water, respectively. **(g)** is summer mean snowfall frequency (May-Sep), with **(e)** and **(f)** the percentages of summer snowfall coincident with ice phase clouds and clouds containing liquid water, respectively. The location of Summit Station is marked in each panel by a white star. 48
- 2.3 Snowfall mass contribution to the GIS. **(a)** is the annual average mass contribution broken down by basin, with the color scale representing Gt yr^{-1} for each basin and the total mass listed in the bottom left corner. **(b)** is the percentage of the snowfall mass produced by ice clouds, and **(c)** is the percentage of the mass produced by liquid containing clouds. The center (**(d)**, **(e)**, and **(f)**) and bottom (**(g)**, **(h)**, and **(i)**) rows are as the top row but for winter (Oct-Apr) and summer (May-Sep) months, respectively. The location of Summit Station is marked in each panel by a white star and the color of the circle surrounding it indicates the mass/percentage value for the area within 100km radius of the station. 49
- 2.4 Snowfall rates for all observed snowfall. **(a)-top** is a histogram of the observed rates of all GIS snowfall from 2CSP (log scale), and **(a)-bottom** is the regime percent for each histogram bin. **(b)** and **(c)** are the same for GIS winter (Oct-Apr) and summer (May-Sep) months, respectively. . . . 50

2.5 Annual cycle of regime fraction near Summit Station, Greenland. The regime fraction is the number of observations of one of the snowfall regimes (IC or CLW) divided by the total number of snowfall observations. A-Train values (solid lines, ‘x’ markers) shown for the near Summit annual cycle line plot are averages for all CPR footprints within 100km of Summit Station, Greenland. The solid lines represent the average of all observational years, each x depicting a single year’s monthly average. The shaded region surrounding each line is the standard deviation about the mean for the month. The red color is for the IC regime percent and the blue is for the CLW regime percent. For the A-Train data, the red and blue add to 1.0. The ICECAPS values (dashed lines, circle markers) are from vertically pointing instruments at Summit Station, also with markers representing a single year’s monthly average and the line being the mean of all years. The ICECAPS IC and CLW data do not add to 1.0 because of an additional category of ‘indeterminate’ (not plotted). 51

2.6 Annual cycle of GIS snowfall cloud characteristics. **(a)** the geometric cloud depth, and **(b)** the vertically integrated reflectivity for IC (red) and CLW (blue) snowfall observations. The solid lines represent the average of all observational years, each marker (x,+) depicting a single year’s monthly average. The shaded region surrounding each line is the standard deviation about the mean for the month. 52

2.7 As in Fig 2.6 except only including observations within a 100 km radius of Summit Station. 53

2.8 Histograms of precipitation regime geometric cloud depth. Red bins contain all footprints of IC snowfall and blue bins contain all footprints of CLW snowfall for each given season (Annual, Winter, and Summer) and region (Full GIS, Summit 100) as described in Fig 2.4. The histograms are normalized to highlight the distribution differences. The relative percentage of each regime is listed in the top right of each panel. 54

2.9 As in Fig 2.8 with $dB(Z_{path})$ 54

2.10 Composite two-dimensional histograms of CPR heights and reflectivities for the two snowfall regimes over the full GIS. The top row contains the entire annual cycle of events, including every footprint of snowfall detected during the study period, for IC **(a)** and CLW **(b)** events. The center row contains all wintertime (Oct-Apr) IC **(c)** and CLW **(d)** events, and the bottom row contains all summertime (May-Sep) IC **(e)** and CLW **(f)** events. There is a discontinuity apparent in each panel at ~ -15 dBZe. This is due to the 2CSP threshold of -15 dBZe for defining snowfall events. The shape and character of these plots compare well to Pettersen et al. (2018) Fig. 6. 55

2.11	ERA5 derived mean and anomaly 500 mb geopotential heights (GPH) and winds for the strongest 50 % of precipitation events that occurred within a 100 km radius of Summit Station during the study period. (a) shows the average 500 mb GPH and winds for 159 IC events and (b) shows the same for 43 CLW events. (c) and (d) show the GPH and wind anomalies for the IC and CLW cases, respectively. These panels are all consistent with Pettersen et al. (2018) Fig. 11, which also shows a strong trough ridge for the IC snow cases and relatively calm, quiescent conditions for the CLW snow cases.	56
2.12	As in Fig. 2.11 for the northern GIS: basins 1.1, 1.2, 1.3, and 1.4.	57
2.13	As in Fig. 2.11 for the western GIS: basins 6.1, 6.2, 7.1, 7.2, 8.1, and 8.2.	58
2.14	As in Fig. 2.11 for the southeastern GIS: basins 3.3, 4.1, 4.2, 4.3, and 5.0.	59
3.1	Annual cycle of liquid containing cloud (LCC) in the Arctic. The solid lines for CESM1 (red) and CESM2 (purple) illustrate the mean values for the monthly area weighted averages for all grid boxes between 70°N and 90°N from the 10 year branch simulations of their respective 1850s control runs. The dashed lines are also for CESM1 and CESM2, but for for the area between 66 and 82° N, for comparison with observations. The blue line represent the average of 2007-10 CloudSat/CALIPSO observations. The markers surrounding the lines each depict a single year's monthly average. The shaded regions denote the standard deviation about the mean for the month, showing the inter-annual variability.	84
3.2	As in Fig 3.1 for the annual cycles of (a) total cloud water, (b) liquid cloud water, and (c) ice cloud water. Note the same y-axis is used in (a) and (b) , but (c) is reduced.	85
3.3	As in Fig 3.1 for the annual cycles of (a) downwelling LW at the surface, (b) downwelling SW at the surface, and (c) total downwelling radiation at the surface (LW+SW). Note each y-axis different.	86
3.4	Seasonal averages of surface temperature in the Arctic. Seasonal divisions were chosen to capture sea ice minimum (August, September, October, top row) and sea ice maximum (February, March, April, third row). The plots for CESM1 (left column) and CESM2 (center column) are means from the 10 year branch simulations of their respective 1850s control runs. The difference plots in the right column are CESM2 minus CESM1, with red (blue) values showing increases (decreases) in temperature in CESM2 with respect to CESM1. The area weighted averages for the study area (70° N and 90° N) are shown in the lower right of each map.	87
3.5	As in Fig 3.1 for the annual cycles of (a) precipitation frequency in LCCs, (b) total precipitation frequency, and (c) total precipitation. Note each y-axis different.	88

3.6	Annual averages of water equivalent snow depth on sea ice (top row) and land (bottom row). The plots for CESM1 (left column) and CESM2 (center column) are means from the 10 year branch simulations of their respective 1850s control runs. The difference plots in the right column are CESM2 minus CESM1, with red (blue) values showing increases (decreases) in snow depth in CESM2 with respect to CESM1. The area weighted averages for the study area (70° N and 90° N) are shown in the lower right of each map.	89
3.7	As in Fig 3.1 for the annual cycles of a.) snowfall, and b.) rainfall. Note the y-axes are the same.	90
3.8	As in Fig. 3.6 for snow rate (top row) and rain rate (bottom row).	91
3.9	Vertical profiles of average microphysical tendencies for cloud liquid in the Arctic region (70°N-90°N) for CESM1 (solid lines) and CESM2 (dashed lines) from the 10 year branch simulations of their respective 1850s control runs. The values are averages of the 10 years of monthly averaged output.	92
4.1	General Cloud Radiative Impacts	110
4.2	(a) Annual average of the observed Cloud Impact on Surface Radiation Ratio (CISRR). CISRR is the ratio of shortwave cloud radiative effect (SWCRE) to the longwave cloud radiative effect (LWCRE). Observations are from the A-Train data product 2B-FLXHR-Lidar between January 2007 and December 2010. Regions in blue indicate the SWCRE is dominant and the clouds have an average cooling effect on the surface. Regions in red indicate the LWCRE is dominant and the clouds have an average warming effect on the surface. Regions in white indicate the SWCRE and LWCRE are balanced. Regions outside of the A-Train orbit are filled in gray. (b) Annual average CISRR for CESM-LE for the same time period. (c) The fractional difference between the top and middle figures. Regions in red indicate CESM-LE has too strong of cloud warming relative to observations, regions in blue show too strong cooling. Note: panel (a) is adapted from McIlhattan et al. (2017) Figure 2.	111
4.3	Annual cycle of CISRR for the near-global satellite observational range, 82° S-82° N. Satellite observations are in blue, CESM-LE outputs are in red. The heavy blue line represents the average of all observational years, each blue circle depicting a single year's monthly average. The heavy red line represents the average of all ensemble members, each red x depicting a single member's four year monthly average. The shaded regions are the standard deviation about the mean for each dataset	112

4.4	(a) Map of Greenland with a box showing the region used for the area weighted line plot, a line depicting the A-Train swath path, and a star at Summit Station. (b) A-Train overpass of SE Greenland depicting vertical curtains of reflectivity, CISRR, and cloud phase. (c) Annual cycle of CISRR over Summit Station, Greenland. Satellite observations are in blue, CESM-LE outputs are in red, surface observations are in black/grey. The region used for satellite/model analysis is grid boxes within 70-75° N and 35-41° W.	113
4.5	As in Fig 4.4(c) for surface net cloud radiative effect (NETCRE).	114
4.6	As in Fig 4.4 with CALIPSO lidar backscatter instead of radar reflectance in (a). The region used for satellite/model analysis in (c) is 34-20° S, 5-10° E.	115

List of Tables

2.1	Summary of CloudSat snowfall detection capability over Summit Station, Greenland based on averaged MMCR data for POSS detected snowfall. To mimic CloudSat detection we used: a height range of 960-1200 m, equivalent to the standard height of bin 5 of the CPR used in the 2CSP algorithm over land; and time average of 300 s, which at a moderate wind speed of 5 m s^{-1} is equivalent to the horizontal CPR footprint of $\sim 1.5 \text{ km}$.	46
2.2	Summary of 2CSP accumulation estimates by GIS basin.	46
3.1	Summary of high-frequency and tendency term CESM variables used in this analysis.	84
3.2	Summary of annual mean values of Arctic cloud properties. The \pm value is the standard deviation of the monthly mean values. The top section contains area weighted means for the full modeled Arctic ($70\text{-}90^\circ \text{ N}$) while the bottom section contains the area weighted means for the observed Arctic ($66.5\text{-}82^\circ \text{ N}$)	90
3.3	Summary of annual mean values for downwelling surface radiation in the Arctic. The \pm value is the standard deviation of the monthly mean values. The top section contains area weighted means for the full modeled Arctic ($70\text{-}90^\circ \text{ N}$), the center section are global means, and the bottom section contains the area weighted means for the observed Arctic ($66.5\text{-}82^\circ \text{ N}$)	93
3.4	Summary of annual mean values for Arctic precipitation. The \pm value is the standard deviation of the monthly mean values. The top section contains area weighted means for the full modeled Arctic ($70\text{-}90^\circ \text{ N}$) and the bottom section contains the area weighted means for the observed Arctic ($66.5\text{-}82^\circ \text{ N}$)	93
4.1	Summary of the time periods for the datasets used in Chapter 2. Details on the datasets and time periods can be found in McIlhattan et al. (2017).	110

Abbreviations

CALIOP	Cloud–Aerosol Lidar with Orthogonal Polarization (aboard CALIPSO)
CALIPSO	Cloud-Aerosol Lidar and Infrared Pathfinder Satellite Observation
CAM	Community Atmospheric Model
CESM	Community Earth System Model
CPR	Cloud Profiling Radar (aboard CloudSat)
CRE	Cloud Radiative Effect
ECMWF	European Centre for Medium-Range Weather Forecasts
GCM	Global Climate Model
GPH	Geopotential Height
GIS	Greenland Ice Sheet
ICECAPS	Integrated Characterization of Energy, Clouds Atmospheric State and Precipitation at Summit
IPCC	Intergovernmental Panel on Climate Change
LCC	Liquid Containing Clouds
LWE	Liquid Water Equivalent
IPCC-AR5	IPCC fifth Assessment on Report
LW	Longwave (radiation)
SW	Shortwave (radiation)

Chapter 1

Introduction*

1.1 Background and Motivation

1.1.1 Clouds and their role in the Arctic system

Clouds exert a strong control on the radiative energy received by the Earth's surface through two main pathways: reflecting incoming solar shortwave (SW) and trapping terrestrial longwave (LW) radiation (Fig 1.1). In addition to their radiative influence, Arctic clouds also play important roles in both the the freshwater cycle and the mass balance of ice sheets through precipitation. Individual cloud characteristics as well as underlying surface conditions vary greatly in time and space, modulating specific radiative and precipitation impacts. While clouds have been observed and studied for centuries,

Portions of this chapter are taken directly from McIlhattan et al. (2017), which was the publication that resulted from my M.S. thesis and provided the motivation for my dissertation research.

the Intergovernmental Panel on Climate Change (IPCC) Fifth Assessment Report (AR5) identified cloud feedbacks as one of the large puzzles remaining in accurately modeling future climate scenarios (Vaughan et al., 2013). Arctic clouds in particular have been the focus of numerous recent studies, in part due to improvements in technology that have allowed for more comprehensive in situ and remote sensing observational campaigns in the harsh region (e.g. Castellani et al., 2015, Cesana et al., 2012, Miller et al., 2015, Morrison et al., 2018, Norin et al., 2015). Quantifying the impacts of Arctic clouds is made even more difficult given the rapid rate of warming occurring at high latitudes in recent years owing to Arctic amplification (Serreze and Barry, 2011). The large, ice-covered regions and their potential contribution to sea level rise makes understanding and modeling Arctic responses to future climate scenarios a high priority (e.g. Clark et al., 2016, Hanna et al., 2013). There is, however, ongoing debate over the large-scale role of Arctic clouds since compelling evidence shows that increased cloud cover can both accelerate (Bennartz et al., 2013, Francis et al., 2005) and slow down (Kay et al., 2008) cryosphere melting depending, primarily, on the characteristics of the underlying surface. However, the short observational record and specific conditions of many ground-based investigations make extrapolation to a general Arctic cloud impact difficult.

1.1.2 Clouds Phase

The radiative properties of a cloud are strongly linked to cloud phase: liquid droplets, ice crystals, or a mixture of the two (Fig. 1.1). Despite the cold temperatures of the high latitudes, liquid containing clouds (LCCs) are ubiquitous throughout the Arctic

(Morrison et al., 2012). At sub-freezing temperatures, the cloud-liquid is supercooled, existing in unstable equilibrium with ice down to the homogeneous freezing point of -40°C (Wang, 2013). LCCs have been observed in the Arctic for decades by flight and ship campaigns, ground-based observatories (Shupe, 2011), and more recently by the space-borne lidar carried on the Cloud-Aerosol Lidar and Infrared Pathfinder Satellite Observation (CALIPSO) satellite (Cesana et al., 2012). The presence of such clouds has been shown to have a large influence on downwelling longwave radiation received at the surface, and thus also on melt over the Greenland ice sheet (GIS) in general (Van Tricht et al., 2016), and specifically during extreme melt events (Bennartz et al., 2013). Cloud phase has also been linked to distinct precipitation characteristics at Summit Station, a research observatory on the GIS (Pettersen et al., 2018). While the occurrence of LCCs and some of their impacts on downwelling LW and snowfall have been documented, the physical mechanisms and microphysical properties that maintain them are not yet well understood (Morrison et al., 2012).

1.1.3 Modeling Arctic Clouds

Since the processes that maintain supercooled LCCs in the Arctic are not well understood, modeling them correctly is difficult. Numerous studies have documented both local (Lenaerts et al., 2019b, Liu et al., 2011) and regional (Cesana et al., 2012, 2015, English et al., 2014, Forbes and Ahlgrimm, 2014, Kay et al., 2016a, 2012, Tan and Storelvmo, 2016) deficiencies in the ability of global climate models (GCMs) to accurately represent

cloud liquid in the Arctic. The misrepresentation of GCM LCCs has resulted in a variety of systematic temperature and radiation biases (e.g. Barton et al., 2014, Cesana et al., 2015, Forbes and Ahlgrimm, 2014, Pithan et al., 2014). For example, Kay et al. (2016a) found that insufficient cloud liquid in the atmospheric component of the Community Earth System Model (CESM) contributed to a cold bias of 2-3 °C at Summit Station. CESM has also been shown to overestimate snow frequency over the GIS in general (Lenaerts et al., 2019a) and specifically from LCCs over the full Arctic (McIlhattan et al., 2017)

1.1.4 The Transformative Role of Active Space-borne Observations

Evaluating Arctic cloud representation in models requires robust observations. Despite the clear need for large-scale, long-term Arctic cloud datasets, they have only recently become available. Ground-based observing stations provide long-term, high-quality cloud measurements; however, they require power and personnel, so only a few are located in the high latitudes (e.g. Summit Station, Greenland; Eureka, Nunavut, Canada; Utqiagvik, AK, USA) and they provide only highly localized cloud data. Passive satellites have full spatial coverage at the poles, but require contrast between the surface and the cloud layer in order to readily characterize clouds. They therefore struggle in the frequent case of cold, bright clouds overlying cold, bright surfaces near the poles. The lack of incoming SW during polar night also precludes use of visible channels in the region for much of the year.

The addition of active, space-borne sensors to the NASA A-Train satellite constellation (L'Ecuyer and Jiang, 2010) has transformed our ability to observe Arctic clouds and precipitation. Joining the A-Train in 2006, the CloudSat and CALIPSO satellites were designed specifically to improve our understanding of clouds and climate by documenting cloud vertical structure. Both carry active sensors, CloudSat with a 94-GHz Cloud Profiling Radar (CPR) (Tanelli et al., 2008) and CALIPSO with a Cloud–Aerosol Lidar with Orthogonal Polarization (CALIOP) (Winker et al., 2007). Neither requires inherent contrast to operate, and together they probe cloud particles ranging from tiny cirrus ice crystals to falling rain droplets. Most of the previously mentioned studies (e.g. Cesana et al., 2012, Kay et al., 2016a, 2012, Lenaerts et al., 2019a, McIlhattan et al., 2017) have relied on the CloudSat and CALIPSO instruments for observed cloud and precipitation characteristics. Figure 1.2 shows the 16 day overpass cycle of the A-Train satellites along with a sample overpass of the GIS of the CPR (a), CALIOP (e), and three example dataproducts (b-d).

1.2 To be Investigated

The studies that comprise Chapters 2-4 of this dissertation aim to further leverage observations from CloudSat and CALIPSO to increase our understanding of the connections between Arctic clouds, precipitation, and surface radiation. Each chapter presents a stand alone study, complete with introduction, methods, and conclusions specific to its results.

- In **Chapter 2** we use the satellite observations to partition snowfall over the GIS

into two regimes: snowfall produced by ice-phase clouds and snowfall produced by LCCs. We demonstrate that the two regimes are distinct beyond the cloud phase that defines them, including differing seasonal and regional frequency, snowfall rates, geometric cloud depth, and air mass origins.

- In **Chapter 3** we evaluate changes in the representation of Arctic clouds and precipitation in the newly released CESM version 2. We show that the Arctic mean state has changed markedly relative to CESM version 1; CESM2 has more than doubled the Arctic LCC frequency, has an Arctic surface temperature that is 3 K higher, and has more rain and less snow.
- In **Chapter 4** we use the Cloud Impact on Surface Radiation Ratio (CISRR) to show where on the Earth clouds act to warm the surface. The icy surfaces of the Arctic see a year round mean warming effect from clouds. We also look outside the Arctic to identify other regions where clouds predominantly warm the surface.

1.3 Copyrights

Portions of this dissertation are taken from manuscripts that have been previously published (Chapter 1) or are currently under review (Chapter 2). Chapters 3 and 4 are being prepared for publication.

Since portions of Chapter 1 were published in an American Meteorological Society journal (McIlhattan et al., 2017), the following copyright statement is required:

Copyright 2017 American Meteorological Society (AMS). Permission to use figures, tables, and brief excerpts from this work in scientific and educational works is hereby granted provided that the source is acknowledged. Any use of material in this work that is determined to be “fair use” under Section 107 of the U.S. Copyright Act or that satisfies the conditions specified in Section 108 of the U.S. Copyright Act (17 USC §108) does not require the AMS’s permission. Republication, systematic reproduction, posting in electronic form, such as on a website or in a searchable database, or other uses of this material, except as exempted by the above statement, requires written permission or a license from the AMS. All AMS journals and monograph publications are registered with the Copyright Clearance Center (<http://www.copyright.com>). Questions about permission to use materials for which AMS holds the copyright can also be directed to permissions@ametsoc.org. Additional details are provided in the AMS Copyright Policy statement, available on the AMS website (<http://www.ametsoc.org/CopyrightInformation>).

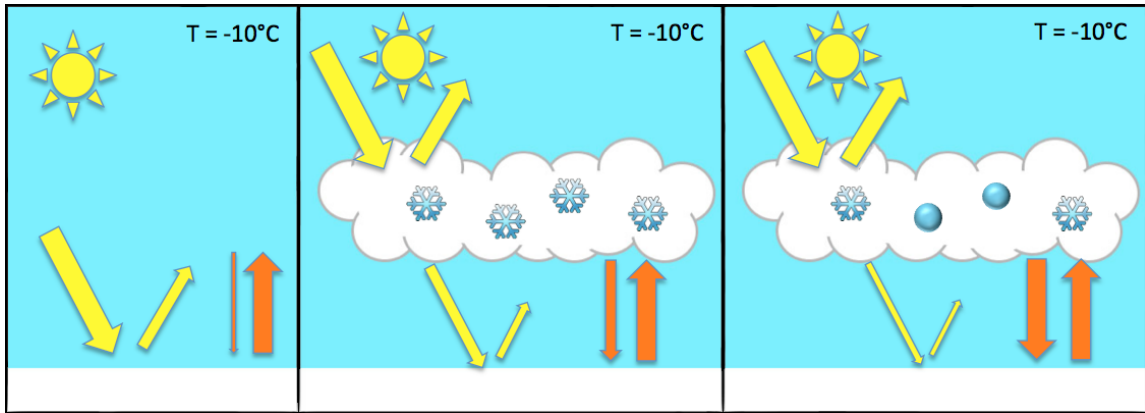


FIGURE 1.1: Simple cartoon depicting cloud impacts on radiation over ice surfaces; SW is depicted in yellow arrows, LW in orange. In a cloudless sky (**left**), incoming solar SW radiation reaches the surface unobstructed, with some reflected back to space depending on the surface albedo. Outgoing terrestrial radiation emits towards space, with only a small amount of downwelling LW radiation being emitted towards the surface by the low emissivity atmosphere. When an ice cloud is introduced (**center**), incoming SW is reflected by the cloud, reducing the amount reaching the surface. The increased emissivity of the cloud relative to clear sky also acts to increase the amount of downwelling LW reaching the surface. Relative to the all ice cloud, a liquid-containing cloud is ‘brighter’, reflects additional SW, and traps additional LW (**right**). Reproduced from McIlhattan (2016)

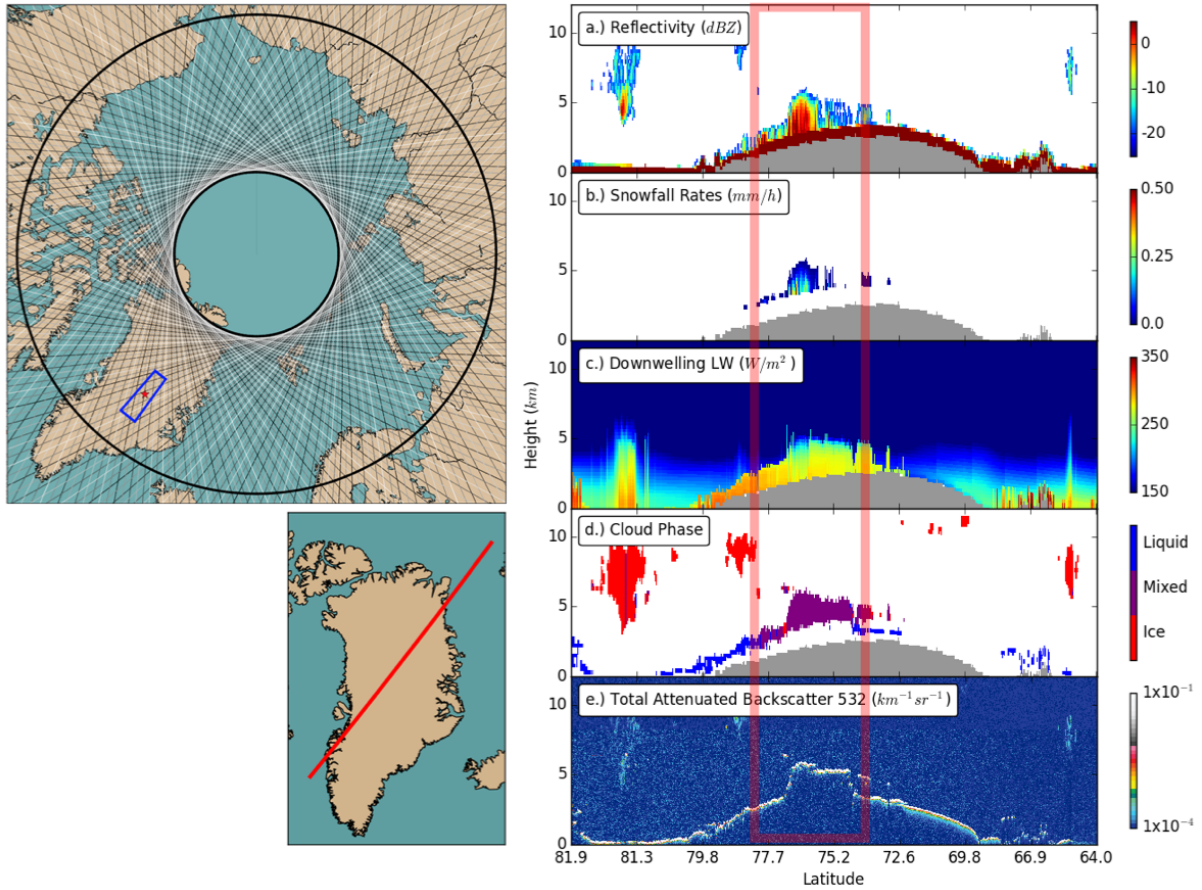


FIGURE 1.2: Top left: The Arctic region of analysis for Chapter 3 and 4 observations is outlined by the parallels at $\sim 66.91^\circ\text{N}$ and $\sim 81.99^\circ\text{N}$ (thick black lines). Sixteen days of overpasses are plotted as a gradient, ranging from black (the first overpass of day one) to white (the last overpass of day 16). Summit Station, Greenland is marked with a red star, with the region of overpass comparisons used in Chapter 4 outlined in blue. Bottom left: The path of the data plotted in the bottom figure. Right: Sample A-Train overpass from July 23, 2009. The plotted curtain passes over Greenland, which is shown in grey in Panels a-d. **Panel (a)** shows the reflectivity measured by CloudSat's CPR, with values less than -20 dBz masked. Note that the high reflectivity values near the surface are due to ground clutter, and are not representative of atmospheric properties. **Panel (b)** contains snowfall rates from the 2C-SNOW-PROFILE data product. **Panel (c)** shows the downwelling LW radiative flux from the 2B-FLXHR-LIDAR data product. **Panel (d)** shows the locations and phases of the clouds within the curtain, as identified by the 2B-CLDCLASS-LIDAR data product. **Panel (e)** contains the total attenuated backscatter for the CALIOP 532 nm wavelength. Figure and caption reproduced from McIlhattan et al. (2017)

Chapter 2

Satellite Observations of Snowfall Regimes over the Greenland Ice Sheet*

2.1 Introduction

The Greenland Ice Sheet (GIS) plays a key role in both the global energy budget (e.g. Box et al., 2012) and water cycle (e.g. Church et al., 2001, Enderlin et al., 2014). Unlike seasonally shifting sea-ice and snow cover, the GIS is a persistent bright surface, reflecting incoming solar energy back to space year-round. While there is variability in the percent of solar radiation reflected by snowy surfaces (35-90 %) due to melt-refreeze events and

* This chapter is under review in *The Cryosphere* with coauthors C. Pettersen, N. B. Wood, and T. S. L'Ecuyer

the age of the snow cover, it is consistently higher than other high-latitude surfaces such as open ocean (<10 %), forests (10-25 %), or grasslands (15-30 %) (Petty, 2006). There is enough freshwater stored in the GIS to raise sea levels globally by 7.2 m (Church et al., 2001). In recent decades the GIS has been losing mass beyond natural variability and has contributed 13.7 mm to global sea level rise since 1972 (Mouginot et al., 2019). In general, mass is gained from precipitation in the central GIS (above 2,000 m elevation) and lost from melting and ice dynamics in the margins (below 2,000 m elevation), and from the 1990s to the 2000s the rate of gain decreased while the rate of loss increased dramatically (Zwally et al., 2011). By the end of this century mass loss from the GIS is predicted to contribute up to 15 cm to the global mean sea level (Vaughan et al., 2013).

Snowfall is responsible for both building mass and brightening the surface of the GIS. Surface brightness, or albedo, is largely dependent on the frequency of precipitation because fresh snow is more reflective than old snow in the shortwave (SW) solar wavelengths (Box et al., 2012, Enderlin et al., 2014, Petty, 2006). However, the SW albedo only matters in summer when there is incoming solar radiation; therefore the seasonal timing of snowfall events must also be considered. Snowfall is the major source term for the mass of the GIS (Bring et al., 2016, Ettema et al., 2009), and in addition to frequency the snowfall rate and duration of events are important for accumulation.

Snowfall characteristics depend on atmospheric conditions, regional surface properties, and topography. There is consensus among modeling studies and observational datasets that most of the GIS snowfall is produced by cyclones, with the highest accumulation

occurring where their moist air masses move up the steep orography of the southeastern coastline (e.g. Berdahl et al., 2018, Hakuba et al., 2012, Kapsner et al., 1995, Schuenemann et al., 2009, Vihma et al., 2016). One encounters less agreement when it comes to the total amount of snowfall over the full GIS. Ground-based observations are concentrated near the coasts, and often indirectly measure snowfall using changes in surface height (Steffen and Box, 2001). Estimating snowfall frequency and accumulation over the whole ice sheet is often achieved using regional climate models (e.g. Berdahl et al., 2018, Mougnot et al., 2019) or reanalyses (e.g. Schuenemann et al., 2009). However, models and reanalyses require robust observations to serve as constraints, and since those are lacking, the community has produced a wide range of GIS snowfall estimates (van den Broeke et al., 2016, Vernon et al., 2013).

Given the scarcity of ground-based observations, satellites are needed to look at snowfall across the GIS. Surface snowfall can be estimated from space using brightness temperature depression in passive microwave measurements, however these estimates are subject to large errors when applied over non-ocean surfaces due to variations in surface emission (Liu and Curry, 1997), including emission variations of the ice and snow-covered surfaces of the GIS. Passive microwave sensors can also provide information on the extent, and in some conditions depth, of the snowpack (Frei et al., 2012), however, they measure snow already on the ground which can be impacted by processes other than snowfall (e.g. blowing snow, melt events, etc) and do not give information about the clouds that produce the snow. Satellite-borne active sensors are currently the best platform to measure the annual cycle of snowfall over the full GIS and give insight into the coincident clouds.

In recent years, the Cloud Profiling Radar (CPR) aboard NASA's CloudSat satellite has provided unprecedented insight into snowfall processes in remote, ice-covered regions (e.g. Milani et al., 2018, Norin et al., 2015, Palerme et al., 2019, 2016, 2014, Souverijns et al., 2018). Two recent studies have used CloudSat's CPR to look at snowfall over the GIS in particular: Lenaerts et al. (2019a) focused on GIS snowfall frequency and leveraged the satellite observations to evaluate climate model output; and Bennartz et al. (2019) used the radar measurements to provide the first in-depth, observationally based snowfall rate estimates of the GIS.

In order to understand how snowfall on the ice sheet may change in the future, it is not sufficient to merely know how much snow accumulates but also understand the processes and large-scale drivers that produce it. Using detailed, ground-based measurements at Summit Station, a research facility in the center of the GIS, Pettersen et al. (2018) (hereafter P18) showed that there are distinct atmospheric processes associated with snowfall events that originate from either ice clouds or from Arctic mixed-phase clouds. P18 used microwave radiometers (MWRs) to partition snowfall events into the two regimes: those produced by fully-glaciated ice clouds and those produced by Arctic mixed-phase clouds containing super-cooled liquid water (hereafter IC and CLW events, respectively). P18 highlighted that each precipitation regime exhibited marked differences in cloud microphysical properties, associated atmospheric circulations, and air mass origins.

P18 found that IC events at Summit are associated with deep clouds that advect moist air quickly up and over the southeast Greenland coastline and on to the central GIS. The

North Atlantic cyclones that set up these cloud systems have been credited in many studies for producing snowfall over Greenland (e.g. Berdahl et al., 2018, Schuenemann et al., 2009, Serreze and Barrett, 2008). Conversely, P18 found that CLW events are associated with shallow clouds and slow-moving, quiescent air masses originating from the south and southwest coastlines. The high surface pressure anomaly associated with these conditions was shown by Hanna et al. (2016) to have mainly positive precipitation anomalies over the GIS in reanalyses.

In this paper, we aim to expand the ground-based snowfall regime analysis of P18 to the full GIS, exploring the importance of cloud phase to both snowfall frequency and accumulation. Flying in the same NASA satellite constellation as CloudSat, the Cloud–Aerosol Lidar and Infrared Pathfinder Satellite Observations (CALIPSO) satellite carries the Cloud-Aerosol Lidar with Orthogonal Polarization (CALIOP) instrument which is highly sensitive to the cloud liquid layer at the top of Arctic mixed-phase clouds and can thus reliably discern cloud phase (Matus and L’Ecuyer, 2017, McIlhattan et al., 2017, Morrison et al., 2018). In this work, we use cloud phase data from CALIOP to divide snowfall events identified by CloudSat’s CPR into IC and CLW regimes. Leveraging the synergy of the two instruments, we:

- Quantify the percentage of IC and CLW events that are likely missed by CloudSat using ground-based instrumentation
- Map the seasonal frequency of snowfall over the GIS and show the relative contributions from IC and CLW events

- Quantify the total accumulation of snowfall and the fraction resulting from each regime
- Compare the satellite observations to ground-based data from Summit Station
- Examine the annual cycles of precipitation regimes and discuss their importance for building and brightening the GIS
- Document the average cloud properties of the two precipitation regimes and their full distributions
- Map the atmospheric circulations that favor each regime in different regions: near-Summit, southeastern, western, and northern GIS

In the following section we describe the datasets and methods used in this study (Section 2.2). In Section 2.3, we compare CloudSat's CPR to surface observations, showing that the CPR is capable of detecting $\sim 95\%$ of IC events and $\sim 75\%$ CLW events. We go on to examine the distinctions between IC and CLW events in Section 2.4. Looking first at snowfall frequency and accumulation (Section 2.4.1), we find that the IC snowfall events are overall more frequent and have higher snowfall rates than the CLW events. IC snowfall therefore plays the dominant role in building the GIS, producing $\sim 80\%$ of the total annual accumulation. However, we find the CLW events to be nearly as frequent as IC events in the summer months, meaning that CLW events play an important role in brightening the GIS during the time of greatest solar insolation. We go on to examine the differences in clouds characteristics for two regimes (Section 2.4.2). Clouds associated

with IC snowfall are consistently both geometrically deeper and have larger integrated reflectivity values than clouds associated with CLW snowfall. The final distinction we look at is in atmospheric circulation patterns coincident with regime snowfall in four regions of the GIS (Section 2.4.3) We find evidence that varied cyclone locations are associated with IC events in each region, while CLW events in all regions occur under anomalously high pressure scenarios. We summarize our conclusions in Section 2.5.

2.2 Datasets and Methods

To explore the connection between cloud phase and the rate and frequency of snowfall over the GIS, we used space-borne observations from NASA’s A-Train satellite constellation. We employ a product developed using instruments at Summit Station as well as ground-based radar measurements to independently corroborate the regime behavior observed by the satellites. We use reanalysis output to investigate what large-scale atmospheric patterns are coincident with the two precipitation regimes.

2.2.1 Satellite Data

NASA’s A-Train satellites orbit at a height of 705 km and a 98.2° inclination in a sun-synchronous orbit, providing detailed observations of the atmosphere and underlying terrain from 82° S to 82° N (L’Ecuyer and Jiang, 2010). The CloudSat and CALIPSO satellites joined the A-Train in 2006 and their close positioning has allowed for over 10 years of collocated observations of the vertical distribution of clouds and precipitation. The 94-GHz CPR aboard CloudSat has a minimum detectable reflectivity factor of -30

dBZe and is sensitive to large cloud particles and hydrometeors (Tanelli et al., 2008). CALIPSO carries CALIOP (532- and 1064-nm wavelengths) which is capable of determining cloud phase based on the differing backscatter of ice crystals and liquid droplets (Wang et al., 2012). CALIOP's short wavelengths attenuate quickly and only penetrate clouds with relatively low optical depths, ~ 3 or less (Chepfer et al., 2010), so CALIOP on its own is not capable of providing information on moderate to heavy snowfall or snowfall beneath liquid cloud layers. The CPR's longer wavelength, however, can generally penetrate all Arctic clouds to detect underlying precipitation (Battaglia and Delanoë, 2013). It is the combined skill of these instruments that allows for this study.

CloudSat experienced a battery failure in 2011, causing the CPR to only provide data for daytime overpasses. Due to the high latitude position of the GIS, this malfunction has a seasonal impact, rather than a daily one. In summer, the GIS experiences nearly constant solar illumination so there is no difference in the pre- and post-2011 summertime data collection. While there is a reduction in the post-2011 wintertime Arctic data, it is not eliminated completely. The CPR continues to function for some minutes as it passes into the darkness of boreal winter, resulting in the collection of approximately half of the wintertime Arctic observations collected prior to the battery malfunction (Skofronick-Jackson et al., 2019).

The satellite data used in this study is referred to in terms of overpasses and footprints. An overpass is an individual flyover of the GIS, and comes from a single granule of CloudSat data — one orbit around the Earth (roughly 1.5 hours). Each CloudSat footprint has a

horizontal resolution of approximately 1.4 x 1.7 km at the surface. Because of its shorter wavelength, ~ 12 CALIOP footprints fit within a single CPR footprint. The CALIOP cloud phase information has therefore been scaled to the CPR resolution in the below described data products. In this study we use all available footprints where both the CPR and CALIOP were functioning. For the regional maps, all A-Train data were binned to a $\sim 0.94^\circ$ latitude by 1.25° longitude grid (consistent with McIlhattan et al. 2017).

This study is primarily based on three data products produced by the CloudSat Data Processing Center: 2C-SNOW-PROFILE, 2B-CLDCLASS-LIDAR, and 2B-GEOPROF (hereafter 2CSP, 2BCCL, and 2BG, respectively). These products have all been extensively described elsewhere so the reader is directed to the citations provided below for algorithm and validation details. All granules available in the R05 CloudSat data product release as of May 2019 are used - no years or months were excluded. In total this research includes more than 17 thousand overpasses of the GIS, consisting of 14.7 million total individual footprints, 2.4 million of which contained snowfall (Fig. 2.1). In addition to gridding the observations, we have also collected satellite footprints made within each GIS drainage basin as defined by Zwally et al. (2012) and shown in Fig. 2.1. The basins each have consistent surface slope relative to atmospheric advection (Zwally et al., 2012), enabling us to look at snowfall characteristics in large regions that are more meaningfully homogeneous than grid boxes (Zwally et al., 2012).

The first step in our analysis is to obtain snowfall frequency and rate from 2CSP, a radar-only product that uses CPR reflectivity information from the lowest clutter free bin to

estimate surface snowfall rates (Wood and L'Ecuyer, 2018). The CPR cannot directly observe snowfall at the surface because of ground clutter — the bright surface return overwhelms the detector and creates a blind zone in the ~ 1 - 1.2 km closest to the surface. To make a surface rate estimation, 2CSP relies on the connection between precipitation-sized particles aloft and snowfall at the surface; the downward snow mass flux retrieved at the top of the blind zone is assumed to reach the surface (discussed in Section 2.3). Studies comparing 2CSP to surface data have validated this connection, specifically in the polar regions (Maahn et al., 2014, Milani et al., 2015, Norin et al., 2015, Palerme et al., 2016). The minimum detectable rate for 2CSP is ~ 0.0005 mm/h.

We define a footprint as snowing if it has a non-zero 2CSP snowfall rate in the lowest clutter free bin, unless that bin is flagged as possibly contaminated by ground clutter. Potential contamination is indicated by the third bit in the 2CSP status flag, which is set when there is a large difference between the snowfall rate in the lowest clutter free bin and the bin immediately above. This occurs naturally if there is a very shallow snowfall event such as lake effect snow, where the precipitation-sized particles are confined to ~ 1 - 1.5 km of the surface, or it means that lowest bin expected to be clutter free is actually contaminated by surface return. Contamination is most prevalent in regions of steep, icy topography where the digital elevation map used to determine the surface level does not exactly match conditions at the time of the overpass (Bennartz et al., 2019). Palerme et al. (2019) showed that the edges of the GIS are particularly prone to clutter in the R04 version of 2CSP, but the updated elevation map in R05 has reduced the number of contaminated pixels. In this study we use the snowfall rate in the bin above the

lowest for all profiles with potential clutter contamination, consistent with Palerme et al. (2019) and Milani et al. (2018). Bennartz et al. (2019) also highlighted the issue of surface contamination in GIS snowfall estimates using 2CSP, but approached a solution by creating a completely new rate based on reflectivities aloft.

In a given footprint, if 2CSP indicates snowfall at the surface, we then obtain cloud phase for that footprint from the 2BCCL. The sensitivities of both the CPR and CALIOP are leveraged by 2BCCL to determine phase (Wang et al., 2012): the lidar is particularly sensitive to cloud liquid layers while the CPR provides additional ice crystal information that the lidar may miss due to attenuation. 2BCCL gives each vertically contiguous cloud a single phase (ice, liquid, or mixed), regardless of how the particles within the cloud are distributed. If there are multiple cloud layers in a given column, we take the phase of the lowest cloud layer. Our liquid-containing classification (CLW) includes both ‘liquid’ and ‘mixed’ flags while our ice classification (IC) uses only ‘ice’.

Finally, we use a second radar-only product, 2BG (Marchand et al., 2008), to further characterize the clouds producing snowfall by looking at reflectivity properties. From 2BG we obtain the height and magnitude of radar reflectivity factor, Z_e , in the vertical column and also the vertically integrated reflectivity, Z_{path} , discussed below.

2.2.2 Z_{path}

Ice water path (IWP) is a useful measure to explore the contents of clouds, but converting radar reflectivities to IWP is sensitive to ice habit and particle size distribution, which

are quite variable over the GIS (P18; Korolev et al., 1999). In this work we use an alternate value, column-integrated reflectivity (Z_{path} , $\text{mm}^6 \text{ m}^{-2}$). Z_{path} is a relatively simple measurement related to the amount of hydrometeor backscatter that can reliably be used as a proxy for IWP (defined as Z_{int} in Kulie et al., 2010, Pettersen et al., 2016). It is defined as:

$$Z_{path} = \int_{H_{CB}}^{H_{CT}} Z_{CPR}(z) dz, \quad (2.1)$$

with H_{CT} and H_{CB} as the cloud-top height and base, respectively, and Z_{CPR} is the CloudSat CPR radar reflectivity factor at a given height, z . Cloud boundaries come from 2BCCL and the reflectivities between those boundaries come from 2BG. The 2BG reflectivity factors are converted from the provided $dBZe$ to Ze before integrating, then from Z_{path} to $dB(Z_{path})$ for plotting and discussion (consistent with Kulie et al. (2010)).

2.2.3 Ground-based Data

The ground-based observations of snowfall, cloud phase, and radar reflectivity used in this study were collected as part of the ongoing Integrated Characterization of Energy, Clouds, Atmospheric State and Precipitation at Summit (ICECAPS) project (Shupe et al., 2013). Summit Station is located at $72^{\circ}36'$ N, $38^{\circ}25'$ W and is denoted with a white star on all GIS maps in this work (e.g. Fig 2.1).

Surface detected snowfall events at Summit were defined and segregated into IC and CLW events using the novel method developed and detailed in P18. P18 employed differences in absorption and scattering properties of cloud liquid and ice in MWR measurements to separate the two precipitation regimes. The IC and CLW surface based snowfall data are for the period 2010-2015. The data product as well as technical details are available in the National Science Foundation (NSF) Arctic Data Center archive (Pettersen and Merrelli, 2018).

In Section 2.3, we use averaged reflectivity measurements from ICECAPS's millimeter wavelength cloud radar (MMCR) to estimate the detectability of surface snowfall events from space by the CPR. The MMCR is a vertically pointing, 35 GHz, Doppler pulsed radar (Moran et al., 1998) that is sensitive to both ice and liquid hydrometeors.

To convert the MMCR reflectivity native resolution to CloudSat-like footprints we use time averaging and thresholds that closely mimic the CPR and its algorithm: a height range of 960-1200 m AGL, equivalent to the standard height of bin 5 of the CPR used in the 2CSP algorithm over land; and a time average of 300 s, which at a moderate wind speed of 5 m/s is equivalent to the horizontal CPR footprint of ~ 1.5 km. Missing MMCR reflectivities are excluded from the average, while clear bins are included.

The 1-minute resolution snowfall regime data (Pettersen and Merrelli, 2018) is sampled to match the MMCR time averaging period. If snow occurred (defined in P18 as Precipitation Occurrence Sensor System (POSS) power unit > 2) for any time during the sample, the sample counts as a snow occurrence, even if for the majority of the averaged time

no snow was falling. For sample mean snowfall rates, the POSS rate was averaged over the sample with missing values omitted and values associated with POSS power unit <2 included as zeros.

2.2.4 Reanalyses

Similar to P18, in Section 2.4.3 we use reanalyses to examine the atmospheric circulations associated with IC and CLW events for various GIS regions. The European Centre for Medium-Range Weather Forecasts (ECMWF) provides the global reanalysis product ERA5 (C3S, 2017), from 1950 to present. ERA5 contains hourly data with a latitude and longitude spatial resolution of $0.25^\circ \times 0.25^\circ$.

For each region analyzed in Section 2.4.3, we use only the most intense 50 % of IC and 50 % of CLW events identified by CloudSat/CALIPSO. To rank the strength of observed events, we take a cumulative sum of surface snowfall rate for a single overpass within a basin. Thus, both large-scale, light snowfall and small-scale, heavy snowfall are included in the top 50 %. For the selected events, we use the nearest hourly ERA5 output to examine the mean and anomaly of the 500 mb geopotential height (GPH) and winds. For the anomalies, we subtracted the long-term monthly mean from the event day/hour.

2.3 Quantifying Snowfall Detectability from Space

The ICECAPS instrument suite at Summit provides a unique opportunity to look at IC and CLW cases from both below and above. Radar-derived snowfall rate estimates are

dependent on assumptions of ice habit, which is variable in space and time (Kulie et al., 2010), making it impossible to exactly measure surface snowfall from space. However, if the CPR detects precipitation size particles immediately above the blind zone, it is a good indicator that snow is falling at the surface (Bennartz et al., 2019, Milani et al., 2018, Palerme et al., 2019).

When comparing 200 m and 700 m above ground level (AGL) snowfall reflectivities at Summit, Castellani et al. (2015) found evidence of growth — the reflectivities at 200 m AGL were larger than 700 m AGL on average — suggesting that towards the surface there is an increase in particle masses, an increase in number concentration, or a shift from small particles to large particles in the size distribution (or a combination thereof). Since an increase in reflectivity can arise from one or more of these different processes, when we say “growth” throughout this work, we are not specifically implying particle mass increase, but the collection of snow property changes that can influence reflectivity. Castellani et al. (2015) showed the distribution of reflectivity differences between 200 and 700 m AGL have both positive and negative values, meaning that while on average snowflakes at the top of the blind zone likely underwent growth as they fell, it was not guaranteed. McIlhattan et al. (2017) looked specifically at the presence of clouds containing super-cooled liquid over Summit and the frequency with which they precipitated, finding that the 2CSP and 2BCCL (R04 versions for 2007-10 only) matched well with the surface observations from Miller et al. (2015). Figure 6 of P18 further supports the idea that snowfall cases should be detectable from space, since reflectivities greater than 0 dBZ occur frequently above the blind zone: up to 3 km AGL for IC snowfall cases and 2 km

AGL for CLW cases. However, the MMCR reflectivities shown in P18 cannot be directly compared to the CPR due to differing space and time averaging.

Previous papers have mentioned that due to the blind zone of the CPR, a number of snowfall events are likely missed (e.g. Bennartz et al., 2019, Maahn et al., 2014, Palerme et al., 2019). We aim here to quantify that number for our two snowfall regimes. By averaging the Summit MMCR data for IC and CLW cases, we create a CPR-like vertical profile and use coincident POSS measurements to define cases as snowing or not. Averaging and instrument details can be found in Section 2.2.3. For profiles with snow occurrence, the sample is considered missed by the CloudSat-like MMCR observations if the radar reflectivity in the selected CloudSat vertical bin is below the -15 dBZe threshold as defined in the 2CSP algorithm. Despite the differing wavelengths of the CPR and MMCR (frequencies of 94 and 35 GHz, respectively), at the snowfall defining threshold of -15 dBZe their reflectivities are comparable. For such small reflectivities, in most cases the ice particles are small such that the reflectivity is in the Rayleigh regime for both wavelengths.

The results of this comparison are summarized in Table 2.1. Note that when the MMCR was averaged over time, sometimes more than one type of Summit snowfall event (IC, CLW, or indeterminate) were blended together. For clarity, we are only showing results for the combined total, IC-only, and CLW-only scenes. In IC-only averaged scenes, all included snowfall events contained only fully-glaciated ice clouds. In CLW-only averaged

scenes, cloud liquid was present in each snow event, though to be clear the CLW clouds are almost always mixtures of both supercooled-liquid water and ice.

Out of 20,516 total snowfall events identified in the averaged P18 dataset, 22 % of the events would have been undetected by the CPR. When looking at the 9,777 CLW-only snowfall events, the missed fraction goes up to 25 % and for the 3,545 IC-only events the missed fraction goes down to 5 % (the remaining 7,194 cases are mixed or indeterminate). The mean snowfall rate reported by the P18 dataset for the missed events is consistently about half the rate of the detected cases, meaning that the CPR is missing the lighter of the events overall, and within both of the regimes. Broadly, these results indicate that the CPR is sensitive enough to detect nearly all of the IC-only cases (95 %) as they appear at Summit, but has more difficulty with the Summit CLW-only cases, capturing a smaller majority (75 %).

Bennartz et al. (2019) showed that 2CSP underestimates snowfall accumulation near Summit Station relative to stake field and MMCR estimates. P18 showed that CLW cases are responsible for slightly more than half of accumulation at Summit. Our results here indicate the CPR is likely missing ~ 25 % of CLW cases, which could mean that the low 2CSP accumulation bias is an issue of missing snowfall cases entirely, rather than an underestimate of rate as was suggested in Bennartz et al. (2019). The following results are not modified based on this under-detection, but the implications are touched on in the discussion and conclusions.

2.4 IC and CLW Regime Characteristics

2.4.1 Snowfall Frequency and Accumulation

The frequency of snowfall varies both regionally and seasonally over the GIS. There is a north-south gradient in the annual frequency map of all snow events (Fig 2.2, a), with frequency increasing towards the southern end of the GIS. The highest concentration of snowfall observations is along the southeastern coastline. This is consistent with previously documented heavy snowfall in the area, with studies attributing it to the region's steep orography and interaction with paths of North Atlantic storms (e.g. Berdahl et al., 2018, Hakuba et al., 2012, Schuenemann et al., 2009). When we partition the annual snowfall into IC and CLW cases (Fig 2.2, b and c, respectively) the GIS snowfall frequency is clearly dominated by IC events. There is an east-west gradient in the regime fraction, with more CLW cases along the western side of the GIS than the eastern.

In wintertime (defined here as October through May, consistent with P18), there is very little snowfall in the northern GIS and an even stronger north-south gradient compared to the annual distribution (Fig 2.2, d). The concentration of events along the southeastern coastline is also more prominent, with snowfall occurring up to 40 % of the time. This is consistent with the wintertime high concentration of cyclone centers and increased cyclone intensity off the southeastern GIS coastline, found by Zhang et al. (2004) using reanalyses. IC events (Fig 2.2, e) make up nearly 100 % of the wintertime snowfall

observations over most of the GIS, with the exception of western Greenland where CLW approaches 50 % of the cases in some grid boxes nearest the central coast (Fig 2.2, f).

In summertime (defined here as May through September, consistent with P18), the north-south gradient is gone, with a fairly consistent 20-30 % snowfall frequency over the GIS (Fig 2.2, g). The precipitation occurring at the edges and outside of the ice sheet is predominantly rainfall during this season, and since rain is excluded from this study the frequency over the coast and ocean is reduced. CLW cases make up ~ 50 % of the snowfall frequency over much of the ice sheet in summer months (Fig 2.2, i), which is consistent with what P18 observed at Summit Station. The southeastern coastline, however, remains more influenced by IC snowfall even in summer. The east-west gradient in regime fraction is distinct in summer, with more CLW along the western side of the ice sheet (reasons for this east-west regime divide are examined in Section 2.4.3). In the summer months, the GIS receives ~ 83 % of its annual incoming solar insolation. So while the IC events clearly occur more often annually, the CLW events are equally important for brightening the GIS and increasing the surface albedo during the months of intense downwelling shortwave radiation.

Snowfall accumulation is the only significant, positive term in the surface mass balance of the GIS (Jakobson and Vihma, 2010, Zwally et al., 2011). The estimate of mass added to the GIS by snowfall by season and regime is shown in Fig 2.3. The mean annual accumulation for the study period is 399 Gt yr^{-1} (Fig 2.3, a) which is distributed nearly equally between winter (198 Gt yr^{-1} , Fig 2.3, d) and summer (201 Gt yr^{-1} , Fig 2.3,

g). However, by our definition summer represents only five months compared to winter's seven, meaning that the intensity of summer snowfall is greater on average. Snowfall from IC events makes up $\sim 80\%$ of the total annual accumulation by mass, $\sim 88\%$ of the winter, and $\sim 71\%$ of the summer accumulation (Fig 2.3, b, e, and h, respectively). While there is some seasonal variation in the accumulation and distribution between regimes, it is clear that in all basins the majority of the snowfall mass comes from IC events. The accumulation by individual basin is summarized in Table 2.2.

Previous estimates for GIS mean annual accumulation have generally been higher than this study, with different models, configurations, and reanalyses ranging from $\sim 581 - 899$ Gt yr⁻¹ (Cullather et al., 2014) and the recent CloudSat observational study, Bennartz et al. (2019), reported 586 ± 129 Gt yr⁻¹. As discussed previously, models and reanalyses rely on observations for constraints, and over the GIS those have historically been sparse. The CPR derived snowfall rate in Bennartz et al. (2019) had a correction (relative to 2CSP) to increase high elevation rates to more closely match Summit observations with the assumption that there would be little effect outside of high elevations because snowfall was expected to be associated with higher reflectivities. While this is likely true for IC cases, the following analysis demonstrates that CLW clouds are consistently thinner geometrically and with low IWP over the full ice sheet. Our GIS accumulation estimate is likely biased low because the CPR is missing $\sim 25\%$ of CLW snowfall cases (as discussed in Section 2.3), but it is not clear that tuning all high elevation snowfall rates to one particular location will improve our larger scale evaluation and thus we present 2CSP rates as they are.

A histogram of the rates for all observed snowfall (Fig. 2.4, a, top) illustrates that the vast majority (note the log scale on the y-axis) of snowfall observations are very light. Just over 92 % of the snowfall observed is contained in the first bin, which includes snowfall rates of $\leq 0.41 \text{ mm hr}^{-1}$ liquid water equivalent (LWE). Snowfall is frequent in both seasons, with winter and summer time periods each accounting for roughly half (~ 1.2 million) of the snowfall-containing satellite footprints. The winter histogram (Fig. 2.4 b, top) looks much the same as the annual, though has slightly steeper drop-off from first to the second bin, indicating that winter snowfall is often lighter, fitting with the general scarcity of available atmospheric moisture during these months. The summer histogram (Fig. 2.4, c, top), on the other hand, shows a smaller decrease between the first and second bins, consistent with generally more summertime atmospheric moisture allowing for increased hydrometeor formation and/or growth. The slope of the distributions between the two seasons is distinct, with summer having an overall steeper decline and fewer observations over 6 mm hr^{-1} compared to winter. This means that while the common summer events are snowing at slightly higher rates on average, it is in winter that the less frequent, highest-intensity snowfall occurs. Jakobson and Vihma (2010) found a similar relationship using reanalysis data in the Arctic, showing winter having lower precipitation rates than summer overall, but the annual precipitation maximum occurring in winter along the southeastern GIS coastline. They attributed the regionally strong winter snowfall to the strength and position of the North Atlantic cyclone tracks.

The distribution of snowfall events between the two regimes is stark. In the annual (Fig. 2.4, a, bottom), IC observations (red) are more frequent at all snow rates. The

largest fraction of CLW events (blue, $\sim 32\%$) occurs at the lightest snowfall rates and the fraction decreases rapidly, with all events greater than 6 mm hr^{-1} produced by ice clouds, consistent with the findings of P18 at Summit. In winter (Fig. 2.4, b, bottom) the CLW fraction decreases to $\sim 18\%$ for the lightest events and IC are responsible for greater than 95% of the observations of snowfall $>2\text{ mm hr}^{-1}$. CLW and IC produce nearly the same number of light events in summer (Fig. 2.4 c, bottom), and CLW has a larger share of the moderate events than in winter. However, in both summer and winter, the heaviest snowfall is produced by IC events.

The motivation for this study was to see if the analysis in P18 at Summit Station could be expanded to the full GIS, and if so, to see how the regime characteristics compare. To compare with the point source ground measurements from P18, we selected only satellite observations made within 100 km of Summit Station (the starred circle in Fig 2.1). Fig 2.5 illustrates the annual cycle of regime cloud frequency: the fraction of IC events and the fraction of CLW events out of all the snowfall events observed. The CLW fraction for both the satellite (solid blue line) and the ground-based (dashed blue line) observations have close agreement, particularly in the summer months. The satellite CLW fraction is lower year round than the surface observations, which fits with the CPR missing $\sim 25\%$ of CLW events, as discussed in Section 2.3. The closer match between ground- and space-based observed fractions in summer could be due to the higher cloud water content improving detectability from space. The IC events (red lines) from the two platforms follow a similar pattern in the summer months, though the ground-based fraction is smaller. During the winter there is a clear majority of near-Summit IC events observed

from space. The surface observations, on the other hand, show a drop off in IC snow during winter, and at the same time have a minimum in CLW events. This results likely from the third, “indeterminate”, category present in ground-based Summit observations in P18, but not in 2BCCL, being more prevalent in winter.

A key takeaway of Fig 2.5, beyond general agreement between the two instrument platforms on the relative frequency of regimes, is the important role CLW events play in brightening and adding mass to the surface of the central ice sheet during the summer months. CLW events are roughly double the number of IC in July, and continue to dominate frequency in August, the highest month of accumulation at Summit (Bennartz et al., 2019).

2.4.2 Cloud Characteristics

The annual cycle of geometric cloud depth for IC and CLW snowfall events (Fig 2.6, a) demonstrates that these regimes are consistently physically distinct in all months of the year. The CLW clouds are on average much shallower than the IC clouds, which is consistent with previous understanding of these regimes (e.g. Morrison et al., 2012; P18). The mean IC geometric depth hovers around 4 km with two broad maxima: one centered around January and one around August. The mean CLW geometric depth is between 1.5 and 2.5 km, with a single peak in July-August. Looking at the monthly average and standard deviation (solid line and shaded region, respectively) for the full GIS, there is no overlap between the two regimes in any time of year.

Since the geometric cloud thickness is so distinct between the two regimes, it follows that the cloud water content will also be different. In this work we use $dB(Z_{path})$ as a proxy for IWP (see method section 2.2.2). Looking at the annual cycle of $dB(Z_{path})$ for the full GIS (Fig. 2.6, b), the IC monthly averages show one main peak between May and October. IC $dB(Z_{path})$ has particularly small inter-annual variability June through September, the months with highest $dB(Z_{path})$. In contrast, the CLW $dB(Z_{path})$ has a broader and shallower summer peak and larger year to year variation (shown by the broader shaded region and spread of monthly markers) compared to IC events.

For the clouds observed within 100 km of Summit Station, the annual cycle shows that the IC events are consistently thicker geometrically than CLW events (Fig 2.7, a), though with more inter-annual variability compared to the full GIS (illustrated by the relatively larger shaded region) and no discernable annual cycle. Using ground based remote sensing, Miller et al. (2015) also found no clear annual cycle in integrated thickness for clouds above Summit Station. The near-Summit satellite observations of $dB(Z_{path})$ (Fig 2.7, b) have increased variability between years relative to the full GIS. Though the IC clouds still have higher $dB(Z_{path})$ than CLW year round, both regimes have have much smaller monthly mean $dB(Z_{path})$ values near-Summit than for the full ice sheet. This implies decreased IWPs for both regimes near Summit relative to the rest of the GIS, consistent with the greater distance from moisture sources.

It is useful to look also at the distribution of individual snowfall events to understand the character of the clouds that make up the mean. The top row of Fig 2.8 is a collection

of histograms containing all of the observed snowfall over the GIS for the entire study period. From left to right we have: annual, winter, and summer time periods (a, b, and c, respectively). Overall, most observations of snowfall (70 %) over the GIS are coming from IC events; however, in the summer months, close to half (45 %) of the snow observed is produced in CLW events. Similar to the plot of the annual cycle, Fig 2.8, a, shows that overall IC and CLW snowfall event cloud have distinctly different geometric depths. However, the overlap in their distributions indicate that there are some individual IC events that are shallower and CLW that are deeper than is implied in the annual cycle plot. Each regime histogram is individually normalized to better focus on and compare the shapes of the distributions, rather than the magnitudes. The CLW clouds are remarkably invariant across seasons, with a narrow distribution and a peak between 1 and 2 km in geometric thickness (Fig 2.8, b, c). The tail of the CLW distribution changes between winter and summer — summer has a longer tail to the right of the peak, responsible for the slight increase in mean thickness for those months seen in Fig 2.6, a. The IC clouds have a broader range of geometric depths than the CLW, with a wide peak in the annual distribution between 2 and 5 km geometric thickness that becomes slightly thinner in winter (2-4 km) and thicker in summer (3-6 km). There is also a change in the skewness of the distribution, with a positive skew (peak to the left, tail to the right) in the winter and a negative skew (peak to the right, tail to the left) in summer. The difference in the shapes of the distributions means that the average cloud depth does not shift as much between seasons as the peaks in the distribution would imply. The distribution of cloud depths near Summit (Fig 2.8, bottom row) are noisier, but demonstrate consistency with

the full GIS results in both shape and seasonal characteristics.

The histograms of $dB(Z_{path})$ (Fig. 2.9) demonstrate the distinct nature of the two regimes, with clear differences in the IC and CLW event distributions. The CLW events are again quite invariant between the annual, winter, and summer plots for both the full GIS (top) and within 100km of Summit (bottom). GIS-wide, the CLW has a sharp peak at ~ 0 $dB(Z_{path})$, positive skew, and overall similarly shaped distributions during all three time periods. The GIS IC event distributions have broader peaks that are consistently at larger $dB(Z_{path})$ values than the CLW peak, and much higher values (~ 10 $dB(Z_{path})$) in summer. This indicates higher IWP year-round in the GIS IC snow events compared to CLW events, and an increased summer ice path for the IC events, coinciding with the peak in the annual cycle plot (2.6, b). The skewness of the IC events is again marked, with the annual having no strong skewness and winter and summer showing opposite skewness, positive and negative, respectively. This means that the $dB(Z_{path})$ of the most commonly present cloud (the mode) in the two seasons is more disparate than shown by the mean in the annual cycle. The near Summit distributions are again noisier compared to the full GIS, but are quite similar in overall behavior, though with relatively fewer values above ~ 10 $dB(Z_{path})$.

Taking the cloud geometric thickness and $dB(Z_{path})$ together, another distinction becomes clear: the GIS CLW events exhibit relatively constant characteristics throughout the year, while the GIS IC events are more seasonally dependent, within limits. IC events have a distinct annual cycle for both cloud geometric depth and $dB(Z_{path})$, but the variability

(shown by the shaded standard deviation) within that cycle is generally no larger than the CLW variability, and in the summer in particular the variation is smaller. The summertime $dB(Z_{path})$ increase in IC events is accompanied by only a small increase in geometric thickness, meaning the clouds are denser during this period.

While $dB(Z_{path})$ gives an estimate of the total ice content of a cloud, the distribution of that ice in the vertical profile can give insight into hydrometeor growth tendencies. As a reminder, by “growth” we refer to an increase in particle masses, an increase in number concentration, or a shift from small particles to large particles in the size distribution (or a combination thereof). Fig 2.10 contains two-dimensional (2D) histograms of CPR reflectivities as a function of height for each regime. The composite of all observed IC snow events (Fig 2.10, a) shows increasing reflectivity toward the surface, indicating growth from the top of the deep clouds moving down the column to the top of the blind zone. The IC histograms in the winter and summer (Fig 2.10, c and e, respectively) have narrower distributions for given heights compared to the annual, with generally higher reflectivities in summer but showing consistent growth patterns in both seasons.

The CLW snowfall does not have as defined a relationship between height and reflectivity (Fig 2.10, b), shown by the rounded distribution. The CLW winter and summer (Fig 2.10, d and f, respectively) histograms have similar, round distributions and reflectivity spreads, though the peak in height is slightly higher in winter ($\sim 2.5\text{-}3$ km AGL) than in summer (~ 2 km AGL). Unlike the IC distribution, the CLW shape does not display a

discernible growth pattern. Both the IC and CLW results are consistent with what P18 found using the MMCR from the ground.

2.4.3 Associated Atmospheric Circulations

The moisture required to produce GIS snowfall is not produced locally — evaporation over the snow- and ice-covered regions of the Arctic is negligible — so moisture must be imported from the lower latitudes (Jakobson and Vihma, 2010) and/or ice-free ocean surfaces during summer months. While there are certainly local factors to consider (topography, surface type, temperature, etc.), variations in atmospheric circulation have been determined to be the primary control on GIS snowfall accumulation (e.g. Alley et al., 1993, Chen et al., 1997, Kapsner et al., 1995). Knowing the large-scale meteorological conditions that are coincident with each snowfall regime can help better constrain both the present day mass balance of the GIS as well as predict how it might change in the future. In this section, we examine the atmospheric circulations associated with regime snowfall for four GIS regions: near-Summit, southeastern, western, and northern.

First we look at near-Summit cases to find the coincident atmospheric conditions that are able to bring IC and CLW events all the way to the center of the GIS. To be included as a case for one of the regimes, an individual Summit overpass needed to contain a minimum of 10 contiguous snowfall footprints (equivalent to ~ 15 km along-track) within 100 km of Summit Station, and of those footprints a minimum of 90 % had to be of that regime type. We then took only the strongest 50 % of the selected overpasses (described in Section 2.2.4), giving 159 IC cases and 43 CLW near-Summit cases.

The mean 500mb geopotential heights (GPH) for near-Summit IC events (Fig. 2.11a) display a trough-ridge feature with a gradient bisecting the GIS. The mean winds close to Summit are coming from the south-southeast. The 500 mb GPH anomaly (Fig. 2.11c) shows a dipole with higher than average heights in the North Atlantic and lower than average over the western GIS and Baffin Bay. The anomalous winds are strong relative to the mean and come from the south-southeast. These conditions are similar in character and magnitude to what P18 found when looking at IC events at Summit Station. The IC 500 mb mean and anomalous GPH patterns are consistent with low-level convergence advecting warm, moist air from the North Atlantic ocean surface vertically through the column and north over the steep southeast coast of Greenland. These conditions bear strong resemblance to synoptic conditions often credited with GIS snowfall (Chen et al., 1997, Rogers et al., 2004, Schuenemann et al., 2009, Serreze and Barrett, 2008).

The regional map of mean 500 mb GPH for near-Summit CLW cases (Fig. 2.11, b) indicates calm conditions, showing relatively uniform heights over the GIS and with low wind speeds around Summit coming from the south-southwest. The main feature of the CLW GPH anomaly (Fig. 2.11, d) is much higher than average heights over the entire GIS. Hanna et al. (2016) identified that persistent high pressure anomalies are consistent with increased GIS precipitation in reanalyses in the western and central regions. These CLW conditions are again consistent with what was found in P18. This overall picture of quiescent flow and large-scale subsidence is known for maintaining Arctic mixed-phase clouds (Morrison et al., 2012). While in this work we are focused on

precipitation production, it is worth noting that these conditions also have the potential to enhance melt over the GIS through radiative forcing (Van Tricht et al., 2016).

The strength of our satellite approach is that we can look beyond Summit station to extend the P18 surface-based analysis and examine conditions coincident with regime snowfall in areas without ground-based observatories. We start by looking at cases of snowfall in the northern GIS, defined here as basins 1.1, 1.2, 1.3, and 1.4. Shupe et al. (2013) and Castellani et al. (2015) found essentially no snowfall at Summit associated with northerly surface wind components. Similarly, P18 saw negligible northerly surface winds with IC cases and a very small component for CLW cases, though northerly surface winds did occur outside of precipitation events. This hints that the air-masses responsible for northern GIS snowfall do not move on towards the central GIS.

Choosing the strongest 50 % of overpasses for each snowfall regime during the study period, we have 1,125 IC cases and 452 CLW cases making up the composite maps for the northern GIS (Fig. 2.12). There are more cases in the northern GIS than any other region we examine because of the concentration of satellite overpasses (see Fig. 2.1), not because it snows more frequently there. The IC mean 500 mb GPH map (Fig. 2.12, a) contains a trough to the west of the GIS and very calm upper level winds in the northern GIS. The GPH anomaly map for IC cases (Fig. 2.12, c) has a dipole centered over the GIS with higher than average heights to the west of the GIS and a low centered on the northeastern coast, with the anomalous winds coming from the north into our basins of interest. In an analysis by Chen et al. (1997) looking at synoptic causes for GIS

precipitation, it was found that high precipitation in the northern GIS in 1987-88 was associated with a mean cyclone located in the Arctic Ocean close to the northeast coast of Greenland. The low anomaly in IC 500 mb GPH seen in Fig. 2.12, c is suggestive of a mean cyclone in that location.

The northern GIS CLW cases are associated with a markedly different circulation pattern. Much like the near-Summit CLW cases, the mean 500mb GPH for northern GIS CLW cases has relatively uniform heights and low wind speeds. There is a strong anomalous ridge centered over Baffin Bay extending over the full GIS in the GPH anomaly plot (Fig. 2.12, d), with high anomalous northerly winds similar to the IC cases. The high anomalous winds moving over the northern GIS are pointed southeast towards the center of the ice sheet, however the actual mean wind speeds present there are very low and coming from the west, indicating the CLW snowfall travels west to east in this region. This fits with previously mentioned work that showed snowfall in the central GIS does not come from the north (Shupe et al., 2013; Castellani et al., 2015; P18).

The western GIS is defined in this work as basins 6.1, 6.2, 7.1, 7.2, 8.1, and 8.2. Its composite (Fig. 2.13) includes 999 IC cases and 372 CLW cases. Again the mean 500 mb GPH for IC shows a trough to the west of Greenland (Fig. 2.13, a) and the mean for CLW is relatively flat (Fig. 2.13, b). The GPH anomalies for the IC cases again show a dipole, but in this case the high anomaly is now off the southeastern Greenland coastline and the low anomaly is west-northwest of Greenland. The location of the low is possibly suggestive of the mean cyclone found by Chen et al. (1997) located in Baffin Bay

and which they connected with increased snowfall in the central west GIS. The western GIS CLW events are associated with the same relatively flat 500mb mean GPH and high anomaly over the GIS (Fig. 2.13, b and d) seen in the northern and near-Summit composites. The anomalous high ridge and winds show on-shore flow in the central west GIS. In their work using reanalyses to look at Greenland blocking, Hanna et al. (2016) showed similar 500 mb GPH and wind speed anomaly plots to be associated with positive precipitation anomalies along the western coastline of Greenland.

Moving finally to the southeastern GIS, defined as basins 3.3, 4.1, 4.2, 4.3, and 5.0, the composites shown in Fig. 2.14 are made up of 422 IC cases and 114 CLW cases. For this region the IC mean 500 mb GPH (Fig. 2.14, a) shows the deepest trough of the four regions, similarly placed to the west of Greenland but now extending all the way to the southern tip. This is consistent with previous studies connecting north Atlantic stormtracks to heavy precipitation in the southeastern GIS (e.g. Berdahl et al., 2018, Chen et al., 1997, Schuenemann et al., 2009, Vihma et al., 2016). The IC anomaly plot (Fig. 2.14, c) has a strong dipole with the trough just to the west of the southern tip of the GIS and the ridge centered just east of Iceland. The anomalous winds associated with the dipole are high and flowing from the North Atlantic onto the southeastern GIS. This scenario is suggestive of lee cyclogenesis, where cyclones form in the lee of the topographic ridge running along the southern tip of Greenland (Rogers et al., 2004, Schuenemann et al., 2009). Lee cyclogenesis has been found previously to correlate with precipitation in the southern region (Chen et al., 1997, Schuenemann et al., 2009). Indeed, Berdahl et al. (2018) found that the position of the Icelandic low is a determining factor in the

amount of snowfall hitting the SE coastline, with up to a 40 % increase when the low is in its far west position, relative to its far east position. The CLW GPH mean (Fig. 2.14, b) has a very shallow trough-ridge feature, in the same location but much less distinct than for the IC events. The CLW anomaly (Fig. 2.14, d) shows a dipole, but the low is now fully off the continent, and most of the GIS is under an anomalous high that is directing onshore flow from the North Atlantic into the SE GIS.

In all of these regional composites, there are common themes for both the IC and the CLW cases. For each region the two regimes are related to clearly distinct circulation patterns. The IC anomalies tend to have a trough and ridge dipole centered around the particular region of interest with anomalous flow directed onshore into the region in a pattern that resembles previously identified cyclone activity. The 500 mb GPH anomalies for the CLW consistently show an anomalous ridge over the GIS, but centered in such a way that the anomalous winds are directing flow and moisture into the region from the nearest coastline. These results point to IC snowfall being consistently associated with cyclone activity while CLW snowfall occurs under quieter, high pressure scenerios that favor long lived Arctic mixed-phase clouds.

2.5 Conclusions

Using CloudSat and CALIPSO observations, we quantify the frequency and rate of snowfall over the GIS associated with two distinct microphysical regimes: snowfall produced

by fully glaciated clouds (IC) and snowfall produced by Arctic mixed-phase clouds containing super-cooled liquid water (CLW). Motivated by the results in P18, this study determines the relative contribution of the two precipitation regimes to the mass of the full GIS.

Comparisons with ground-based observations show that CloudSat's CPR is sensitive enough to detect most IC events ($\sim 95\%$) as defined at the surface. However the CPR struggles with the shallower CLW events, identifying a smaller fraction of those defined at the surface ($\sim 75\%$). These missed cases likely result in an overall underestimation of GIS snowfall accumulation, particularly for the CLW accumulation values. While a future satellite based measurement system may reduce the depth of the blind zone, these missed cases represent a persistent limitation for CloudSat's CPR.

We find that, in general, snowfall occurs most frequently along the steep orography of the GIS's SE coastline, and IC events make up the majority of annual snowfall frequency ($\sim 70\%$). Across the full GIS, IC snowfall is responsible for $\sim 80\%$ of the estimated annual 399 Gt yr^{-1} accumulation. The relative contributions of the two regimes vary by basin, but in all basins and seasons, IC dominates the snowfall mass.

CLW frequency peaks in summer, with $\sim 45\%$ of all GIS snowfall observations associated with liquid containing clouds during this season. Looking at cases near Summit Station, we find that CLW are more frequent than IC in July and August, agreeing with data gathered from ground-based instrumentation (P18).

By looking at the synoptic conditions coincident with each regime, we find that the IC events in all regions appear to be associated with cyclones interacting with the GIS, while CLW events are coincident with anomalously high 500 mb GPHs over the GIS. In all regions and for both IC and CLW events, the anomalous winds direct flow and moisture onto the GIS from the nearest coastline.

Snowfall over the GIS matters in the energy and water cycles because of the ability to add mass to the ice sheet and increase the surface albedo. With this work we show that during the 2007-16 period, IC events played the larger role in adding mass, but CLW's increased prevalence in the summer months has led to a nearly equal role in freshening the surface. While not the focus of this work, it is important to remember that CLW events have the competing surface effects of enhancing albedo with snow while the liquid bearing clouds also trap additional terrestrial radiation, potentially enhancing melt (McIlhattan et al., 2017, Van Tricht et al., 2016)

For nearly half a century, the GIS has experienced net mass loss (Mouginot et al., 2019). Snowfall is the only significant, positive contribution to the mass of the GIS, and while snowfall rates have been increasing in recent decades, it has not matched the increased loss due to climate warming (Zwally et al., 2011). The mean frequency and accumulation values in this study should not be viewed as a climatology, but as a snapshot of characteristics in a rapidly changing Arctic. However, this snapshot is useful in that it provides insights into the character of present-day snow events across the ice sheet and the dominant synoptic patterns that produce them. Lenaerts et al. (2019a) compared observations

from CloudSat to present-day model representation of GIS snowfall frequency and used those results to interpret the relevance of model predicted changes in future precipitation frequency. Mapping our regime based results onto predicted changes in synoptic patterns from climate models may yield additional insights into how this important source of ice sheet mass may change in a warmer climate.

2.6 Author Contributions

E. A. McIlhattan was responsible for the overall conceptualization and methodology of this work. She led the investigation, conducted the formal analysis of the satellite data, wrote the original draft, completed revisions based on co-author review, and completed the data visualization for Figures 1 - 10. C. Pettersen assisted with the conceptualization of the work, gave pre-publication critical review, and developed the methodology and completed the visualization for the reanalysis based atmospheric circulation patterns shown in Figures 2.11, 2.12, 2.13, and 2.14. N. B. Wood gave pre-publication critical review and developed the methodology and conducted the formal analysis for the evaluation of MMCR data to determine missed-cases over Summit Station, producing the data in Table 2.1. T. S. L'Ecuyer provided computing resources, pre-publication critical review, and assistance with the overall conceptualization and methodology for this work.

TABLE 2.1: Summary of CloudSat snowfall detection capability over Summit Station, Greenland based on averaged MMCR data for POSS detected snowfall. To mimic CloudSat detection we used: a height range of 960-1200 m, equivalent to the standard height of bin 5 of the CPR used in the 2CSP algorithm over land; and time average of 300 s, which at a moderate wind speed of 5 m s^{-1} is equivalent to the horizontal CPR footprint of $\sim 1.5 \text{ km}$.

Snowfall Event Type	# of Events	Total Fraction Missed	Mean Rate: Missed	Mean Rate: Detected
Total Snow Events	20,516	0.22	0.05	0.09
IC Only Events	3,545	0.05	0.05	0.10
CLW Only Events	9,777	0.25	0.05	0.10

TABLE 2.2: Summary of 2CSP accumulation estimates by GIS basin. All masses are in Gt yr^{-1} . The ‘summit100’ basin includes every observation within 100km of Summit Station. The first number is the total mass for the basin followed by the percentage contribution from each regime (IC%,CLW%).

Basin #	Annual Mass	Winter Mass	Summer Mass	Area km^2
1.1	12 (77 , 23)	4 (88 , 11)	8 (62 , 38)	131,115
1.2	7 (78 , 22)	2 (87 , 13)	4 (67 , 33)	63,773
1.3	5 (83 , 17)	2 (90 , 10)	3 (74 , 26)	46,152
1.4	2 (79 , 21)	1 (87 , 13)	1 (67 , 33)	17,536
2.1	29 (82 , 18)	11 (91 , 9)	17 (71 , 29)	274,220
2.2	6 (85 , 15)	3 (91 , 9)	4 (76 , 24)	51,196
3.1	23 (87 , 13)	9 (94 , 6)	14 (78 , 22)	148,090
3.2	14 (81 , 19)	8 (89 , 11)	6 (70 , 30)	35,619
3.3	31 (86 , 14)	18 (92 , 8)	13 (78 , 22)	73,232
4.1	30 (84 , 16)	18 (90 , 10)	12 (76 , 24)	64,669
4.2	30 (77 , 23)	20 (85 , 15)	10 (67 , 33)	46,802
4.3	24 (73 , 27)	18 (80 , 20)	6 (64 , 36)	33,326
5.0	30 (77 , 23)	18 (85 , 15)	12 (64 , 36)	49,738
6.1	19 (79 , 21)	9 (87 , 13)	10 (67 , 33)	49,909
6.2	36 (78 , 22)	18 (86 , 14)	18 (66 , 34)	136,902
7.1	24 (83 , 17)	11 (92 , 8)	13 (70 , 30)	95,213
7.2	30 (84 , 16)	12 (91 , 9)	18 (73 , 27)	130,027
8.1	42 (82 , 18)	14 (90 , 10)	28 (71 , 29)	241,556
8.2	6 (74 , 26)	2 (85 , 15)	4 (59 , 41)	33,497
summit100	3 (83 , 17)	1 (93 , 7)	2 (69 , 31)	31,416

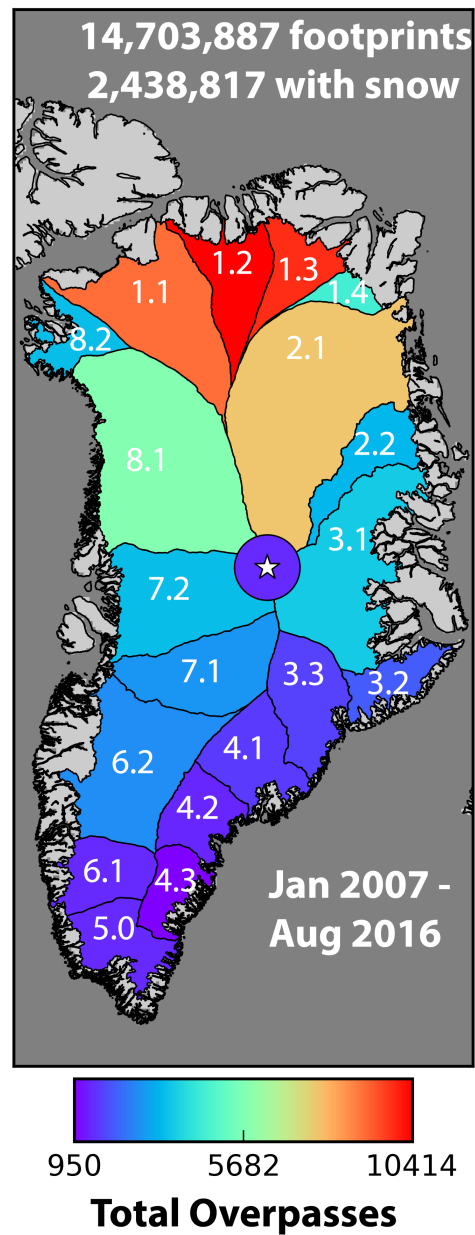


FIGURE 2.1: A summary of the CloudSat/CALIPSO satellite observations collected over the Greenland Ice Sheet (GIS). The GIS is divided into drainage basins as defined and numbered by the Ice Altimetry group at Goddard Space Flight Center. The color scale represents the total number of satellite overpasses in each basin during the full study period, January 2007 through August 2016. During that period, there were 14,703,887 individual satellite observations, 2,438,817 of which contained snowfall.

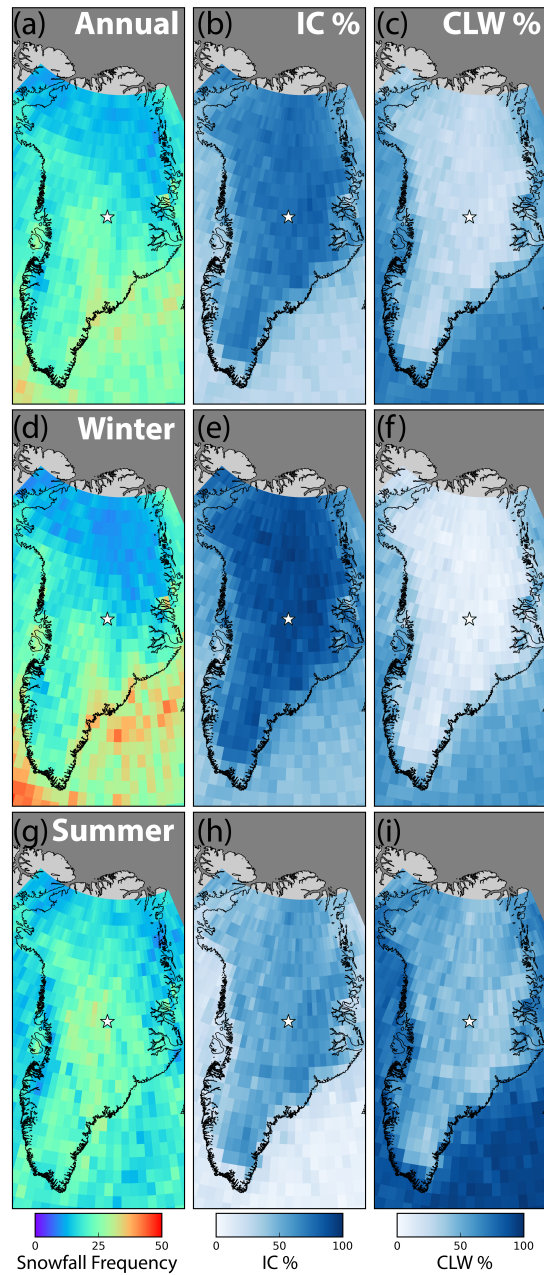


FIGURE 2.2: Snowfall frequency over the GIS defined as observations of snowfall divided by total observations in each gridbox. (a) is annual mean snowfall frequency using all observations from the study period, (b) is the percentage of total snowfall observations that were coincident with ice phase clouds, and (c) is the percentage of the total snowfall observations that were coincident with clouds containing liquid water. (b) and (c) sum to 100. (d) is winter mean snowfall frequency (Oct-Apr), with (e) and (f) the percentages of winter snowfall coincident with ice phase clouds and clouds containing liquid water, respectively. (g) is summer mean snowfall frequency (May-Sep), with (h) and (i) the percentages of summer snowfall coincident with ice phase clouds and clouds containing liquid water, respectively. The location of Summit Station is marked in each panel by a white star.

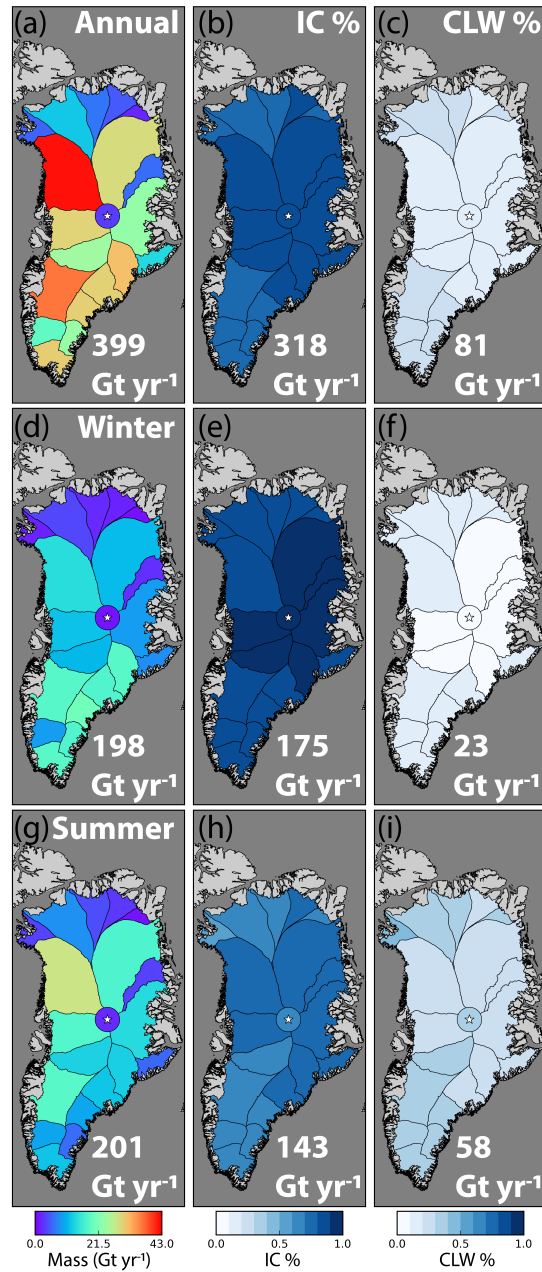


FIGURE 2.3: Snowfall mass contribution to the GIS. (a) is the annual average mass contribution broken down by basin, with the color scale representing Gt yr^{-1} for each basin and the total mass listed in the bottom left corner. (b) is the percentage of the snowfall mass produced by ice clouds, and (c) is the percentage of the mass produced by liquid containing clouds. The center ((d), (e), and (f)) and bottom ((g), (h), and (i)) rows are as the top row but for winter (Oct-Apr) and summer (May-Sep) months, respectively. The location of Summit Station is marked in each panel by a white star and the color of the circle surrounding it indicates the mass/percentage value for the area within 100km radius of the station.

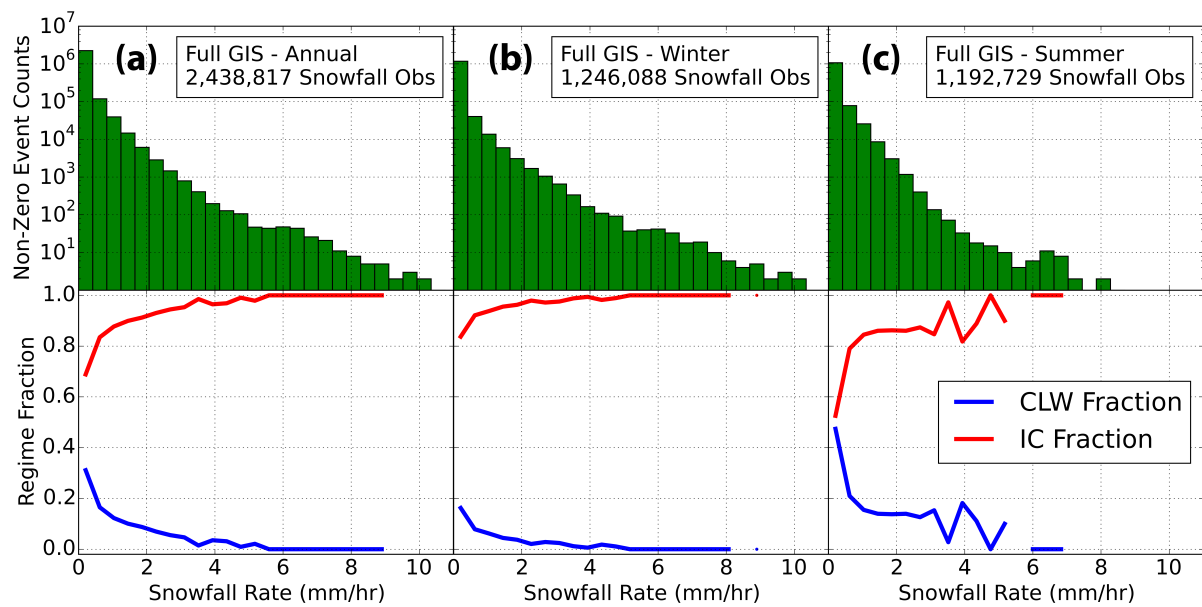


FIGURE 2.4: Snowfall rates for all observed snowfall. **(a)-top** is a histogram of the observed rates of all GIS snowfall from 2CSP (log scale), and **(a)-bottom** is the regime percent for each histogram bin. **(b)** and **(c)** are the same for GIS winter (Oct-Apr) and summer (May-Sep) months, respectively.

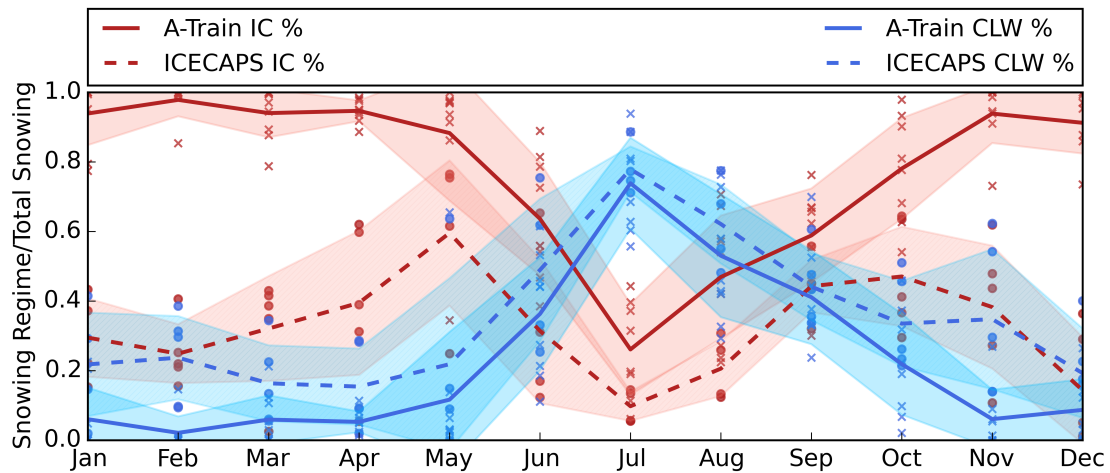


FIGURE 2.5: Annual cycle of regime fraction near Summit Station, Greenland. The regime fraction is the number of observations of one of the snowfall regimes (IC or CLW) divided by the total number of snowfall observations. A-Train values (solid lines, ‘x’ markers) shown for the near Summit annual cycle line plot are averages for all CPR footprints within 100km of Summit Station, Greenland. The solid lines represent the average of all observational years, each x depicting a single year’s monthly average. The shaded region surrounding each line is the standard deviation about the mean for the month. The red color is for the IC regime percent and the blue is for the CLW regime percent. For the A-Train data, the red and blue add to 1.0. The ICECAPS values (dashed lines, circle markers) are from vertically pointing instruments at Summit Station, also with markers representing a single year’s monthly average and the line being the mean of all years. The ICECAPS IC and CLW data do not add to 1.0 because of an additional category of ‘indeterminate’ (not plotted).

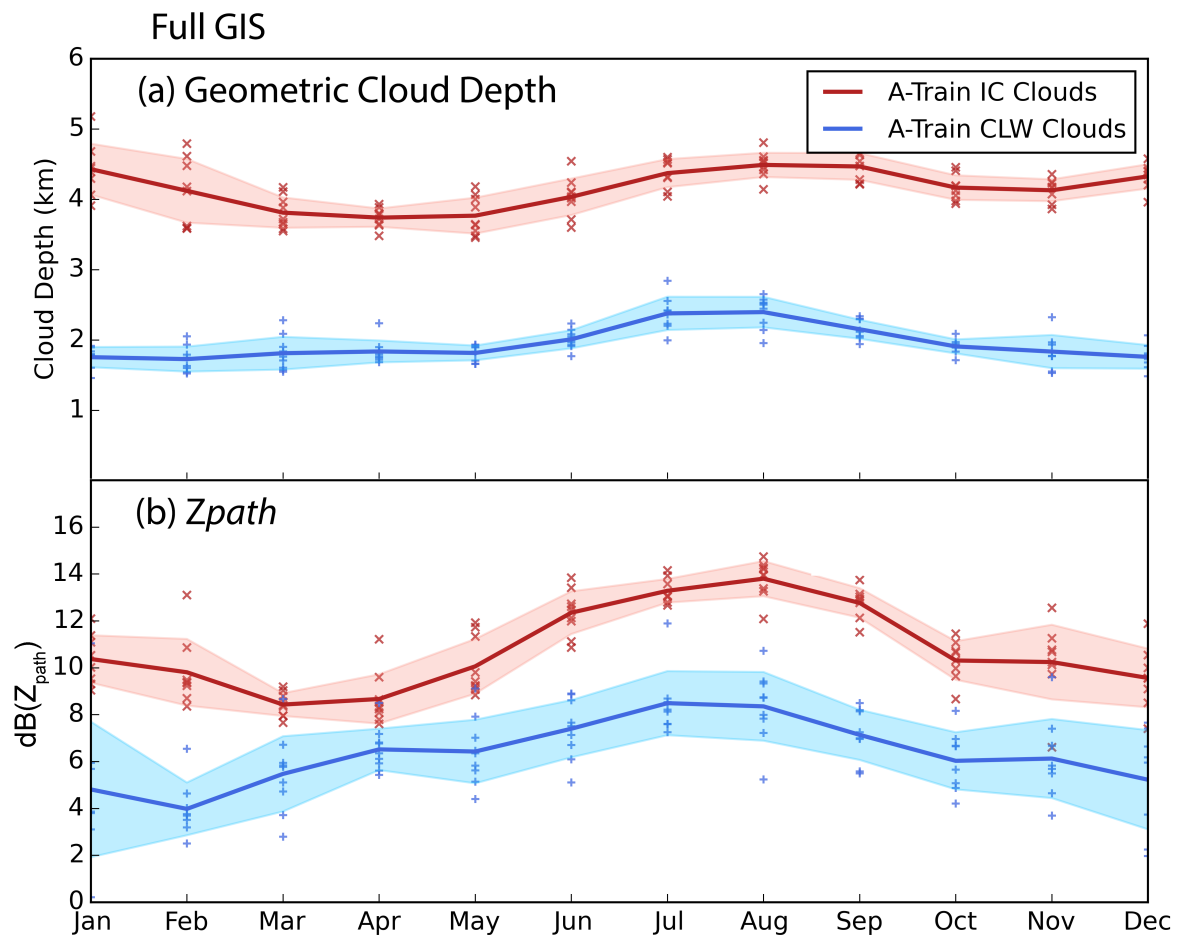


FIGURE 2.6: Annual cycle of GIS snowfall cloud characteristics. **(a)** the geometric cloud depth, and **(b)** the vertically integrated reflectivity for IC (red) and CLW (blue) snowfall observations. The solid lines represent the average of all observational years, each marker (x,+) depicting a single year's monthly average. The shaded region surrounding each line is the standard deviation about the mean for the month.

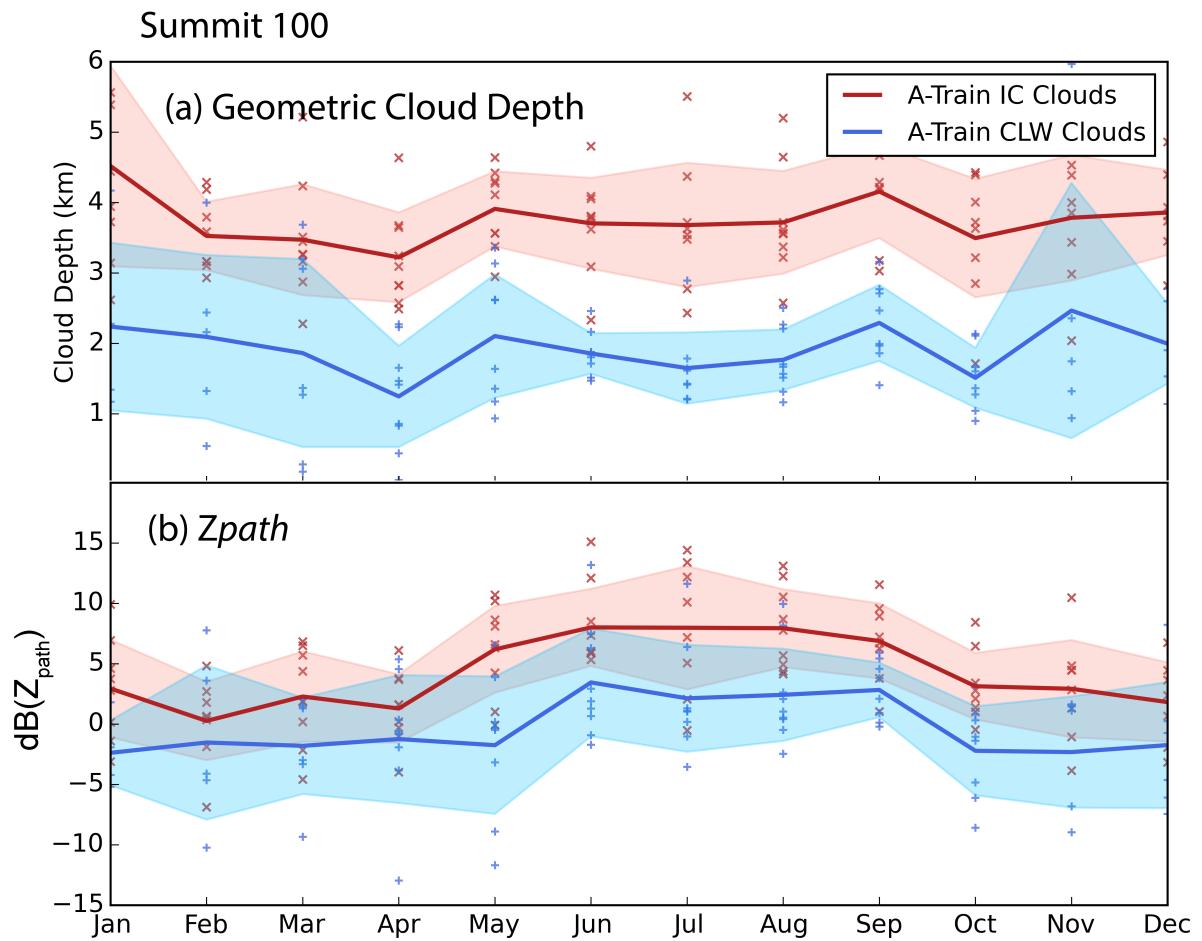


FIGURE 2.7: As in Fig 2.6 except only including observations within a 100 km radius of Summit Station.

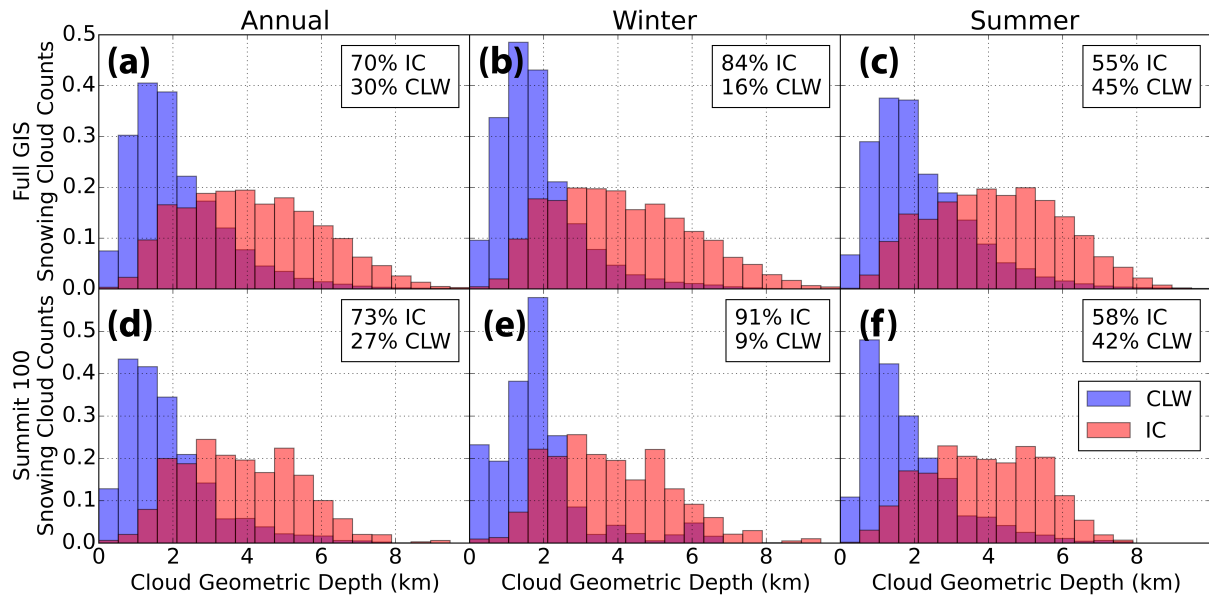


FIGURE 2.8: Histograms of precipitation regime geometric cloud depth. Red bins contain all footprints of IC snowfall and blue bins contain all footprints of CLW snowfall for each given season (Annual, Winter, and Summer) and region (Full GIS, Summit 100) as described in Fig 2.4. The histograms are normalized to highlight the distribution differences. The relative percentage of each regime is listed in the top right of each panel.

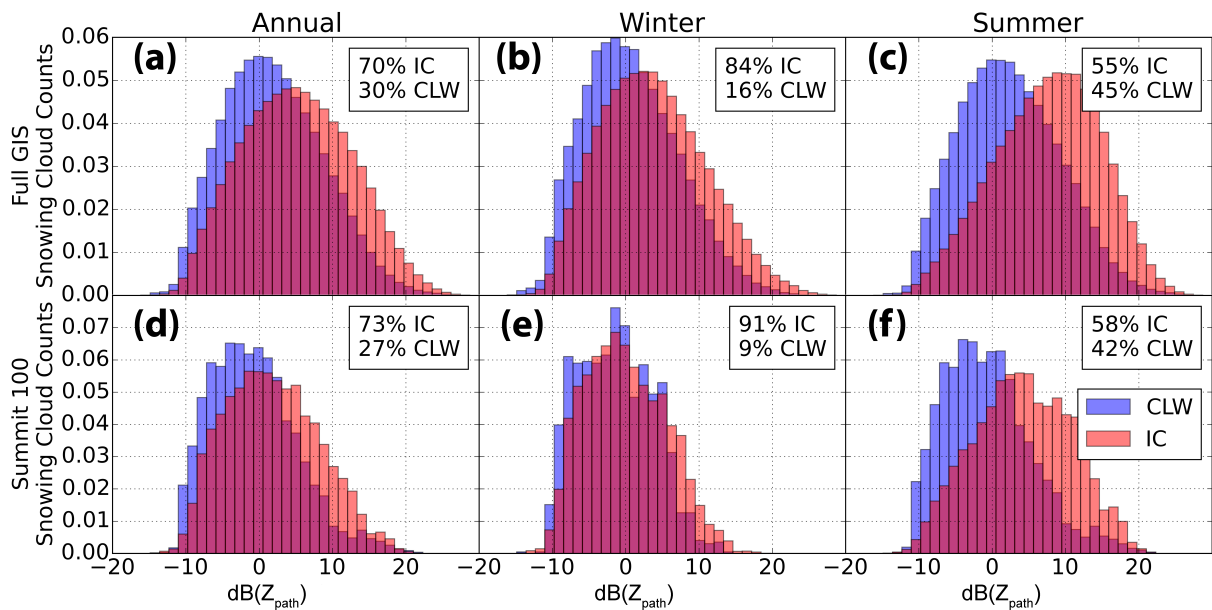


FIGURE 2.9: As in Fig 2.8 with $dB(Z_{path})$.

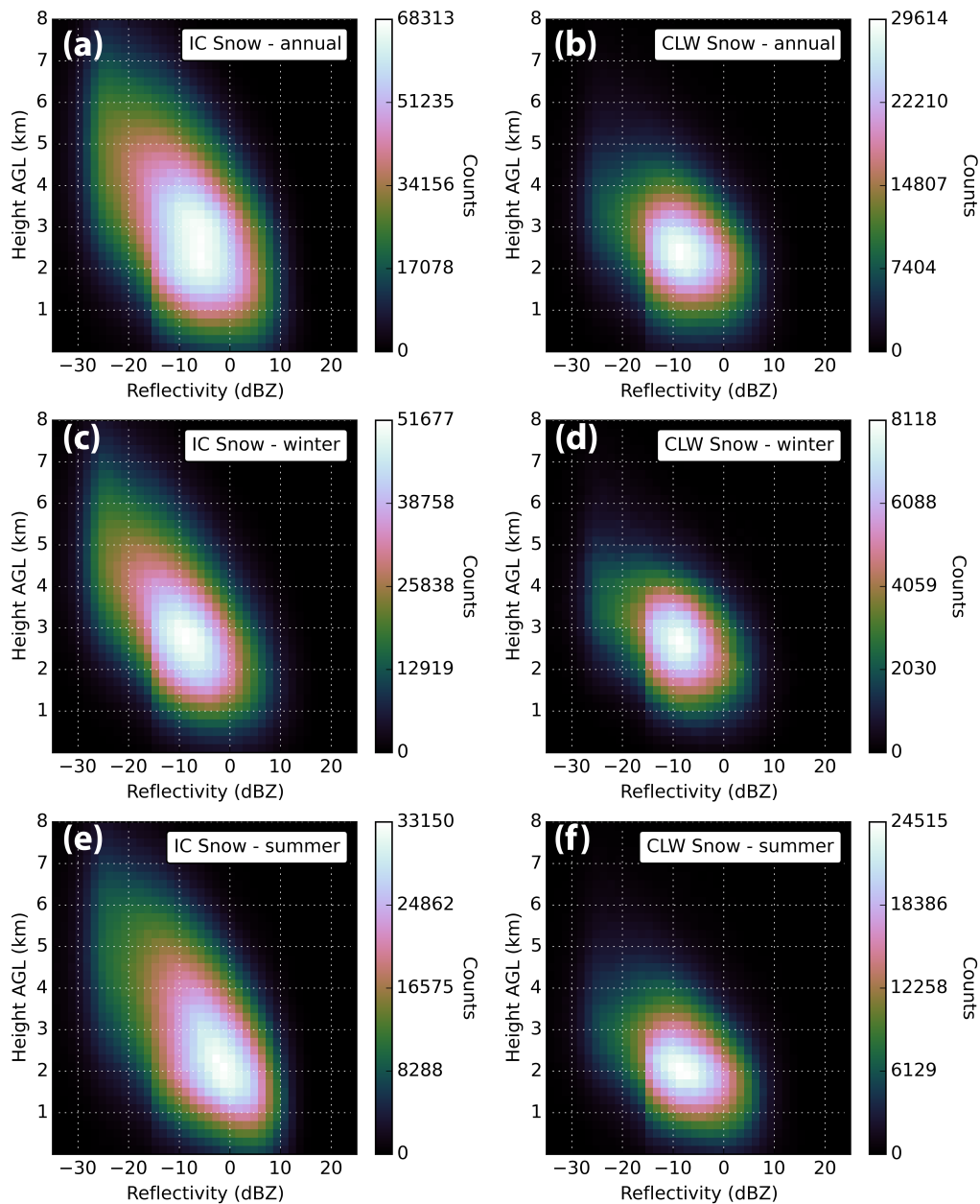


FIGURE 2.10: Composite two-dimensional histograms of CPR heights and reflectivities for the two snowfall regimes over the full GIS. The top row contains the entire annual cycle of events, including every footprint of snowfall detected during the study period, for IC **(a)** and CLW **(b)** events. The center row contains all wintertime (Oct-Apr) IC **(c)** and CLW **(d)** events, and the bottom row contains all summertime (May-Sep) IC **(e)** and CLW **(f)** events. There is a discontinuity apparent in each panel at ~ 15 dBZe. This is due to the 2CSP threshold of -15 dBZe for defining snowfall events. The shape and character of these plots compare well to Pettersen et al. (2018) Fig. 6.

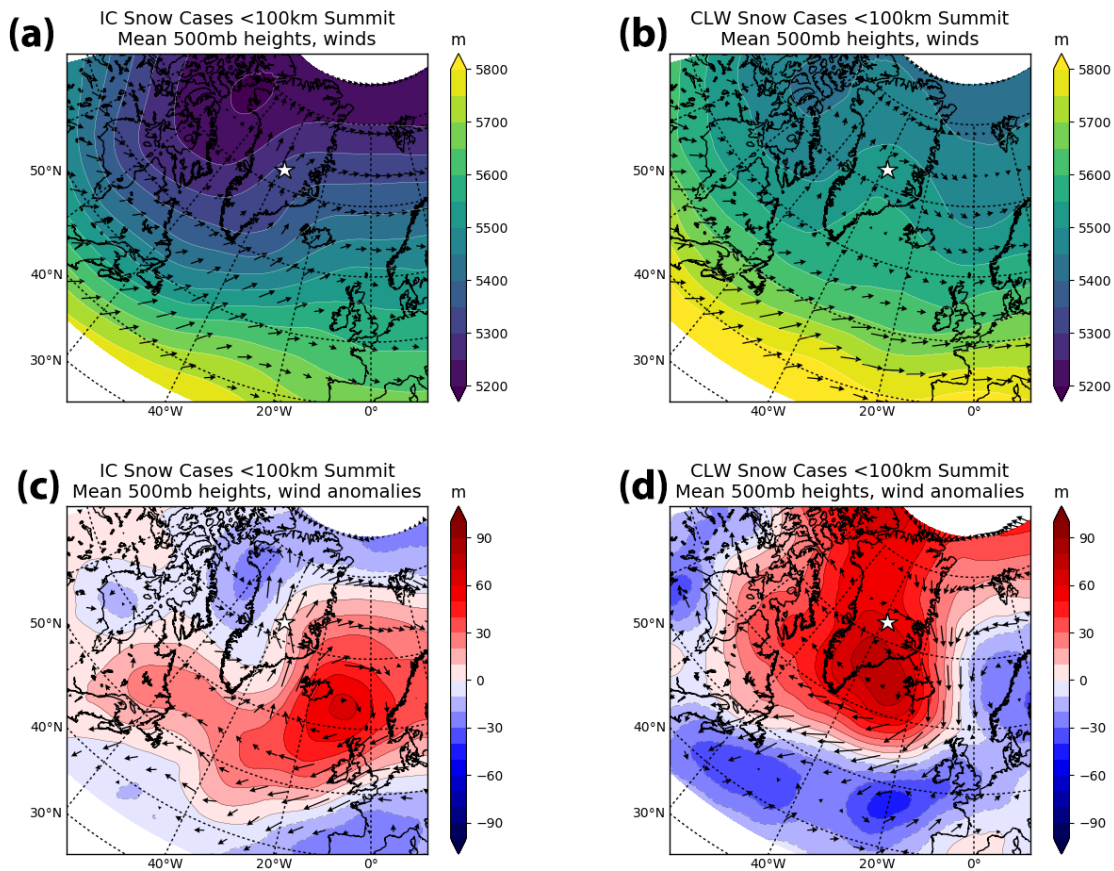


FIGURE 2.11: ERA5 derived mean and anomaly 500 mb geopotential heights (GPH) and winds for the strongest 50 % of precipitation events that occurred within a 100 km radius of Summit Station during the study period. **(a)** shows the average 500 mb GPH and winds for 159 IC events and **(b)** shows the same for 43 CLW events. **(c)** and **(d)** show the GPH and wind anomalies for the IC and CLW cases, respectively. These panels are all consistent with Pettersen et al. (2018) Fig. 11, which also shows a strong trough ridge for the IC snow cases and relatively calm, quiescent conditions for the CLW snow cases.

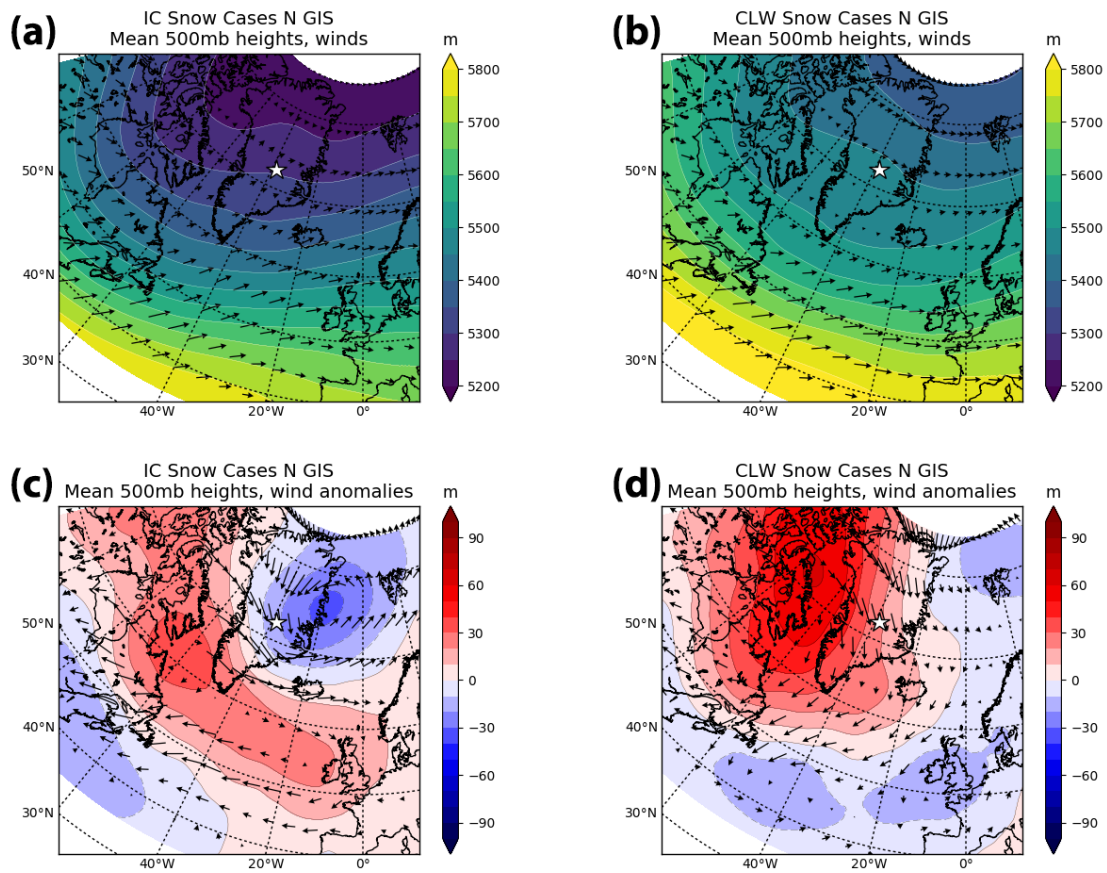


FIGURE 2.12: As in Fig. 2.11 for the northern GIS: basins 1.1, 1.2, 1.3, and 1.4.

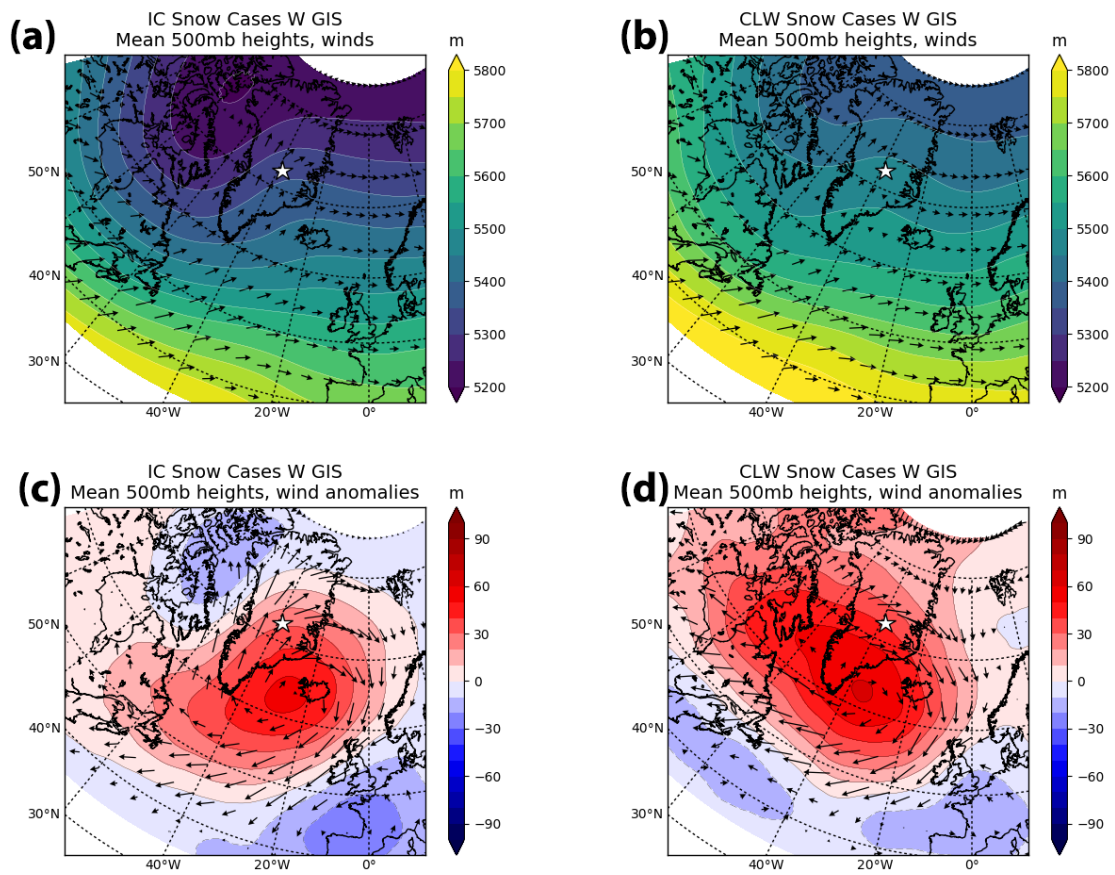


FIGURE 2.13: As in Fig. 2.11 for the western GIS: basins 6.1, 6.2, 7.1, 7.2, 8.1, and 8.2.

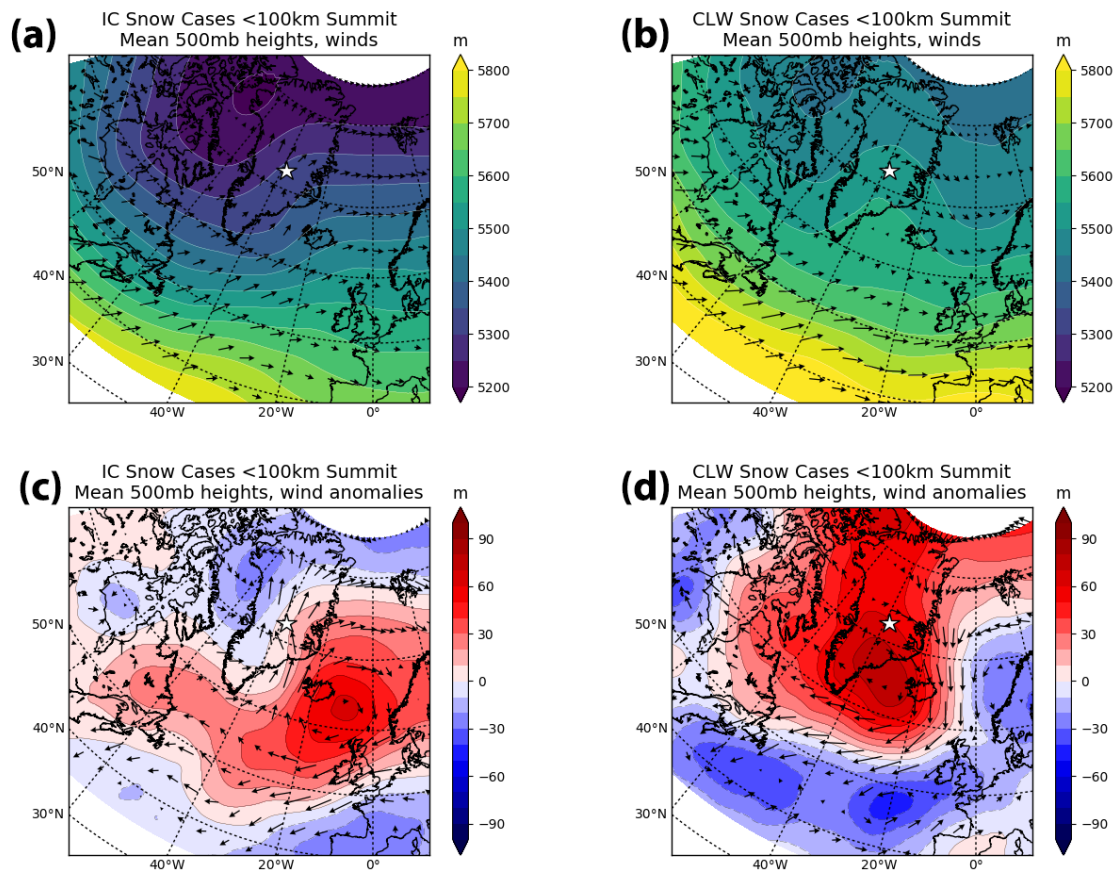


FIGURE 2.14: As in Fig. 2.11 for the southeastern GIS: basins 3.3, 4.1, 4.2, 4.3, and 5.0.

Chapter 3

Arctic Clouds and Precipitation in the Community Earth System

Model Version 2*

3.1 Introduction

The Arctic climate is undergoing rapid change (Serreze and Barry, 2011). Observations show that sea ice thickness and extent are decreasing (Onarheim et al., 2018), the Greenland Ice Sheet (GIS) is losing mass (Mouginot et al., 2019), and permafrost is melting (Schuur et al., 2015), all beyond what is expected from natural variability. Global climate models (GCMs) are essential tools for understanding the mechanisms driving these

* This chapter is being prepared as a manuscript for submission with coauthors J. E. Kay and T. S. L'Ecuyer

deviations and for simulating possible future scenerios which aid communities in planning and preparing for longer term climate changes.

As far back as 1896, Arrhenius was able to use relatively simple models and calculations to predict that increased carbon dioxide in the Earth's atmosphere would lead to global surface temperature increases, with enhanced warming of the high latitudes (Arrhenius, 1896). In the intervening years between Arrhenius' prediction and our ability to observe global warming, simple physical models (Budyko, 1969) and early GCMs (Manabe and Stouffer, 1980) continued to highlight the Arctic as a focal point for increased temperatures, due in large part to the ice albedo feedback— ice reflects more incoming solar radiation than ocean or land surfaces, so as the ice melts, more radiation is absorbed leading to more warming and more melt.

With advances in computational capabilities, modern GCMs have swiftly increased in complexity. This has led to models with more detailed representations of real world processes and forecasts, and a better ability to reproduce the present day climate in agreement with observations (Knutti et al., 2013). However, GCMs still struggle to represent some processes that occur on scales smaller than their spatial resolution. Differences between how individual GCMs parameterize sub-scale process contribute to the persistent, large inter-model spread for societally important predictions such as the magnitude of future warming (Knutti and Sedláček, 2012) and the onset of ice free arctic summers (Stroeve and Notz, 2015). Clouds in particular evolve and change rapidly on small spatial scales

so must be parameterized in GCMs. Clouds play an important role in Earth's water budget through precipitation and in Earth's energy budget by modulating the solar energy that reaches the surface and trapping terrestrial radiation that would otherwise escape to space. Clouds and their feedbacks were specifically identified in the Intergovernmental Panel on Climate Change (IPCC) Fifth Assessment Report (AR5) as one of the major remaining challenges in accurately modeling future climate scenarios (Vaughan et al., 2013).

The Community Earth System Model version 1 (CESM1) was one of the GCMs included in IPCC AR5 as part the Phase 5 Coupled Model Intercomparison Project (CMIP5). CESM1 contains fully-coupled atmosphere, ocean, land, and sea ice components that together simulate Earth's past, present, and future climate. Among the models included in CMIP5, CESM1 shows the closest match to observations of temperature and precipitation (Knutti et al., 2013). All components of CESM1 were recently updated by their respective modeling teams and a new wave model was added, resulting in the release of version 2 (CESM2). The atmospheric component was updated from the Community Atmospheric Model version 5 (CAM5) to version 6 (CAM6) (Gettelman et al., 2019).

While CAM5 overall represents Earth's atmosphere relatively well (Knutti et al., 2013), its representation of the Arctic atmosphere has some known issues. Relative to observations, CAM5 does not contain enough Arctic clouds (English et al., 2014, Kay et al., 2012). Supercooled liquid containing clouds (LCCs) are underrepresented in CAM5's Arctic (Cesana et al., 2015, Kay et al., 2016a, McIlhattan et al., 2017, Tan and Storelvmo,

2016), an issue shared by many GCMs (Cesana et al., 2012, Forbes and Ahlgrim, 2014). The LCCs that do occur in CAM5 produce snow too often relative to the observed frequency (McIlhattan et al., 2017). Downwelling longwave (LW) radiation at the surface is strongly connected with cloud presence and phase, thus is too low relative to both satellite derived Arctic estimates and measurements from a ground-based observatory on Greenland (McIlhattan et al., 2017). Also related to the insufficient LCCs, Kay et al. (2016a) found a summertime cold bias of 2–3°C in CAM5’s daily maximum of near-surface air temperatures at Summit, Greenland. In light of these known issues, improving polar cloud liquid representation was a goal for CAM6.

Studies comparing CESM1 with CAM5 and CESM2 with CAM6 (hereafter CESM1 and CESM2) have shown promising results in a variety of areas. The changes to CAM6 have increased correlation between model global monthly means and observations for a variety of atmospheric variables including: shortwave (SW) and LW cloud radiative effect; 30° S - 30° N rainfall; and temperature (Gettelman et al., 2019). Northern hemisphere circulation characteristics have improved, especially winter jet streams, storm tracks, and stationary waves (I. Simpson, 2019, personal communication). Lenaerts et al. (2019b) found that overall CAM6 has improved cloud representation over the GIS, in particular LCCs are simulated in CAM6 in similar distributions to observations whereas CAM5 simulates no LCCs over the GIS outside coastal regions.

While CAM6 simulates atmospheric conditions over the GIS well, that does not necessarily mean the the atmosphere over the remaining land surfaces, sea ice, or open ocean will

be well represented. Nor do improved global means guarantee Arctic improvement. In this work we explore differences between CESM1 and CESM2 in cloud behavior over the whole Arctic. In order to see changes in the mean state rather than responses to forcing, we use fully-coupled 1850s control runs from the two versions. CESM2 historical and present-day forcings are consistent with CMIP6 specifications, which are changed from the CMIP5 forcings used in CESM1 — so changes in the cloud fields in the present-day could be due to both forcing differences and model physics differences. By comparing constant 1850 pre-industrial control runs averaged over many years we can isolate the differences in the model representation of physical processes.

In the following sections, we aim to answer the questions:

- How has the frequency of Arctic LCCs changed in CESM2 relative to CESM1?
- How does the surface energy balance of the Arctic compare in the two versions?
- How has precipitation changed moving to CESM2, both in amount and spatial and temporal distribution?

We illustrate how the combined model updates have altered the representation of Arctic clouds and precipitation. It is beyond the scope of this work to relate individual changes to the model parameterizations or physics to changes in the Arctic. We include observational data in some plots to provide context for particular variables, but the goal of this work is to document changes in the mean Arctic state between CESM1 and CESM2.

3.2 Methods

3.2.1 CESM

Our focus is to compare the overall cloud representation of CESM1 and CESM2, so we first compare the basic state of clouds and precipitation from multi-century, stable, pre-industrial (1850s forcings) control runs for each version. In order to examine cloud properties that are not standard outputs for CESM, we have run fully-coupled 10 year branch simulations off of the control runs for both CESM1 and CESM2 with the necessary additional outputs but no change in configuration. The additional variables output are described in Table 3.1. All model outputs have a horizontal resolution of 1.25° longitude and $\sim 0.94^\circ$ latitude.

3.2.1.1 CESM1

For our CESM1 run, we use the configuration from the CESM Large Ensemble project which is described in detail in Kay et al. (2015). Components included in CESM1 are: atmosphere (CAM5), ocean (Parallel Ocean Program [POP], version 2), land (Community Land Model [CLM], version 4), sea ice (Los Alamos Sea Ice Model [CICE], version 4), land ice (Community Ice Sheet Model [CISM], version 1.9), and river (River Transport Model [RTM]).

3.2.1.2 CESM2

For our CESM2 run, we use the configuration described in Danabasoglu (2019). The components included are: atmosphere (CAM6), ocean (POP version 2, with physical improvements), land (CLM version 5), sea ice (CICE version 5.1.2), land ice (CISM version 2.1), river (Model for Scale Adaptive River Transport [MOSART]), and wave (OAA WaveWatch-III ocean surface wave prediction model [WW3]).

3.2.2 Satellite Observations

While this paper is focused on changes from one model version to another, it is helpful to anchor particular model variables with observed values to provide context. Details on how the observational dataset is compared to model output are presented in Section 3.2.3.

The observations leveraged in this work are derived from two instruments in the National Aeronautics and Space Administration A-Train satellite constellation: *CloudSat*'s 94-GHz Cloud Profiling Radar (CPR) and *CALIPSO*'s Cloud–Aerosol Lidar with Orthogonal Polarization (CALIOP) (532- and 1064-nm wavelengths). Together, these active sensors have provided vertical column information in the Earth's atmosphere between 82° S and 82° N since 2006 (L'Ecuyer and Jiang, 2010). Their combined skill allows for both the determination of Arctic cloud phase as well as precipitation characteristics below the cloud layer (Battaglia and Delanoë, 2013). The particular dataset used here was developed and detailed in McIlhattan et al. (2017) utilizing R04 versions of CloudSat

Data Processing Center data products and boundaries of 66.91 and 81.99° N for the Arctic. A satellite footprint is defined as containing an LCC if the nearest surface cloud layer in 2B-CLDCLASS-LIDAR is flagged liquid or mixed-phase. An LCC is defined as precipitating if 2C-PRECIP-COLUMN contains any of the following flags: Snow Certain, Mixed Certain, Rain Certain, and Rain Probable. The broadband surface radiation fluxes are from 2B-FLXHR-lidar. Satellite footprints from January 2007 to December 2010 were gridded to the CESM resolution before taking the area weighted averages used in this work. For specific details on the satellites, data products, and validation, refer to the methods section in McIlhattan et al. (2017).

3.2.3 Comparing Model Output and Observational Data

The primary purpose of this paper is to document changes in Arctic clouds and precipitation between CESM1 and CESM2. It is, never-the-less, useful to anchor the comparisons against observations to provide independent context for the results.

In this study, the Arctic is defined as 70-90° N. All model results shown in tables and line plots are area weighted averages of all grid boxes with centers $\geq 70^\circ$ N. When comparing to observations, the area defined as the Arctic is reduced to grid boxes with centers between 66 and 82° N to match the spatial extent of satellite observations described in Section 3.2.2.

When looking at clouds, model output and observations can not be directly compared. Both scale and sensitivity must be taken into account before a meaningful comparison can

be made (Kay et al., 2018). Clouds and their microphysical processes are parameterized in GCMs because they occur on scales far smaller than a single grid box. How a cloud is defined in an observational dataset depends on the sensitivity of the instrument used. Satellite simulators have been developed to bridge the gap between modeled and observed clouds (Kay et al., 2012), however, the satellite data used in this work is a combination of radar and lidar that is not currently available as a simulator package. To compare LCC frequency and LCC precipitation frequency between CESM and CloudSat/CALIPSO observations, we use the thresholds developed in McIlhatten et al. (2017). Specifically, model LCCs are defined as grid boxes containing 6 hourly instantaneous values $\geq 5 \text{ g m}^{-2}$ of vertically integrated cloud liquid ('TGCLDLWP'), and model LCCs are defined as precipitating if they have 6 hourly instantaneous precipitation values ('PRECT') $\geq 0.01 \text{ mm h}^{-1}$. If the frequency of LCCs is below 2 % in a given month that month is masked when calculating precipitation frequency to avoid a sampling bias.

It is important to remember that the model output for both CESM1 and CESM2 is from pre-industrial control runs, while the satellite data is from the modern era (2007-10). Since sea ice extent, greenhouse gas levels, surface temperatures, and other atmospheric variables are different in the modern era than they were in the 1850s, an exact match between the satellite and observations is neither expected or desired. Due to the differing time periods of the observations (2007-10) and the models (1850s pre-industrial control), an exact match is not expected and the observed values are a tool for discussing reasonableness of model values. Comparisons are meaningful because often times differences between present-day and pre-industrial are often much smaller than differences between

model and observations. Where available and appropriate, satellite observations are included to provide a present-day reference for the physically reasonable range of some variables for context.

3.3 Results and Discussion

3.3.1 Cloud Representation

Clouds play a key role in the Arctic surface energy balance, modulating the radiation received at the surface. LCCs in particular have a large impact on downwelling LW (Van Tricht et al., 2016) and are ubiquitous throughout the Arctic (Morrison et al., 2012). Too few Arctic LCCs is a known and documented issue for CESM1 (Cesana et al., 2015, Kay et al., 2016a, McIlhattan et al., 2017, Tan and Storelvmo, 2016). To assess Arctic LCC representation in CESM1 and CESM2, the frequency of Arctic LCCs (6-hourly instantaneous values $\geq 5 \text{ g m}^{-2}$ 'TGCLDLWP' divided by total number of instantaneous values) is shown in Fig 3.1. All line plots follow the same format: monthly mean model results for the full Arctic are depicted by a solid line while results for the reduced, satellite observation extent are depicted by a dashed line; individual monthly values are depicted by markers; and the shaded regions are the standard deviation about the mean. In all months, CESM2 (purple) has more than double the frequency of Arctic LCCs in CESM1 (red). The annual cycles for the two model versions show a similar shape, with LCCs at a minimum in winter and maximum in summer, peaking in July. Previous work showed that while CESM1 produced a reasonable spatial distribution of Arctic LCCs relative to

observations, the overall frequency was much too low (McIlhattan et al., 2017). CESM2 has undoubtedly increased the frequency of LCCs relative to CESM1.

We have included modern era observed values (blue line) in Fig 3.1 to show one physically reasonable annual cycle for Arctic LCCs. The 66 to 82° N area weighted model means (dashed red and purple lines in Fig 3.1) are qualitatively the same as the full Arctic (70 to 90° N) model values for LCC frequency so will not be separately discussed. The CESM2 1850s control run is similar in magnitude to modern era observations in all months except June through August. It is possible that wintertime Arctic LCC frequency has not changed much between the 1850s and today, thus CESM2 could be representing the frequency well in those months. In the summer and early fall months however, CESM2 contains more Arctic LCCs than observed. Open ocean and warmer temperatures favor Arctic LCCs, so we would expect the summertime modern era, with its increased temperatures and decreased sea ice, to have more LCCs relative to the summertime 1850s. Since 1850s CESM2 has more summertime LCCs than are observed in the modern era, it may now be overestimating relative to what is physically reasonable. This potential overestimation is also shown by the annual mean values (Table 3.2), with CESM2 having more than twice the LCC frequency of CESM1 (0.50 and 0.17, respectively for the reduced observational area) and higher than the observed value (0.45).

Does this increase in LCC frequency indicate an overall increase in Arctic cloudiness, or does it come at the expense of ice clouds? To explore this question, we look at the annual cycle of total cloud water (monthly mean ‘ICLDTWP’, Fig 3.2 (a)). Arctic total

cloud water (liquid + ice) is higher in CESM2 than CESM1 in all months. The two model versions have similarly shaped annual cycles, with relatively constant values from December through April and a peak around July and August. However, the absolute amount of Arctic cloud water in CESM2 is more than doubled in the winter months and more than quadrupled in September and October, relative to CESM1 values. The annual mean value has tripled, going from 0.023 kg m^{-2} in CESM1 to 0.074 kg m^{-2} in CESM2 (Table 3.2). Dividing the total water by phase, we see that the annual cycle of liquid cloud water (monthly mean 'TGCLDLWP', Fig 3.2 (b)) for both CESM1 and CESM2 are similar to the total cloud water, showing much more liquid in the new model version. Cloud ice water (monthly mean 'TGCLDIWP', Fig 3.2 (c)), on the other hand is decreased in CESM2 relative to CESM1, but noting the reduced value of the y-axis for cloud ice, the absolute value of the change is smaller for cloud ice than cloud water. Indeed, there is reduced cloud ice and increased cloud water in CESM2, but it is apparent that the increase in cloud liquid is due to an overall increase in Arctic cloud water, not simply a transition from cloud ice to cloud liquid. When comparing CESM2 representations of the modern era to equivalent observations over the GIS, Lenaerts et al. (2019b) found an overestimation of cloud liquid, further supporting the idea that CESM2 has potentially overcorrected LCCs in the Arctic.

3.3.2 Surface Radiative Fluxes and Temperature

With large changes in clouds, it is certainly interesting and important to also assess changes in radiation. In particular, with the substantial increase in Arctic cloud liquid

in CESM2 we expect increased downwelling LW due to enhanced trapping of terrestrial radiation and decreased downwelling SW at the surface due to enhanced reflection of incoming solar radiation. Since the LW and SW changes have competing effects, the total downwelling radiation as well as the surface and near surface temperatures could increase or decrease depending on which effect dominates.

3.3.2.1 Downwelling Radiation at the Surface

Looking first at the changes in downwelling LW (monthly mean 'FLDS', Fig. 3.3(a)), we see that CESM2 has consistently larger values year round, relative to CESM1, but maintains the same annual cycle shape. The annual means in Table 3.3 show that CESM2 has on average 20 W m^{-2} more downwelling LW at the surface than CESM1. The modern era observed values follow a similar annual cycle, but with larger values than both CESM1 and CESM2 in all months except June, July, and August where observations overlap CESM2 LW values. The peak values occur in July and August in all three datasets, which coincides with the peak in liquid cloud water discussed in Section 3.3.1.

The increase in cloud water in CESM2 has also impacted the SW reaching the Arctic surface (monthly mean 'FSDS', Fig 3.3(b)). Not only is the magnitude of the downwelling SW reduced in CESM2 relative to CESM1, but the annual variation has also changed. The largest reductions in SW occur in June, July, and August (Fig 3.3(b)), the same months with the largest cloud liquid increases (Fig 3.2(b)). In CESM1 there is a clear peak in downwelling SW in June, but in CESM2 that peak has shifted earlier and is

centered around May and June. In this case, the observed values more closely match the annual cycle of CESM1, having a clear June maximum and a smooth distribution around that peak. However, the observed annual mean of downwelling SW is closer to the reduced area mean for CESM2 than CESM1 (91, 94, and 115 W m^{-2} respectively, Table 3.3).

The annual mean total value of downwelling radiation (LW plus SW) in the modeled Arctic is 2 W m^{-2} less in CESM2 than CESM1 (315 and 317 W m^{-2} , respectively, Table 3.3). This is a relatively small change overall, indicating that the competing effects of SW and LW are nearly balanced. However, looking at the annual cycle of total downwelling radiation (Fig 3.3(c)), we can see that there are larger changes in individual seasons. In the late fall and winter (October through February) there is consistently more total radiation received at the surface in CESM2 relative to CESM1, consistent with the more frequent LCCs trapping more LW terrestrial radiation with no competing SW effect. Conversely, in the summer (June through August), CESM2 sees less total radiation at the surface than CESM1 owing in part to the increased cloud albedo from the greatly increased liquid water content. The observed values follow CESM1 closely in the spring, summer, and fall, and in winter the total downwelling radiation is higher than both CESM1 and CESM2. The total radiation mismatch between CESM2 and observations in June, July, and August, when taken with overabundance of LCCs in those same months (Fig 3.1), indicates that CESM2 has likely overcorrected and now simulates too much cloud liquid relative to the real world. Even so, the differing time periods of the observations and models should be kept in mind and connections between the datasets not be over interpreted.

3.3.2.2 Surface Temperature

While both the CESM1 and CESM2 data are 1850s control runs, it is clear that there are large differences in the mean cloud states which impact the surface radiation budget. The Arctic ocean, land, and ice surface temperatures are dependent on a variety of factors, of which downwelling radiation is only one (e.g. ocean circulation, sensible and latent heat fluxes, emissivity, etc.). The spatial and seasonal variations of surface temperature (monthly mean ‘TS’) are shown in Fig 3.4. Values for near surface air temperature (‘TREFHT’) are qualitatively similar to surface temperature in spatial distribution (not shown) and quantitatively similar in annual means (Table 3.3), thus only surface temperature is discussed hereafter. Due to the warm ocean currents of the North Atlantic, both model versions have in all seasons a region of open water containing above-freezing surface temperatures. Likewise, in both model versions the high and bright surfaces of the GIS are consistently the coldest in every season. Nevertheless, there are large scale differences in the surface temperatures of the simulated Arctic between CESM1 and CESM2 (Fig 3.4, right column). CESM2 has a 3 K higher mean annual Arctic surface temperature than CESM1 (255 and 258 K, respectively, Table 3.3), but that difference isn’t distributed evenly spatially or temporally. The largest difference in mean surface temperature is in winter (NDJ), when the CESM2 Arctic is nearly 4.5 K warmer than the CESM1 Arctic. In winter, the increase in surface temperature is fairly evenly distributed across the Arctic, with the exception of the North Atlantic which is colder in CESM2 relative to CESM1. In summer and fall, when the largest increases in CESM2 LCCs occurred, we can see a

concentration of warming over the sea ice at the north pole and the GIS. It should be noted that the global temperature in CESM2 is also higher than CESM1, though only by 1 K (Table 3.3). The modifications to CESM between version 1 and 2 have undoubtedly altered the mean state of Earth’s climate, including an overall warming that likely results largely from changes to the clouds.

3.3.3 Precipitation

McIlhattan et al. (2017) suggested that the low bias in the Arctic LCC frequency in CESM1 could be due to an overactive conversion of cloud liquid to snowfall. With the drastic increase in cloud liquid in CESM2, we expected that perhaps the precipitation frequency in LCCs would be reduced relative to CESM1. However, the annual cycle of precipitation frequency in LCCs (6-hourly instantaneous values of both $\geq 5 \text{ g m}^{-2}$ ‘TGCLDLWP’ and $\geq 0.01 \text{ mm h}^{-1}$ ‘PRECT’, divided by total number of 6-hourly instantaneous values of $\geq 5 \text{ g m}^{-2}$ ‘TGCLDLWP’) is very similar between CESM2 and CESM1 (Fig. 3.5(a)). The annual mean values in Table 3.4 show that both model versions have LCCs precipitating the majority of the time (66 and 65 % of the time for CESM1 and CESM2, respectively). Satellite observations, on the other hand, indicate that Arctic LCCs only produce precipitation 13 % of the time (Table 3.4) with very little variability temporally (Fig. 3.5(a)) or spatially (not shown). Ground based measurements from the GIS have supported the satellite derived LCC precipitation frequency (McIlhattan et al., 2017). The consistency of the observationally based values possibly indicate a fundamental constraint on the lifetime of LCCs, which CESM has not yet been

able to reproduce.

Looking at total precipitation frequency (6-hourly instantaneous values $\geq 0.01 \text{ mm h}^{-1}$ 'PRECT'), Fig. 3.5(b) shows that CESM2 has a higher mean precipitation frequency in all months, compared to CESM1. In winter and spring, the models' monthly means are similar in magnitude and there is considerable overlap of the monthly variability (shaded regions). Whereas in the summer and fall, CESM2 clearly precipitates much more often than CESM1 with no overlap in monthly variability. In the annual average, CESM2 precipitates 45 % of the time while CESM1 precipitates 38 % of the time (Table 3.4).

Many GCMs, including CESM1, have a notable history of precipitating too lightly, too often (Dai, 2006, Kay et al., 2018, Stephens et al., 2010, Terai et al., 2018), so it comes as a surprise that the updated version of CESM has more frequent precipitation, rather than less. The mean precipitation amount in the Arctic (6-hourly instantaneous 'PRECT') is the same in the two versions, 26 mm month^{-1} (Table 3.4), meaning that not only is Arctic precipitation overall more frequent in CESM2 than CESM1, it's also overall lighter. Comparing the annual cycles of frequency and amount (Fig. 3.5(b) and (c), respectively), we see that it is the winter and spring in particular when CESM2 has more frequent precipitation but less total precipitation relative to CESM1 meaning that the mean CESM2 precipitation event is even lighter in those seasons.

3.3.3.1 Snowpack on Sea and Land Ice

Given the consistent Arctic annual precipitation total between CESM1 and CESM2, we would expect similar values for the snowpack on Arctic sea ice ('SNOWHICE' where 'ICEFRAC' ≥ 0.5). However, we find that the snowpack on sea ice in CESM2 is consistently shallower than CESM1 (Fig. 3.6, top row). CESM1 has an annual mean water equivalent snow depth of 0.36 m, whereas CESM2 has 0.13 m. The seasonal plots of snow pack are qualitatively similar to the annual mean, so are not included here. The largest differences in snow on sea ice are centered around the north and northeastern coastlines of Greenland, stretching towards the north pole (Fig. 3.6, top right). This region is also where the snow depth is deepest in CESM1 (Fig. 3.6, top left), with a maximum grid box mean value of 2.88 m. In CESM2 the snow depth over sea ice is relatively low and uniform, with no grid box mean values above 0.47 m. DuVivier et al. (2019) found that CESM2-CAM6 historical simulations substantially underestimate both Arctic sea ice volume and sea ice extent relative to observationally based estimates.

While the mean snowpack on sea ice has undoubtedly decreased in CESM2, the snowpack on Arctic land surfaces ('SNOWHLAND' where 'LANDFRAC' ≥ 0.5 , Fig. 3.6, bottom row) has increased in the updated version. The annual mean water equivalent snow depth on land is 0.49 m in CESM1 and 4.33 m in CESM2. The majority of the increase is located over the GIS (Fig. 3.6, bottom right) where the the mean differences include increases in depth as large as 9.93 m. The temperature and elevation differences between the GIS and

the sea ice could perhaps explain some of the large difference in how the precipitation is interacting with the two icy surfaces. However, in CESM2 nearly all land surfaces in the Arctic have increases in snow depth relative to CESM1 whereas all sea ice surfaces have decreases. There is clearly a difference in accumulation and/or melt behavior between the two surface types. Lenaerts et al. (2019b) found that in simulations of the modern era, central GIS surface melt is similar but slightly stronger in CESM1 than CESM2.

3.3.3.2 Snowfall

To understand changes in the snowpack between CESM1 and CESM2, we must further separate Arctic precipitation into its two components: snow (the sum of convective and large scale snowfall 'PRECSC' + 'PRECSL') and rain (total convective and large scale precipitation ['PRECC' + 'PRECL'] minus snowfall ['PRECSC' + 'PRECSL']). The annual cycle of snowfall rates is shown in Fig. 3.7(a). Mean Arctic snow rates in CESM2 have decreased in all months save July and August where they have stayed the same, relative to CESM1. In the annual mean, CESM1 snows 20 mm month^{-1} and CESM2 snows 17 mm month^{-1} . The magnitude of the difference is small, but it illustrates a consistent divergence in the mean state of the two models. Over long periods of time and over the full Arctic, a small change in snowfall behavior can lead to large changes in accumulation.

Looking at the spatial distributions of Arctic snowfall (Fig. 3.8, top row), we see that the differences in snowfall (CESM2-CESM1) are predominantly negative over the open ocean

and sea ice, while they are generally positive over land with most of the large positive changes occurring over the central GIS. This opposite sign bias based on surface type fits with the differing snowpack biases discussed in Section 3.3.3.1. Knowing that the total annual precipitation in the two model versions is the same, the mean decrease of 3 mm month⁻¹ in snowfall must be made up for in increased rainfall.

3.3.3.3 Rainfall

Indeed, mean annual Arctic rainfall has increased from 6 mm month⁻¹ in CESM1 to 9 mm month⁻¹ in CESM2. Figure 3.7(b) shows that CESM2 rainfall has increased in all months, with the largest magnitude changes May through October. Spatially, the rainfall is increased in all of the Arctic save the North Atlantic and Baffin Bay. The central GIS has a small positive change while the sea ice regions and western GIS have moderate positive values (Fig. 3.8, bottom right). Lenaerts et al. (2019b) found that CAM6 simulated excessive rainfall over the coastal GIS in the modern era relative to observationally validated regional model data.

The Arctic surface temperature in CESM2 is higher than CESM1 (discussed in Section 3.3.2.2). However, the winter mean temperatures for both models are still well below freezing (~ 246 K) and temperatures over the sea ice are lower still (Fig. 3.4). So why is it raining in CESM2 across the Arctic in winter?

3.3.4 Cloud Liquid Tendencies

Tendency terms show the conversions that create and deplete cloud liquid and have been used previously to explore LCC prevalence in CESM polar regions (Kay et al., 2016b, McIlhattan et al., 2017). Figure 3.9 shows the mean Arctic vertical profiles for microphysical terms that create and deplete cloud liquid in CESM1 (solid lines), and those same values for CESM2 (dashed lines). The vertical axis is height in pressure units and the horizontal is the rate of creation/depletion. In both CESM1 and CESM2, microphysical processes ('MPDLIQ', black lines) overall deplete cloud liquid from the Arctic, primarily through the conversion to precipitation ('MPDW2P', blue lines). The conversion to precipitation has decreased everywhere in the column in CESM2 relative to CESM1, which helps to explain why the large increase in Arctic cloud liquid (Section 3.3.1) is not accompanied by a large increase in precipitation (Section 3.3.3).

While the microphysical processes overall act to remove cloud liquid from the Arctic in both models, there is a stark difference in behavior near the surface. CESM1 microphysics removes liquid in the whole column, but CESM2 microphysical processes actually produce cloud liquid below ~ 900 hPa. Sedimentation ('QCSED TEN') is entirely responsible for producing the near surface cloud liquid in CESM2. In CESM1 there was too little cloud liquid for sedimentation to play a large role in the cloud liquid tendency (solid brown line in Fig 3.9). Whereas in CESM2 sedimentation acts to remove cloud liquid from the upper levels of the atmosphere, bringing it towards the surface. At the surface, sedimentation in CESM2 produces cloud liquid at a mean rate of ~ 11 mg kg⁻¹ hr⁻¹.

Cloud liquid that sediments out of the bottom of the CAM6 atmosphere is converted to a precipitation flux. There is not a specific freezing mechanism for sedimenting condensate thus supercooled cloud liquid sedimentation from the bottom model layer is converted to a surface flux of liquid precipitation even in sub-freezing temperatures (A. Gettelman, personal communication).

The key results from the tendency terms presented in Fig 3.9 are: first, the direct conversion of Arctic cloud liquid to precipitation is reduced in CESM2 relative to CESM1, and thus the mean snowfall rate is also reduced; second, due to the increased sedimentation of Arctic cloud liquid in CESM2, the mean Arctic rainfall rate has also increased year round.

3.4 Conclusions

The pre-industrial control runs of CESM1 and CESM2 show distinctly different Arctic cloud, radiation, and precipitation characteristics. Previous studies documented that CESM1 produces too few LCCs relative to observations (Cesana et al., 2015, Kay et al., 2016a, McIlhattan et al., 2017, Tan and Storelvmo, 2016). CESM2 has addressed this issue, simulating LCCs at more than twice the frequency of CESM1. The increase in cloud liquid in CESM2 brings with it the qualitatively expected changes in downwelling surface radiation and temperature, simulating a warmer Arctic overall (3 K) with higher magnitude warming in winter months (4.5 K), relative to CESM1.

CESM2 LCC frequency for 1850s June, July, and August is higher than modern era observations, hinting that perhaps the model has overcorrected and is now producing too much cloud liquid relative to what's physically reasonable. In comparing modern era simulations with satellite observations Lenaerts et al. (2019b) found that CESM2 slightly overestimates liquid water path over the GIS in summer months. Our study has a mismatch of time periods and the Lenaerts et al. (2019b) study uses a single model realization to compare to observations, neither setup is able to say whether or not the observations fit within the intra-model variability for the observational years. A large ensemble is planned for CESM2, which will provide an opportunity to see if the observed values fit within the models internal variability or if indeed Arctic clouds have too much liquid in the updated version.

Less snow falls in the CESM2 Arctic than the CESM1 Arctic, with tendency terms showing the direct conversion of cloud liquid to snowfall has decreased. This addressed the issue of overactive snowfall in CESM1 LCCs identified by McIlhattan et al. (2017). However an increase in cloud liquid sedimentation in CESM2 has resulted in more rain, even in sub-freezing winter temperatures. The decrease in snowfall and increase in rain has lead to unchanged total precipitation amounts in CESM1 and CESM2, though the snowpack on sea ice has decreased dramatically.

In this work we chose to compare 1850s, pre-industrial control simulations of the two model versions in order to focus on changes in the mean state of modeled cloud and precipitation. Gettelman et al. (2019) showed that cloud feedbacks in CESM2 have led

to an increased equilibrium climate sensitivity, meaning that a doubling of CO₂ has a larger impact on surface temperatures in CESM2 than CESM1. With both the increased mean Arctic temperature in CESM2 (+3 K) and the increased climate sensitivity, it is reasonable to extrapolate that the CESM2 Arctic will be more sensitive to greenhouse gas emissions and perhaps see greater magnitude warming in future projections. The upcoming large ensemble will allow this hypothesis to be explored in greater detail.

The Earth science community has known that the Arctic is a focal point for global warming for more than a century. As GCMs improve, including more detailed physical processes and realistic parameters, modern day representations approach observational values and our confidence in future projections rise Knutti et al. (2013). CESM2 simulates a different Arctic than CESM1, it has addressed the long standing issue of too few LCCs, but also produces wintertime rain in locations that are not physically reasonable. In a model as complex and interconnected as CESM, progress is not likely to be simple or linear, but the trajectory is towards a better understanding of the Earth's climate.

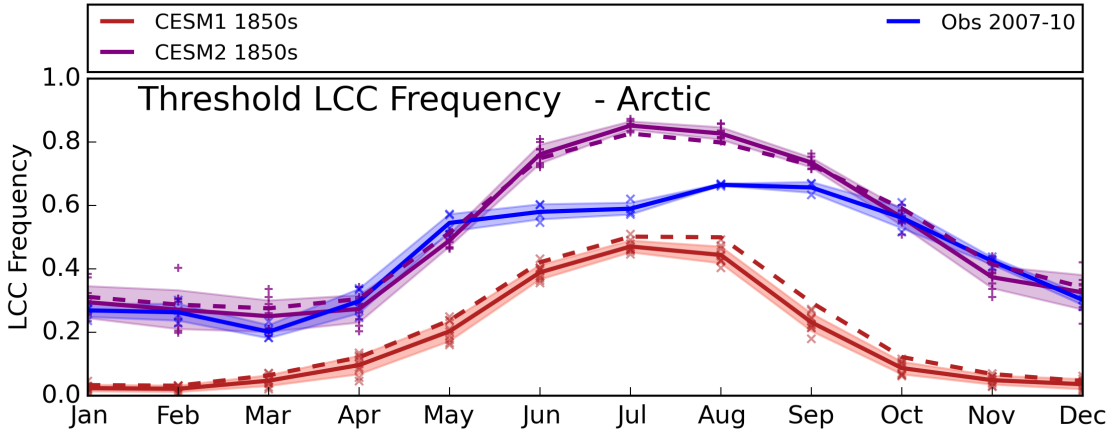


FIGURE 3.1: Annual cycle of liquid containing cloud (LCC) in the Arctic. The solid lines for CESM1 (red) and CESM2 (purple) illustrate the mean values for the monthly area weighted averages for all grid boxes between 70°N and 90°N from the 10 year branch simulations of their respective 1850s control runs. The dashed lines are also for CESM1 and CESM2, but for for the area between 66 and 82°N , for comparison with observations. The blue line represent the average of 2007-10 CloudSat/CALIPSO observations. The markers surrounding the lines each depict a single year's monthly average. The shaded regions denote the standard deviation about the mean for the month, showing the inter-annual variability.

TABLE 3.1: Summary of high-frequency and tendency term CESM variables used in this analysis.

Variable	Description	Native Units	Output Type
'TGCLDLWP'	Total grid-box cloud liquid water path	kg m^{-2}	6-hourly instantaneous
'TGCLDIWP'	Total grid-box cloud ice water path	kg m^{-2}	6-hourly instantaneous
'PRECT'	Total (convective and large-scale) precipitation rate (liq + ice)	m s^{-1}	6-hourly instantaneous
'MPDLIQ'	CLDLIQ tendency - Morrison microphysics	$\text{kg kg}^{-1} \text{s}^{-1}$	Monthly Mean
'MPDW2P'	Water \leftrightarrow Precip tendency - Morrison microphysics	$\text{kg kg}^{-1} \text{s}^{-1}$	Monthly Mean
'MPDW2I'	Water \leftrightarrow Ice tendency - Morrison microphysics	$\text{kg kg}^{-1} \text{s}^{-1}$	Monthly Mean
'MPDW2V'	Water \leftrightarrow Vapor tendency - Morrison microphysics	$\text{kg kg}^{-1} \text{s}^{-1}$	Monthly Mean
'QCSEDTEN'	Cloud water mixing ratio tendency from sedimentation	$\text{kg kg}^{-1} \text{s}^{-1}$	Monthly Mean

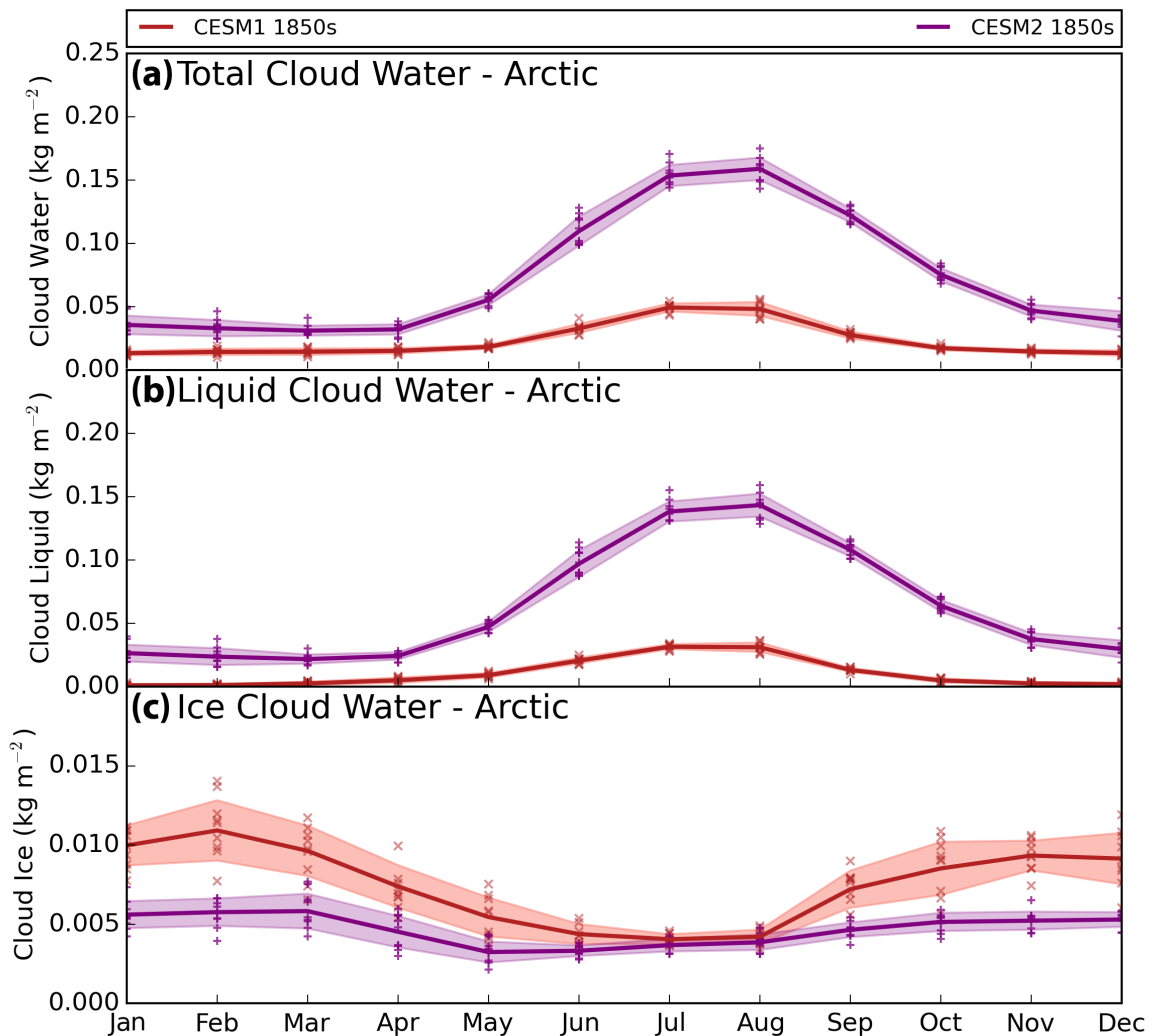


FIGURE 3.2: As in Fig 3.1 for the annual cycles of (a) total cloud water, (b) liquid cloud water, and (c) ice cloud water. Note the same y-axis is used in (a) and (b), but (c) is reduced.

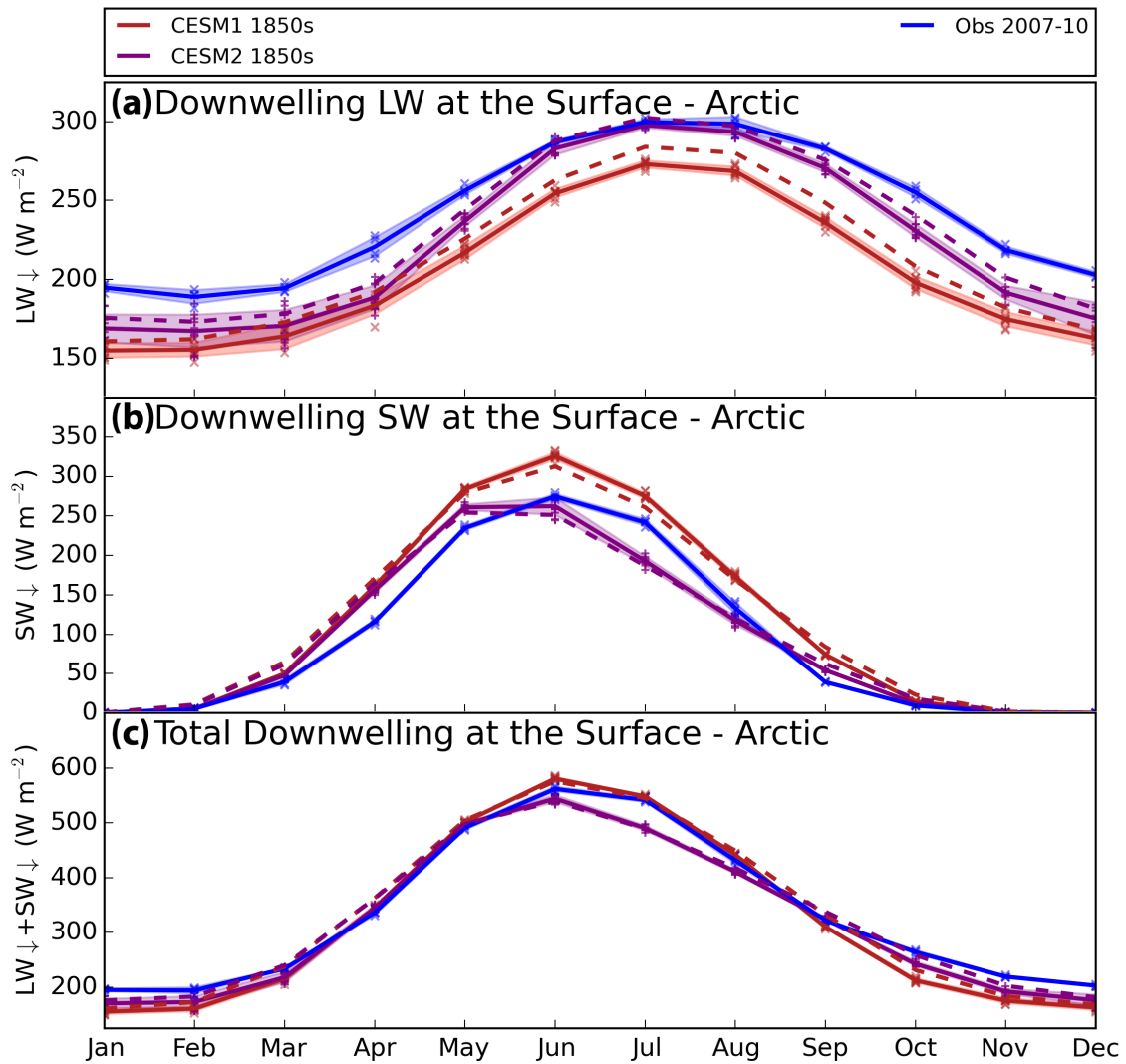


FIGURE 3.3: As in Fig 3.1 for the annual cycles of (a) downwelling LW at the surface, (b) downwelling SW at the surface, and (c) total downwelling radiation at the surface (LW+SW). Note each y-axis different.

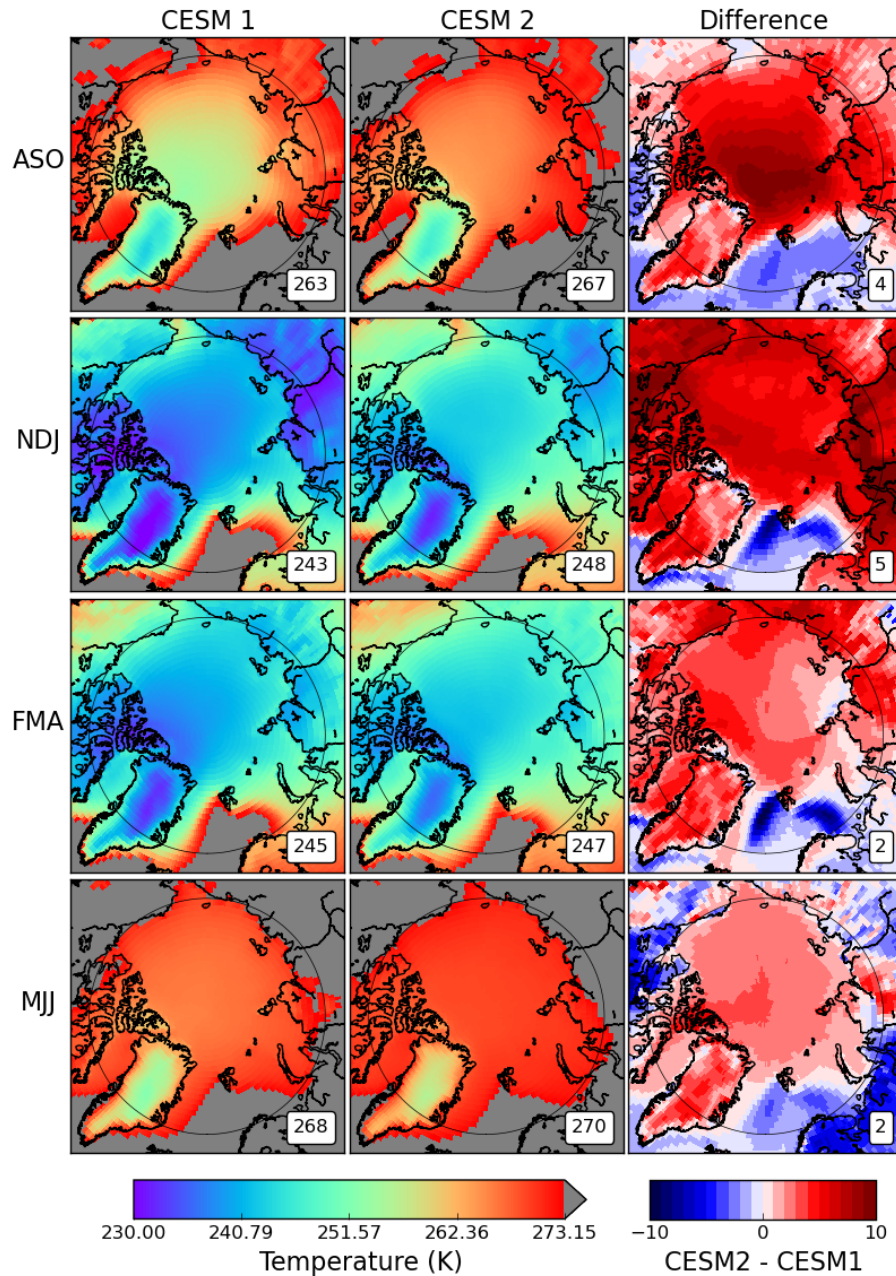


FIGURE 3.4: Seasonal averages of surface temperature in the Arctic. Seasonal divisions were chosen to capture sea ice minimum (August, September, October, top row) and sea ice maximum (February, March, April, third row). The plots for CESM1 (left column) and CESM2 (center column) are means from the 10 year branch simulations of their respective 1850s control runs. The difference plots in the right column are CESM2 minus CESM1, with red (blue) values showing increases (decreases) in temperature in CESM2 with respect to CESM1. The area weighted averages for the study area (70° N and 90° N) are shown in the lower right of each map.

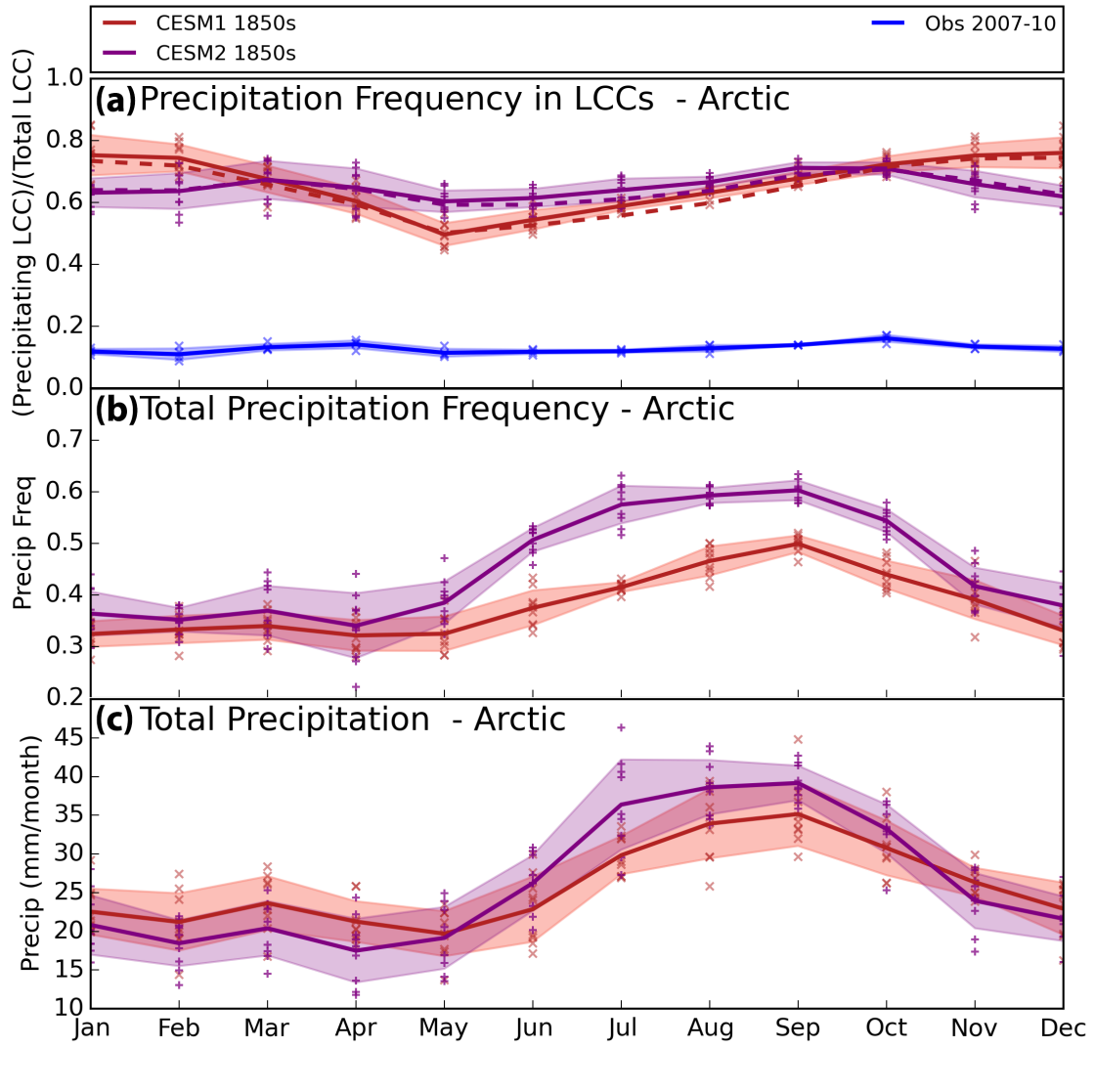


FIGURE 3.5: As in Fig 3.1 for the annual cycles of (a) precipitation frequency in LCCs, (b) total precipitation frequency, and (c) total precipitation. Note each y-axis different.

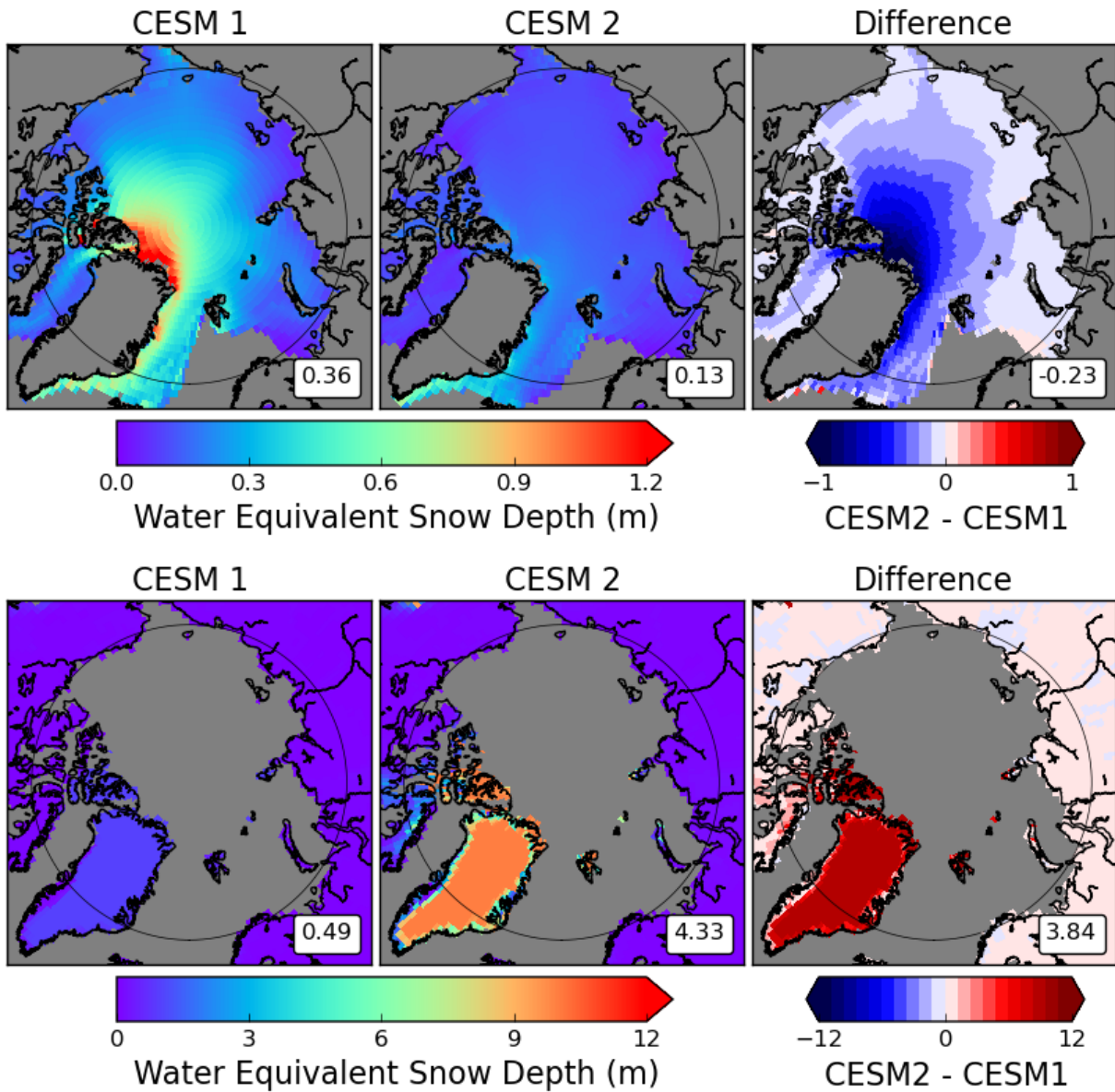


FIGURE 3.6: Annual averages of water equivalent snow depth on sea ice (top row) and land (bottom row). The plots for CESM1 (left column) and CESM2 (center column) are means from the 10 year branch simulations of their respective 1850s control runs. The difference plots in the right column are CESM2 minus CESM1, with red (blue) values showing increases (decreases) in snow depth in CESM2 with respect to CESM1. The area weighted averages for the study area (70° N and 90° N) are shown in the lower right of each map.

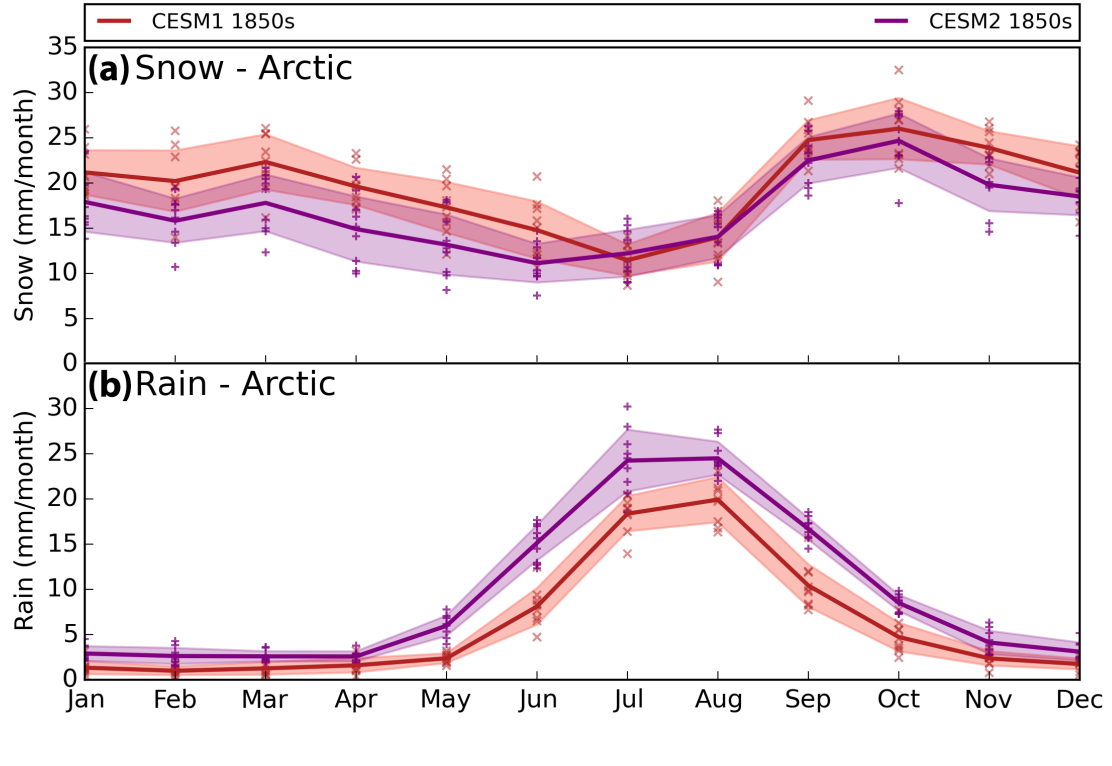


FIGURE 3.7: As in Fig 3.1 for the annual cycles of **a.)** snowfall, and **b.)** rainfall. Note the y-axes are the same.

TABLE 3.2: Summary of annual mean values of Arctic cloud properties. The \pm value is the standard deviation of the monthly mean values. The top section contains area weighted means for the full modeled Arctic ($70\text{-}90^\circ$ N) while the bottom section contains the area weighted means for the observed Arctic ($66.5\text{-}82^\circ$ N)

Dataset	Spatial Region	Time Period	LCC Frequency	Total Cloud Water (kg m^{-2})	Cloud Liquid Water (kg m^{-2})	Cloud Ice Water (kg m^{-2})
CESM1	$70\text{-}90^\circ$ N	1850s Control	0.17 ± 0.16	0.023 ± 0.013	0.010 ± 0.011	0.0075 ± 0.0024
CESM2	$70\text{-}90^\circ$ N	1850s Control	0.50 ± 0.22	0.074 ± 0.047	0.063 ± 0.044	0.0047 ± 0.0009
CESM1	$66.5\text{-}82^\circ$ N	1850s Control	0.20 ± 0.17	-	-	-
CESM2	$66.5\text{-}82^\circ$ N	1850s Control	0.51 ± 0.21	-	-	-
Observations	$66.5\text{-}82^\circ$ N	2007-10	0.45 ± 0.16	-	-	-

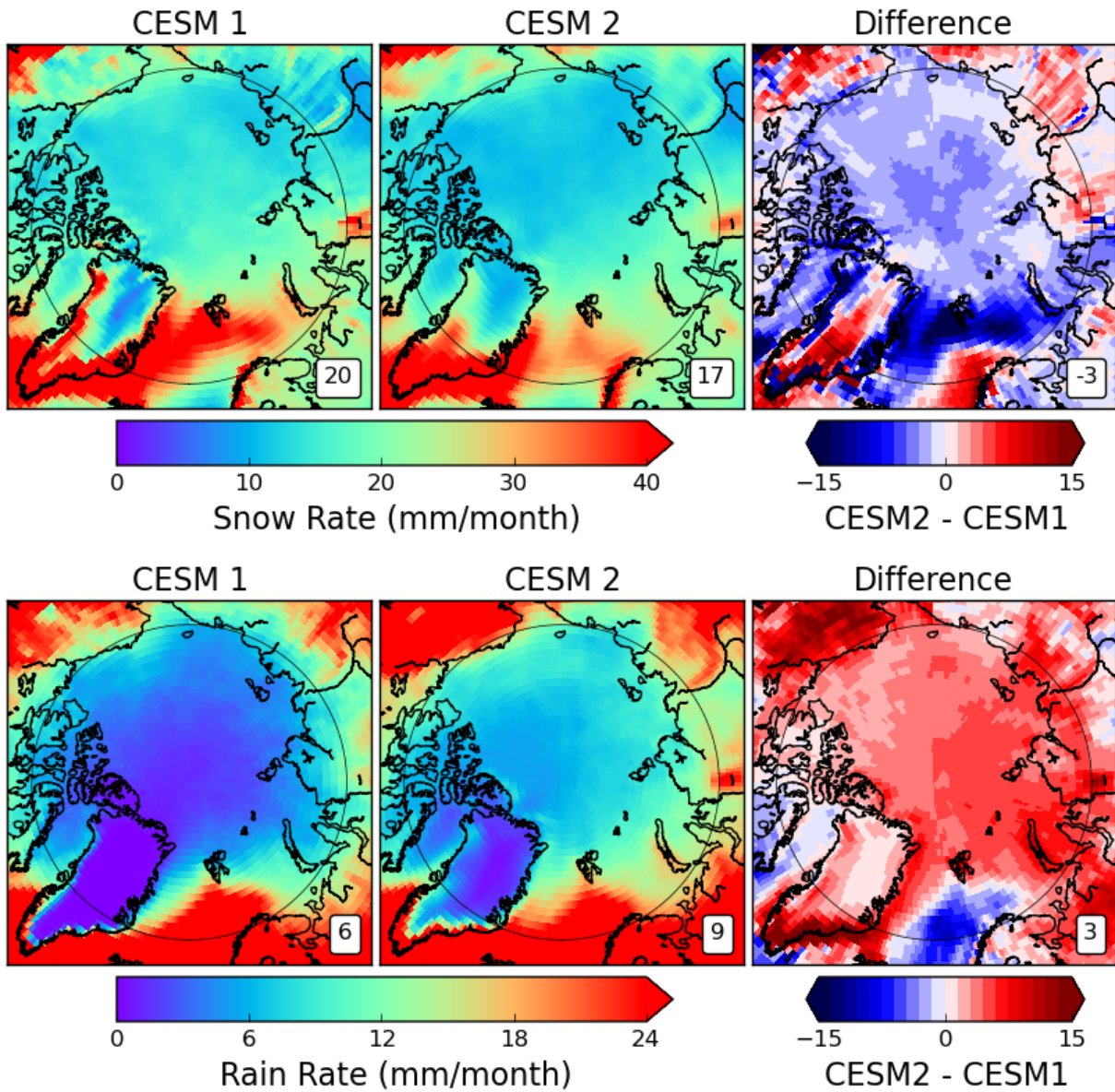


FIGURE 3.8: As in Fig. 3.6 for snow rate (top row) and rain rate (bottom row).

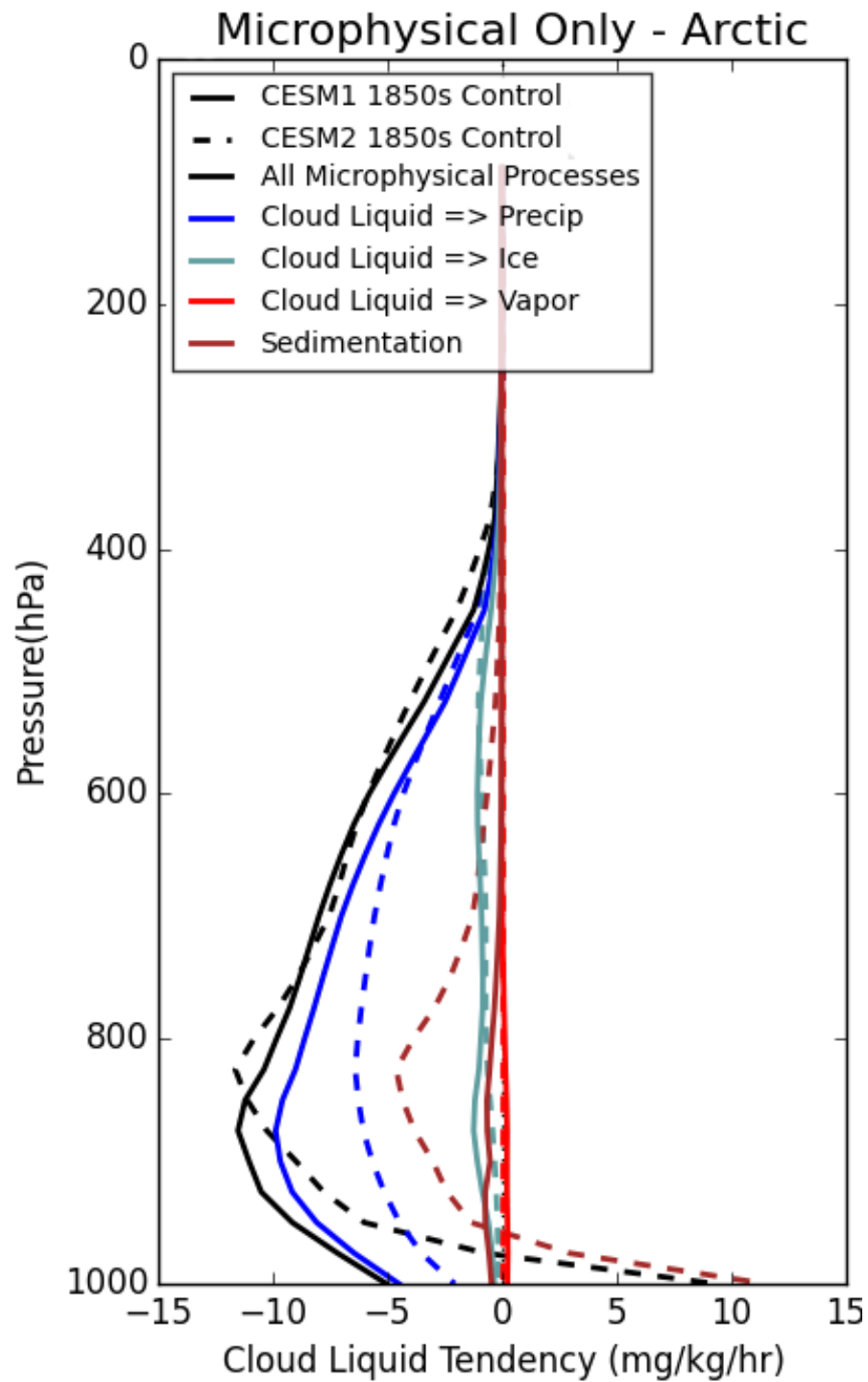


FIGURE 3.9: Vertical profiles of average microphysical tendencies for cloud liquid in the Arctic region (70°N-90°N) for CESM1 (solid lines) and CESM2 (dashed lines) from the 10 year branch simulations of their respective 1850s control runs. The values are averages of the 10 years of monthly averaged output.

TABLE 3.3: Summary of annual mean values for downwelling surface radiation in the Arctic. The \pm value is the standard deviation of the monthly mean values. The top section contains area weighted means for the full modeled Arctic (70-90° N), the center section are global means, and the bottom section contains the area weighted means for the observed Arctic (66.5-82° N)

Dataset	Spatial Region	Time Period	LW↓	SW↓	Total (LW↓+SW↓) (W m ⁻²)	Surface Temp (K)	Near Surface Air Temp (K)
			(W m ⁻²)	(W m ⁻²)			
CESM1	70-90° N	1850s Control	203 ± 45	114 ± 120	317 ± 155	255 ± 12	255 ± 12
CESM2	70-90° N	1850s Control	223 ± 50	92 ± 98	315 ± 134	258 ± 11	258 ± 11
CESM1	Global	1850s Control	-	-	-	287 ± 1	286 ± 1
CESM2	Global	1850s Control	-	-	-	288 ± 1	287 ± 1
CESM1	66.5-82° N	1850s Control	212 ± 45	115 ± 114	327 ± 150	257 ± 13	258 ± 12
CESM2	66.5-82° N	1850s Control	230 ± 48	94 ± 94	324 ± 130	260 ± 11	260 ± 11
Observations	66.5-82° N	2007-10	242 ± 41	91 ± 101	333 ± 133	262 ± 10	262 ± 10

TABLE 3.4: Summary of annual mean values for Arctic precipitation. The \pm value is the standard deviation of the monthly mean values. The top section contains area weighted means for the full modeled Arctic (70-90° N) and the bottom section contains the area weighted means for the observed Arctic (66.5-82° N)

Dataset	Spatial Region	Time Period	LCC Precip Frequency	Total Precip Frequency	Total Precip Rate (mm month ⁻¹)	Snow Rate (mm month ⁻¹)	Rain Rate (mm month ⁻¹)
CESM1	70-90° N	1850s Control	0.66 ± 0.09	0.38 ± 0.06	26 ± 5	20 ± 4	6 ± 6
CESM2	70-90° N	1850s Control	0.65 ± 0.03	0.45 ± 0.10	26 ± 8	17 ± 4	9 ± 8
CESM1	66.5-82° N	1850s Control	0.65 ± 0.08	-	-	-	-
CESM2	66.5-82° N	1850s Control	0.64 ± 0.03	-	-	-	-
Observations	66.5-82° N	2007-10	0.13 ± 0.01	-	-	-	-

Chapter 4

Global Observations of Cloud Impact on Surface Radiation Ratio (CISRR)

4.1 Introduction

The energy balance at the top of Earth's atmosphere (TOA) determines the amount of heat available within the atmosphere, land, and ocean systems. Since the only heat transfer possible at TOA is radiative, the measurements required to constrain the exchange are relatively straightforward. Multiple satellite missions have been focused specifically on measuring the energy exchanged at the TOA (Barkstrom, 1984, Vonder Haar and Suomi, 1971, Wielicki et al., 1996).

Measuring the energy balance at Earth’s surface is more complicated. Not only is there radiative exchange, but latent and sensible heat exchange as well. At present, it is not possible to globally observe all of the exchanges at the surface, and thus precisely constraining the surface energy budget is not yet feasible. For more than a century scientists have leveraged their contemporary datasets to provide estimates of the total energy balance of the atmosphere (e.g. Dines, 1917, L’Ecuyer et al., 2015, Stephens et al., 2012, Trenberth et al., 2009). These estimates vary, but consistently it is radiation, not sensible or latent heat fluxes, that has the largest influence on the energy balance of the surface and will be the focus of this study.

Solar and orbital variations control the amount of radiation incident on the TOA, but it is atmospheric composition, particularly the presence of clouds, that determines how much of that radiation will reach the surface. The Cloud Radiative Effect (CRE) quantifies the impact that clouds have on the radiation received at the surface:

$$CRE_{SFC} = [(F_{allsky}^{\downarrow} - F_{allsky}^{\uparrow}) - (F_{clearsky}^{\downarrow} - F_{clearsky}^{\uparrow})]_{SFC} \quad (4.1)$$

F_{allsky}^{\downarrow} is the downwelling radiative flux in all-sky conditions, meaning cloud effects are taken into account. $F_{clearsky}^{\downarrow}$ is the downwelling radiative flux that would occur in the same scene if clouds were removed.

Bright cloud tops reflect some of the shortwave (SW) radiation that would have otherwise reached the surface, resulting in a cooling CRE (yellow arrows in Fig 4.1). Clouds also

absorb terrestrial longwave (LW) radiation that would otherwise have escaped to space and emit a portion back to the surface, which has a warming CRE (orange arrows in Fig 4.1). The strength of these competing effects is determined by cloud properties, surface conditions, and incident SW.

The $SWCRE_{SFC}$ is largest when a bright cloud is above a dark surface and there is strong solar illumination. Dark surfaces have small albedos (α) in the SW and thus will absorb the majority of incident SW radiation. Bright clouds directly block incoming SW radiation from reaching the surface, so significantly more SW radiation is absorbed in a clear-sky scenario compared to a cloudy one. However, if a surface already has a high α , much of the incident SW is reflected regardless of cloud presence and the $SWCRE_{SFC}$ will be small. Conversely, the $LWCRE_{SFC}$, does not directly depend on surface α , but instead on the increase in atmospheric emissivity resulting from the presence of a cloud. Depending on the characteristics of a particular scene, the overall surface CRE can be cooling, warming, or neutral.

The longterm, passive satellite record can provide reliable estimates of surface downwelling SW and $SWCRE_{SFC}$ (Gupta et al., 1999) because SW is not created in the column, and thus there is a correlation between what's observable at the TOA and surface. However, the surface downwelling LW and $LWCRE_{SFC}$ are dependent on emissions from clouds which are affected by cloud characteristics that cannot be measured with passive satellites, including cloud layering, thickness, and base-height. Thus the surface LW is decoupled from the TOA and requires more knowledge about the full atmospheric

column. Launched in 2006, the active sensors aboard CloudSat and CALIPSO were designed to provide near-global, detailed information about the full column distribution of clouds. Their combined capabilities have allowed for refined estimates of TOA and surface CRE (L’Ecuyer et al., 2019).

To better understand how clouds modulate surface radiation in the Arctic, McIlhattan et al. (2017) developed a diagnostic ratio that clearly shows which of the competing radiative effects is dominant. The Cloud Impact on Surface Radiation Ratio (CISRR) is a ratio of the SWCRE to the LWCRE:

$$CISRR = - \left(\frac{SWCRE}{LWCRE} \right)_{SFC} = - \frac{(F_{sw,allsky}^{\downarrow} - F_{sw,clearsky}^{\downarrow})_{SFC}(1 - \alpha_{SFC})}{(F_{lw,allsky}^{\downarrow} - F_{lw,clearsky}^{\downarrow})_{SFC}} \quad (4.2)$$

When CISRR has a value of 1, that means the $SWCRE_{SFC}$ and $LWCRE_{SFC}$ are balanced; the radiation reaching the surface is equivalent to a clear sky scene and the cloud is neither warming or cooling the surface. When CISRR is > 1 , the $SWCRE_{SFC}$ dominates and the surface receives less radiation than it would in a clear sky scenario. Whereas when CISRR is < 1 , $LWCRE_{SFC}$ is larger and the surface receives more radiation because of the clouds. McIlhattan et al. (2017) demonstrated that the Arctic has a mean annual $CISRR < 1$. This is straightforward to explain: with mainly bright, icy surfaces, the majority of incoming solar energy is already reflected and thus the SWCRE is small in the Arctic summer. In Arctic winter when there is no incoming solar, clouds can only act to warm the surface.

NetCRE_{SFC} is the sum of the SWCRE_{SFC} and the LWCRE_{SFC} and is a useful metric for looking at the total magnitude of the radiation changes due to clouds. However, netCRE results from a combination of cloud frequency and cloud impact. CISRR disentangles these and provides insight into cloud impact by itself, showing what the average cloud that occurs in a particular region does to the surface radiation balance.

In this work we use CISRR to address the following questions:

- How does observed polar cloud behavior alter the surface energy balance?
- Are there regions outside the high latitudes where clouds, on average, warm the surface?
- How well do Global Climate Models (GCMs) reproduce the observed cloud impact on the surface radiation balance?

We show that during the period 2007-2010, the LWCRE dominated over the polar ice sheets ($\text{CISRR} < 1$) while the SWCRE was stronger over the majority of the open ocean ($\text{CISRR} > 1$). We look in detail at CISRR at the top of the Greenland Ice Sheet (GIS), finding that surface observations corroborate what we see from the space-based instruments. There are regions outside of the high latitudes that also see $\text{CISRR} < 1$ in the annual average: the Sahara Desert, the Arabian Peninsula, the Himalayas, and the stratocumulus regions off the south-west coasts of North America, South America, and Africa. We find that one GCM, the Community Earth System Model (CESM), shows promising

agreement to observed CISRR in many regions, but is unable to reproduce the regions of warming outside of the high latitudes.

4.2 Methods and Datasets

To explore the impact of clouds on radiation received at the surface, fluxes derived from NASA A-Train observations are compared to GCM outputs. To corroborate conclusions drawn from the satellite data, we utilize datasets from a suite of ground-based instrumentation at Summit Station, Greenland.

4.3 Datasets

4.3.1 Satellite Observations

To establish the large scale radiative effects of clouds on the Earth’s surface, we utilize the multisensor 2B-FLXHR-lidar product (hereafter 2BFLX). Henderson et al. (2013) created an algorithm that combines the satellite cloud and precipitation property measurements from the CloudSat and CALIPSO satellites with ancillary information including European Centre for Medium-Range Weather Forecasts (ECMWF) temperature and humidity profiles, using them to initialize a radiative transfer model that then provides the vertical profile of observationally constrained fluxes and heating rates (L’Ecuyer et al., 2008, Matus and L’Ecuyer, 2017). 2BFLX and ground-based radiation observations at an ARM site in Darwin, Australia (Protat et al. 2014) and several stations in Greenland (McIlhatten et al., 2017, Van Tricht et al., 2016), have been proven to agree well, particularly

for surface downwelling LW which has been historically difficult to constrain from spaceborne measurements (Gupta et al., 1999).

Details on the CloudSat and CALIPSO satellites, instruments, and orbits can be found in Section 2.2.1. There are two additional products, 2B-CLDCLASS-LIDAR and 2B-GEOPROF, which are plotted in Figs. 4.4 and 4.6 to provide context to the CISRR results. Their descriptions and references can be found in 2.2.1.

Due to the A-Train's orbital path, the full diurnal cycle is not observed in any location. SW radiation is dependent on time of day, so the SW has been normalized so we are not biased to the time of day of the overpass.

4.3.2 Model Data

Output from the Community Earth System Model Large Ensemble (CESM-LE) project Kay et al. (2015) is used in this work to demonstrate how well a state of the art GCM represents CISRR. Details on the CESM-LE were previously presented in Section 3.2.1.1.

4.3.3 Ground-based Observations

To provide an independent assessment of CISRR at a point in the Arctic, we leverage continuous ground-based observations from Summit Station, Greenland. The upper left panel in Fig. 1.2 shows the location of the station as well as the region used for both A-Train and CESM-LE analysis in subsequent comparisons, $70.68\text{-}74.45^\circ\text{N}$, $35.63\text{-}40.63^\circ\text{W}$. The particular dataset used here was developed and detailed in McIlhattan et al. (2017),

utilizing measurements collected as part of the ongoing Integrated Characterization of Energy, Clouds, Atmospheric state and Precipitation at Summit (ICECAPS) project. For specific instrument and dataset details, refer to the methods section in McIlhattan et al. (2017).

Table 4.1 shows that the time periods of the ground-based and satellite observations are different. However, the time measurement periods for both platforms span multiple years and are adjacent, so we expect mismatches in statistics to be small.

4.4 Results

4.4.1 Observed Global CISRR

We begin by presenting the global map of observed annual average CISRR (Fig. 4.2a). The regions of deepest blue are where $SWCRE_{SFC}$ is 10 times stronger than $LWCRE_{SFC}$, and the regions of deepest red are where the $LWCRE_{SFC}$ is 10 times stronger than the $SWCRE_{SFC}$. Where CISRR is > 1 (blue), the average cloud effect on the surface is cooling, and where CISRR is < 1 (red), the average cloud effect on the surface is warming. Figure 4.2a shows that for the majority of the planet, clouds act to cool the surface, with particularly strong cooling in the tropics. It is logical that the $SWCRE_{SFC}$ dominates over the tropical oceans and rainforests – bright clouds over the dark water or tree canopy severely restrict the amount of SW absorbed by the surface, while the cloud impact on the LW is not as drastic due to the already warm, humid air. The regions where clouds most strongly warm the surface are the Antarctic and Greenland ice sheets. With bright

snow and ice covered surfaces, much of the incoming solar SW is reflected regardless of the presence of a cloud. Thus, the $LWCRE_{SFC}$ has a larger influence on the surface in the summer months and is the only influence in winter when there is no incoming SW. Cloud warming over the GIS is further examined in Section 4.4.3.

Outside of the ice sheets, Fig. 4.2a highlights five additional regions where clouds have an average warming effect: (1) sea ice; (2) the glacier covered Himalayas; (3) the far northern edges of North America and Asia; (4) the deserts of North Africa and the Arabian Peninsula; and (5) the stratocumulus regions off the south-west coasts of North America, South America, and Africa. The $CISRR < 1$ values of regions 1-3 can be explained by the same logic as the ice sheets; their predominantly bright, icy surfaces reflect most sunlight regardless of cloud cover so the $SWCRE_{SFC}$ will always be small. The other regions of warming we see are harder to explain. The deserts of North Africa and the Arabian Peninsula are the least cloudy regions on Earth, and the few clouds that do occur are most often high thin cirrus (L'Ecuyer et al., 2019). Cirrus clouds are effective insulators of terrestrial LW, however they are ineffective at blocking incoming SW. The authors suggest that the low $CISRR$ values are a result of a relatively strong α of sand (25-40 %, (Petty, 2006)) and the cloud type. This is a case where the net surface CRE would not show strong warming because clouds are so infrequent. Perhaps the most puzzling region of $CISRR < 1$ is (5), the stratocumulus regions off the south-west coasts of North America, South America, and Africa. Oceans have very low α (< 10 %, (Petty, 2006)), and it would seem that any cloud overlying such a surface would have a cooling

effect, however it is clear that that is not the case. The stratocumulus region off the south-west coast of Africa is examined in detail in Section 4.4.4.

4.4.2 GCM Comparison

Figure 4.2b. shows the CESM-LE representation of CISRR. A casual comparison of Figs. 4.2a and 4.2b demonstrates that the model captures the gross features of the observed CISRR: the lowest values are over the ice sheets and the highest values are over the tropics, with clouds over the oceans in general showing an average cooling effect. However, the model does not show observed warming outside of the polar regions, save one or two grid boxes in the western Himalayas and a small portion of north central Siberia. Noticeably absent from the model is the cloud warming of the stratocumulus cloud decks and Northern Africa.

Since CISRR is a ratio, taking the difference between the observed and modeled values would not be meaningful. Instead we have divided the modeled values by the observed values, giving the fractional difference shown in Fig. 4.2c.). The regions in red show where the model clouds have too large a warming effect and the regions in blue are where the model clouds have too large a cooling effect relative to observed values. The $LWCRE_{SFC}$ (cloud warming) is too large at the poles, equatorial rainforests, and throughout the tropical oceans, meaning the model clouds are not bright enough - not reflecting enough SW back to space relative to the amount of LW they trap. Conversely, the model $SWCRE_{SFC}$ (cloud cooling) is too large over most land regions, particularly the deserts, implying that the model clouds are too opaque relative to the observed clouds.

The annual cycle of the near-global (82° S - 82° N) mean CISRR is shown in Fig. 4.3. All line plots in this work follow the same format: the heavy blue line represents the average of all observational years, each blue circle depicting a single year's monthly average; the heavy red line represents the average of all ensemble members, each red x depicting a single member's four year monthly average; the shaded regions are the standard deviation about the mean for each dataset. On average, the monthly global value for CISRR in both observations and models hovers slightly over 2, year-round. This means that the SWCRE_{SFC} is consistently twice as strong as LWCRE_{SFC} , and the model captures that value well. However, there is greater variability in the observations, seen in the larger shaded region about the mean. Despite this variation, both in the model and the real world, on average clouds tend to decrease the radiation received by the surface. Regionally and temporally, however, there is large variation in CISRR. In the following sections, we explore two regions that see annual mean CISRR < 1 .

4.4.3 A Closer Look at the Greenland Ice Sheet

To illustrate how important surface characteristics are to CISRR, we look at an individual overpass of the GIS by CloudSat and Calipso made on September 12, 2009. The line on the map in Fig. 4.4(a) shows the location of the swath plotted in Fig. 4.4(b). The swath begins over the open ocean off the southeastern coastline of Greenland, then moves northwest up and onto the GIS. The y-axis in Fig. 4.4(a) is both latitude and time; moving forward in time is also moving north and west for the satellite swath. The reflectivity swath from CloudSat is displayed at the top of Fig. 4.4(b) and depicts

a spatially large and complex cloud structure. For each individual satellite footprint contained in the swath, CISRR was calculated (Fig. 4.4**(b)**, center). It is clear that for the first half of the swath, CISRR is $\gg 1$ and for the second half it is < 1 . The cloud characteristics (Fig. 4.4**(b)**, bottom) do not change markedly before and after CISRR switches from cooling to warming; instead, the change occurs when the satellites move from the low α ocean to the high α ice sheet. This can be clearly seen in the map of Fig. 4.4**(a)**, which is colored based on the corresponding CISRR value — all ocean footprints are CISRR $\gg 1$ and all GIS footprints are CISRR < 1 . Since the cloud field is similar off and on the coast, the LWCRE_{SWFC} is likely similar as well. The SWCRE_{SWFC} on the other hand is much reduced over the GIS relative to the ocean, because the GIS reflects most sunlight regardless of cloud presence.

The data collected at Summit Station (Fig. 4.4**(a)**, marked with a star) by the ICECAPS project allows for a statistical comparison of CISRR calculated from ground-based data to the satellite and model estimates. Fig 4.4**(c)** compares the ground-based values (black line with grey shading) to mean satellite and model values from the red box drawn in Fig. 4.4**(a)**. For all three datasets, the LWCRE_{SWFC} is at least twice as strong as the SWCRE_{SWFC}. This is true even in the summer months, when there is 24-hour solar illumination. Individual clouds may have an overall cooling effect, but the observations clearly show that the average cloud impact on the GIS surface near Summit Station is warming. Interestingly, the CESM-LE results follow the satellite values very closely, with nearly all model values within the annual variability of the observations. This is surprising, given CESM-LE's known difficulties with representing Arctic cloud liquid

(Cesana et al., 2015, Kay et al., 2016a, McIlhattan et al., 2017, Tan and Storelvmo, 2016), resulting in radiation and temperature biases at the Arctic surface (Barton et al., 2014, Cesana et al., 2015, English et al., 2014, Forbes and Ahlgrimm, 2014, Kay et al., 2016a, McIlhattan et al., 2017). While the model captures the warming character of the cloud effect near Summit Station (demonstrated by CISRR), netCRE_{SFC} (Fig. 4.5) shows that model clouds in CESM-LE do not input enough energy relative to surface/satellite observations, meaning that compensating errors have resulted in a close match for CISRR.

4.4.4 A Closer Look at the Stratocumulus off the Coast of Africa

Over the ocean, it's surprising that CISRR is ever less than one because the relatively dark, low α surface absorbs much of the sunlight incident on it, and thus overlying clouds in general have a very large SWCRE_{SFC} . This is illustrated by the generally high CISRR values over the majority of the oceans in Fig. 4.2(a). However the stratocumulus regions off the south-west coasts of North America, South America, and Africa do not follow that pattern. In Fig. 4.6 we take a closer look at the region off of the south-west coast of Africa.

First we take an individual overpass in the region, shown by the line in Fig. 4.6a. The clouds in this July 6, 2009 scene are within ~ 1 km of the ocean surface, which puts them within CloudSat's blind zone (discussed in Section 2.2.1), and CALIPSO's LIDAR information is presented in place of CPR data in Fig. 4.6b. As in the Greenland example,

the satellites were moving from south to north and the LIDAR backscatter shows the clouds becoming geometrically thinner, less contiguous, and closer to the surface towards the north end of the swath. CISRR also goes from mostly slightly above 1 (cooling) to mostly, slightly below 1 (warming) over the course of the swath though there are individual footprints both above and below throughout (Fig. 4.6b, center). Since the surface remains open ocean for the full swath, and the cloud phase remains liquid (Fig. 4.6b, bottom), it appears that the cloud character changes are enough to cause the balance of CRE to favor the $LWCRE_{SFC}$.

The annual cycle of CISRR for this region is shown in Fig. 4.6c, and comes from averaged observations within the red box drawn in Fig. 4.6a. Observations show that clouds are primarily warming the surface during most months, though in late southern hemisphere spring (October and November) clouds have a mean cooling effect with the largest year-to-year variability (blue shaded region). CESM-LE, on the other hand, shows the average cloud effect to be cooling, with very little year-to-year variability.

How reasonable is this observed CISRR? Can clouds increase surface radiation over the ocean? The author acknowledges that it is hard to explain, and that the 2BFLXHR is a retrieval based on satellite data, with a variety of assumptions inherent in the algorithm that creates it. It is possible that there is a bias in the algorithm. However, initial results from reanalysis data (not shown), also show mean CISRR < 1 in the stratocumulus regions that we see in observations. Our initial theory is that the low clouds are coming off of the warm continents, and when the warm air-masses overlies regions of ocean waters

cooled by coastal upwelling, the difference in LW emission provided by the warm, low clouds is enough to tip the balance.

While there are no ground- or ship-based observations in this region that can definitively show that CISRR is < 1 , the recently completed NASA ORACLES (ObseRvations of Aerosols above CLouds and their intEractionS) campaign collected cloud and radiation observations in this region that could be used in the future to calculate CISRR.

4.5 Conclusions

Active, space-based sensors were leveraged to provide a global picture of the Cloud Impact on Surface Radiation Ratio (CISRR). CISRR is unique in that it provides a measure of how individual clouds impact the radiation seen at the surface. Distinct from netCRE, CISRR does not rely on the frequency of clouds that occur in a region, instead only looking at the relative influence of the $SWCRE_{SFC}$ and $LWCRE_{SFC}$.

Over most of the planet, clouds act to reduce the radiation received by the surface, with the strongest cooling over the tropical oceans and equatorial forests. Over the Earth's three major ice sheets, in the annual mean CISRR shows that the $LWCRE_{SFC}$ dominates the $SWCRE_{SFC}$. This warming effect of polar clouds is due to the bright, icy surfaces reflecting most incoming sunlight, regardless of cloud presence, leading to a consistently small $SWCRE_{SFC}$. Surface observations of clouds and radiation confirm the satellite-based CISRR values at Summit Station, Greenland. A few regions outside the poles also show clouds warming the surface in the annual mean, including the Sahara Desert,

the Arabian Peninsula, the Himalayas, and the stratocumulus regions off the south-west coasts of North America, South America, and Africa.

The observed CISRR values provide a useful benchmark for GCMs. Clouds are necessarily parameterized in GCMs (discussed at length in Chapter 3), so achieving the correct radiation balance at the surface is difficult. CESM-LE shows promising agreement with the observed values in the general character of CISRR. However, the model has difficulty reproducing the warming regions seen outside of the poles.

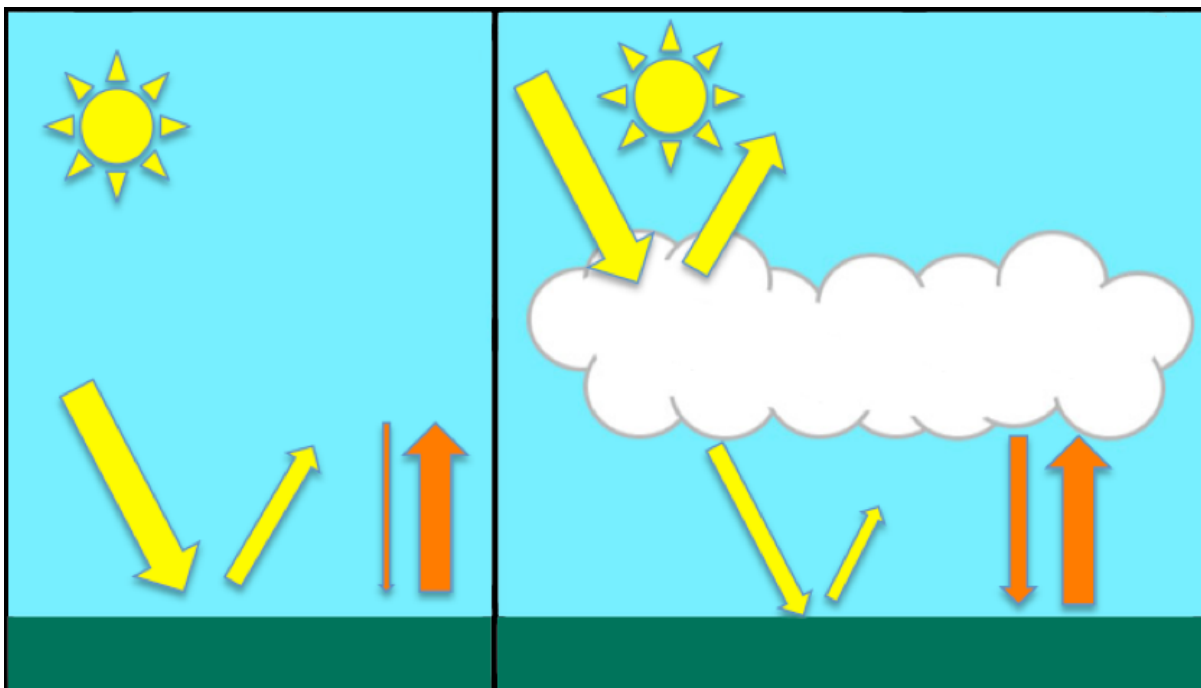


FIGURE 4.1: A simplified cartoon of the broadband radiative effects of a cloud on energy received at the surface; SW is depicted in yellow arrows, LW in orange. In a cloudless sky (left), incoming solar SW radiation reaches the surface unobstructed, with some reflected back to space depending on the surface albedo. Outgoing terrestrial radiation emits towards space, with only a small amount of downwelling LW radiation (DLR) being emitted towards the surface by the low emissivity atmosphere. When a cloud is introduced (right), incoming SW is reflected by the cloud, reducing the amount reaching the surface. The increased emissivity of the cloud relative to clear sky also acts to increase the amount of DLR reaching the surface.

TABLE 4.1: Summary of the time periods for the datasets used in Chapter 2. Details on the datasets and time periods can be found in McIlhattan et al. (2017).

Dataset	Time Period Used	Months Excluded
<i>A-Train Observations (2BFLXR)</i>	Jan 2007 – Dec 2010	Sep 2008, Dec 2009
<i>Summit Station Observations</i>	Jan 2011 – Oct 2013	None
<i>CESM-LE Output</i>	Jan 2007 – Dec 2010	None

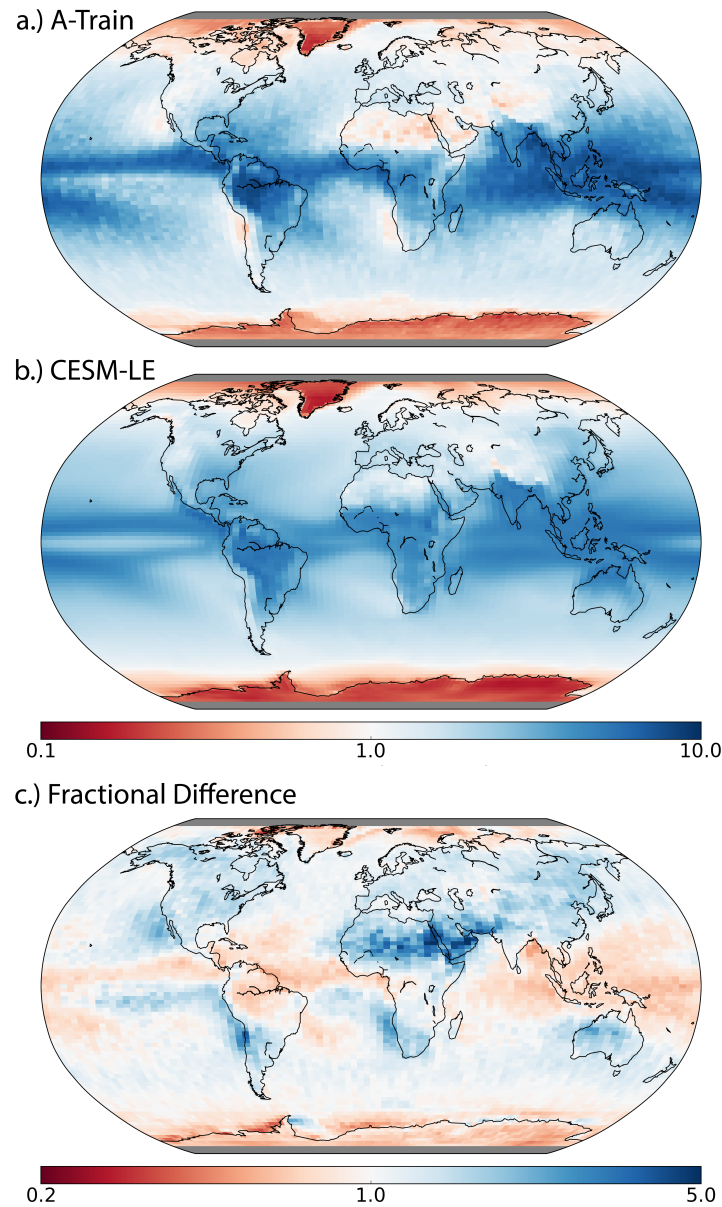


FIGURE 4.2: **(a)** Annual average of the observed Cloud Impact on Surface Radiation Ratio (CISRR). CISRR is the ratio of shortwave cloud radiative effect (SWCRE) to the longwave cloud radiative effect (LWCRE). Observations are from the A-Train data product 2B-FLXHR-Lidar between January 2007 and December 2010. Regions in blue indicate the SWCRE is dominant and the clouds have an average cooling effect on the surface. Regions in red indicate the LWCRE is dominant and the clouds have an average warming effect on the surface. Regions in white indicate the SWCRE and LWCRE are balanced. Regions outside of the A-Train orbit are filled in gray. **(b)** Annual average CISRR for CESM-LE for the same time period. **(c)** The fractional difference between the top and middle figures. Regions in red indicate CESM-LE has too strong of cloud warming relative to observations, regions in blue show too strong cooling. Note: panel (a) is adapted from McIlhattan et al. (2017) Figure 2.

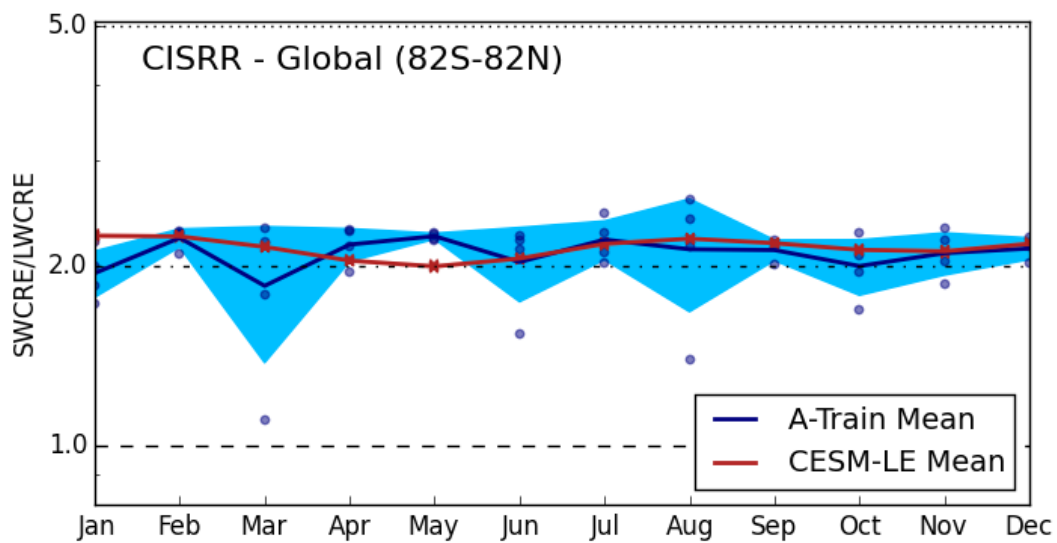


FIGURE 4.3: Annual cycle of CISRR for the near-global satellite observational range, 82° S- 82° N. Satellite observations are in blue, CESM-LE outputs are in red. The heavy blue line represents the average of all observational years, each blue circle depicting a single year's monthly average. The heavy red line represents the average of all ensemble members, each red x depicting a single member's four year monthly average. The shaded regions are the standard deviation about the mean for each dataset

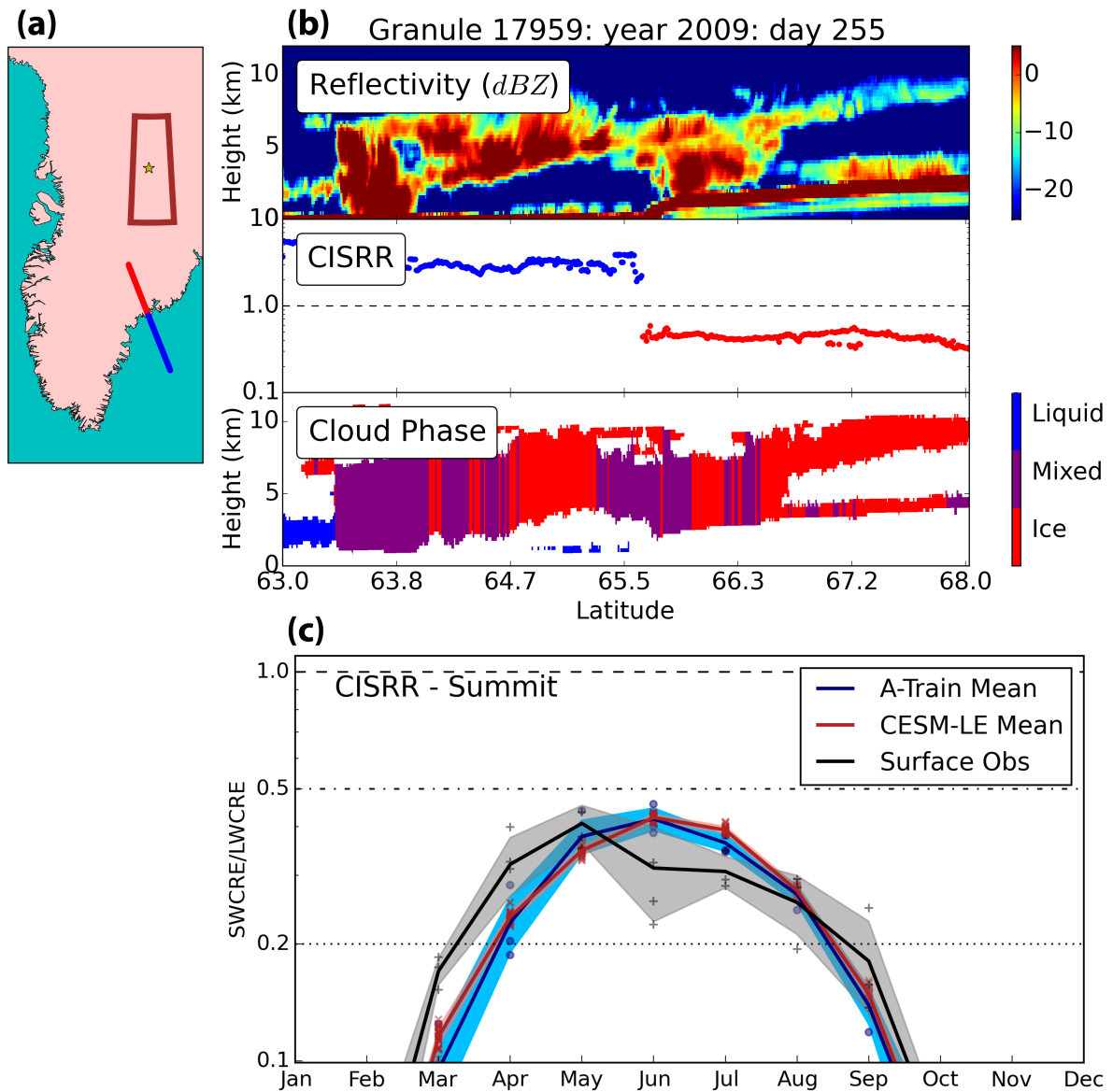


FIGURE 4.4: (a) Map of Greenland with a box showing the region used for the area weighted line plot, a line depicting the A-Train swath path, and a star at Summit Station. (b) A-Train overpass of SE Greenland depicting vertical curtains of reflectivity, CISRR, and cloud phase. (c) Annual cycle of CISRR over Summit Station, Greenland. Satellite observations are in blue, CESM-LE outputs are in red, surface observations are in black/grey. The region used for satellite/model analysis is grid boxes within 70-75° N and 35-41° W.

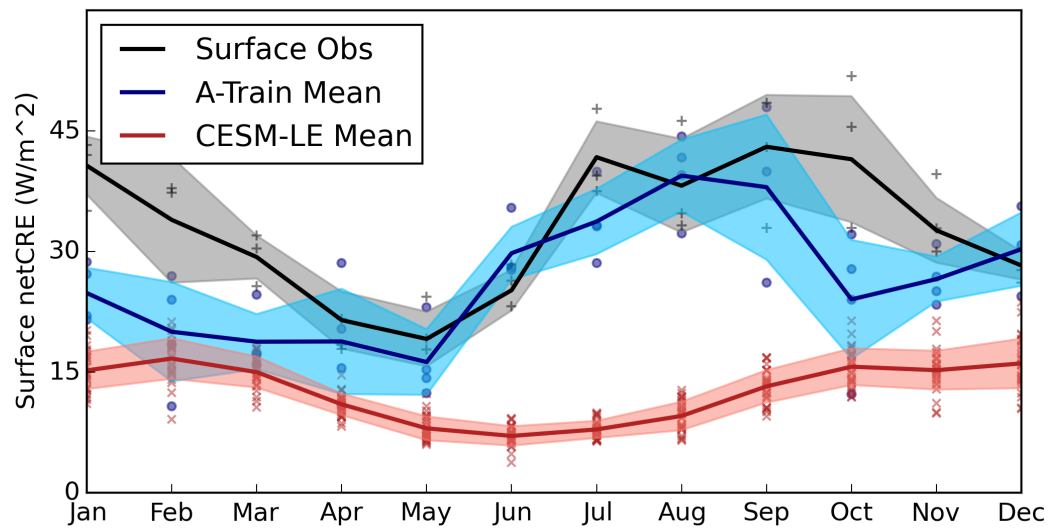


FIGURE 4.5: As in Fig 4.4(c) for surface net cloud radiative effect (NETCRE).

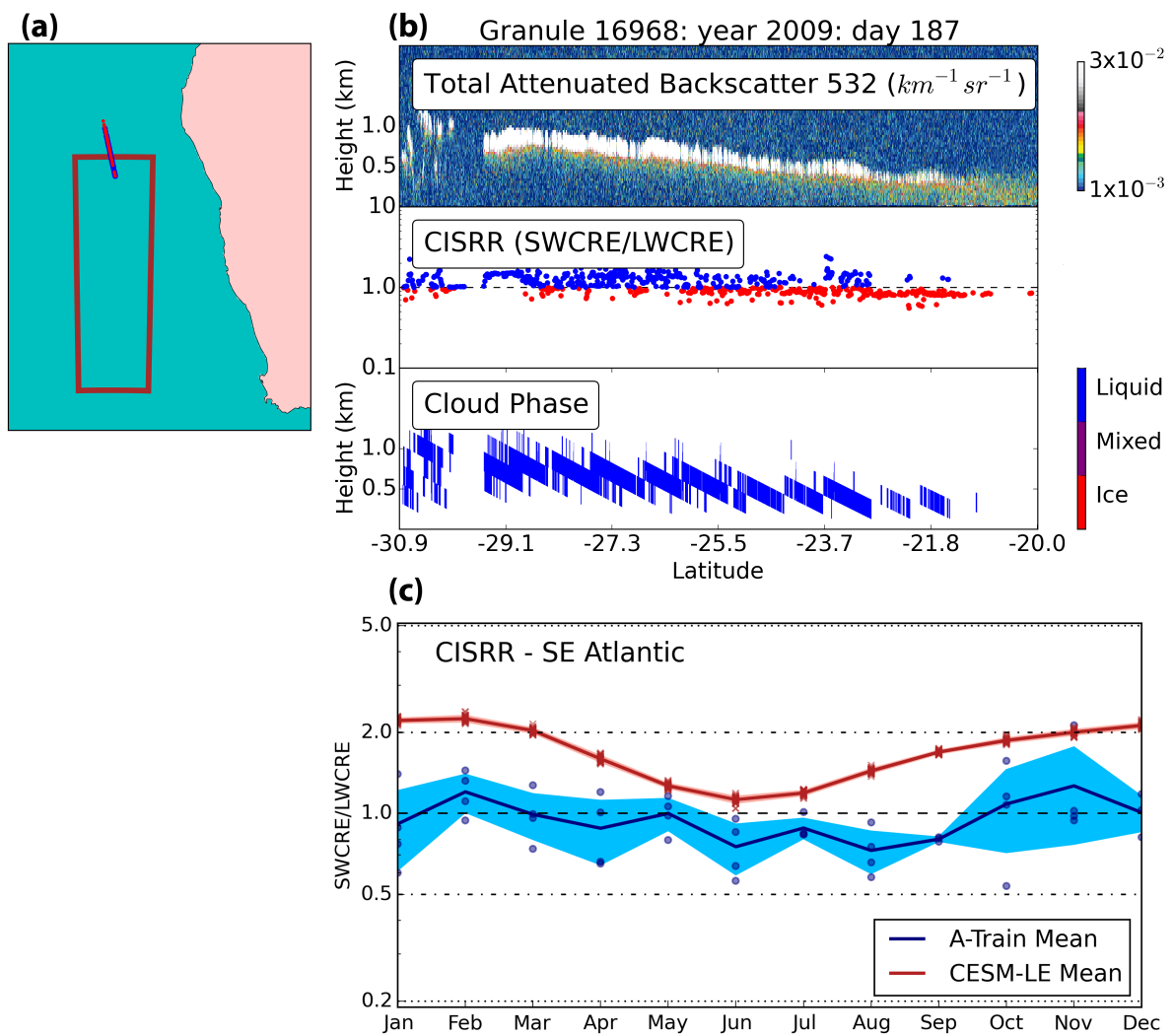


FIGURE 4.6: As in Fig 4.4 with CALIPSO lidar backscatter instead of radar reflectance in (a). The region used for satellite/model analysis in (c) is 34-20° S, 5-10° E.

Chapter 5

Synthesis

5.1 Summary of Results

Arctic clouds play an important role in the surface energy balance through modulating SW and LW radiation and water budgets of the Arctic. Clouds also play an important role in building the Arctic sea ice and land ice through precipitation. Observations from NASA's A-Train satellites give us a new and detailed view into polar clouds that was not possible with passive sensors. By leveraging these measurements, we have: documented the importance of cloud phase in precipitation events over the GIS (Chapter 2); provided context to changes in Arctic cloud representation in the Community Earth System Model (CESM) (Chapter 3); and mapped the observed Cloud Impact on Surface Radiation Ratio (CISRR), showing that in the Arctic, the warming effect of clouds far outweighs their cooling effect (Chapter 4).

Precipitation over the GIS is dominated by fully-glaciated ice cloud events (IC). IC snowfall events are overall more frequent and have higher snowfall rates than those associated with Arctic mixed-phase cloud events (CLW), making up $\sim 70\%$ of the total snowfall observations and producing $\sim 80\%$ of the total annual accumulation. However, during the summer when the solar insolation is at its peak, the CLW events are nearly as frequent ($\sim 45\%$ of events) as IC, and are thus important for brightening the GIS surface. The clouds associated with the two precipitation regimes are distinct beyond their phase — IC clouds are consistently geometrically deeper with larger integrated reflectivity values than CLW clouds. IC events are associated with various cyclone locations and CLW events occur under anomalously high pressure scenarios. The detectability of precipitation events from space is also distinct for the two regimes: while $\sim 95\%$ of IC snowfall events are likely detected by CloudSat's CPR, that percentage drops to $\sim 75\%$ for CLW snowfall.

The mean state Arctic clouds simulated in CESM2 have changed greatly from those simulated in CESM1. The frequency of Arctic LCCs has increased from $\sim 17\%$ in CESM1 to $\sim 50\%$ in CESM2, with total cloud liquid increasing by a factor of six. Using A-Train observations to show the reasonableness of LCC frequency, we find that CESM2 might now be simulating too many LCCs in summer. While the total precipitation amount produced by clouds remained the same going from version 1 to version 2, the distribution between phases changed, with CESM2 having more rain and less snow, relative to CESM1. The increase in rain is primarily a result of increased sedimentation of supercooled cloud liquid out of the bottom level of the modeled atmosphere in CESM2. The changes in

clouds and precipitation resulted in important mean state changes to the Arctic surface. CESM2 has a warmer Arctic — the annual average surface temperature is 3 K warmer in CESM2, and the winter average (November through January) is 5 K warmer. The mean state snowpack is also markedly changed, with CESM2 having less than half the snowpack on sea ice of CESM1 and CESM2 having more than eight times the snowpack on land simulated by CESM1.

CISRR is a metric that shows whether the SW (cooling) cloud radiative effect (CRE) or the LWCRE (warming) is dominant in a particular region. Globally, the cooling effect of clouds is twice as strong as their warming effect. However, CISRR clearly shows that on average the LWCRE dominates over the icy Arctic surfaces and overall clouds have a warming effect in that region. A-Train data, surface-based Summit Station data, and CESM1 model data all agree: while individual clouds may cool the Arctic surface, they are vastly outnumbered by clouds that warm. Even in the height of summer, with 24-hour incoming solar insolation, Arctic clouds still have CISRR < 0.5 , meaning their warming effect is twice as strong as their cooling effect.

Overall, the results presented in this dissertation highlight the key role that Arctic clouds play in regulating the radiation and moisture received by the Arctic surface. Observations from CloudSat and CALIPSO have been transformational in our community's understanding of the distribution and characteristics of Arctic clouds. These large-scale, detailed datasets provide key benchmarks for model simulations. As the Arctic continues to warm, model predictions of sea-level rise, melting permafrost, and sea ice retreat will

all be essential tools for governments and communities in planning and preparing for longer term climate changes. As models become better at reproducing the present-day Arctic clouds and climate seen in real-world observations, our confidence in the model physics, parameterizations, and future predictions will increase.

Bibliography

Alley, R. B., D. A. Meese, C. A. Shuman, A. J. Gow, K. C. Taylor, P. M. Grootes, J. W. C. White, M. Ram, E. D. Waddington, P. A. Mayewski, and G. A. Zielinski, 1993: Abrupt increase in greenland snow accumulation at the end of the younger dryas event. *Nature*, **362**, 527–529, doi:10.1038/362527a0.

Arrhenius, S., 1896: On the influence of carbonic acid in the air upon the temperature of the ground. *Philos. Mag. J. Sci.*, **5**, 237–276.

Barkstrom, B. R., 1984: The earth radiation budget experiment (erbe). *Bulletin of the American Meteorological Society*, **65**, 1170–1185, doi:10.1175/1520-0477(1984)065<1170:TERBE>2.0.CO;2.

URL [https://doi.org/10.1175/1520-0477\(1984\)065<1170:TERBE>2.0.CO;2](https://doi.org/10.1175/1520-0477(1984)065<1170:TERBE>2.0.CO;2)

Barton, N. P., S. A. Klein, and J. S. Boyle, 2014: On the contribution of longwave radiation to global climate model biases in arctic lower tropospheric stability. *Journal of Climate*, **27**, 7250–7269, doi:10.1175/JCLI-D-14-00126.1.

URL <https://doi.org/10.1175/JCLI-D-14-00126.1>

- Battaglia, A. and J. Delanoë, 2013: Synergies and complementarities of cloudsat-calipso snow observations. *Journal of Geophysical Research Atmospheres*, **118**, 721–731, doi:10.1029/2012JD018092.
- Bennartz, R., F. Fell, C. Pettersen, M. D. Shupe, and D. Schuettmeyer, 2019: Spatial and temporal variability of snowfall over greenland from cloudsat observations. *Atmospheric Chemistry and Physics Discussions*, **2019**, 1–32, doi:10.5194/acp-2018-1045.
URL <https://www.atmos-chem-phys-discuss.net/acp-2018-1045/>
- Bennartz, R., M. D. Shupe, D. D. Turner, V. P. Walden, K. Steffen, C. J. Cox, M. S. Kulie, N. B. Miller, and C. Pettersen, 2013: July 2012 Greenland melt extent enhanced by low-level liquid clouds. *Nature*, **496**, 83–6, doi:10.1038/nature12002.
- Berdahl, M., A. Rennermalm, A. Hammann, J. Mioduszewski, S. Hameed, M. Tedesco, J. Stroeve, T. Mote, T. Koyama, and J. R. McConnell, 2018: Southeast greenland winter precipitation strongly linked to the icelandic low position. *Journal of Climate*, **31**, 4483–4500, doi:10.1175/JCLI-D-17-0622.1.
- Box, J. E., X. Fettweis, J. C. Stroeve, M. Tedesco, D. K. Hall, and K. Steffen, 2012: Greenland ice sheet albedo feedback: Thermodynamics and atmospheric drivers. *Cryosphere*, **6**, 821–839, doi:10.5194/tc-6-821-2012.
- Bring, A., I. Fedorova, Y. Dibike, L. Hinzman, J. Mård, S. H. Mernild, T. Prowse, O. Semenova, S. L. Stuefer, and M.-K. Woo, 2016: Arctic terrestrial hydrology: A synthesis of processes, regional effects, and research challenges. *Journal of Geophysical Research: Biogeosciences*, **121**, 621–649, doi:10.1002/2015JG003131.

URL <https://agupubs.onlinelibrary.wiley.com/doi/abs/10.1002/2015JG003131>

Budyko, M. I., 1969: The effect of solar radiation variations on the climate of the earth. *Tellus*, **21**, 611–619, doi:10.3402/tellusa.v21i5.10109.

URL <https://doi.org/10.3402/tellusa.v21i5.10109>

C3S, 2017: Era5: Fifth generation of ecmwf atmospheric reanalyses of the global climate. *Copernicus Climate Change Service Climate Data Store (CDS)*, **date of access = July 2019**.

Castellani, B. B., M. D. Shupe, D. R. Hudak, and B. E. Sheppard, 2015: The annual cycle of snowfall at summit, greenland. *Journal of Geophysical Research: Atmospheres*, **120**, 6654–6668, doi:10.1002/2015JD023072.

URL <https://agupubs.onlinelibrary.wiley.com/doi/abs/10.1002/2015JD023072>

Cesana, G., J. E. Kay, H. Chepfer, J. M. English, and G. De Boer, 2012: Ubiquitous low-level liquid-containing Arctic clouds: New observations and climate model constraints from CALIPSO-GOCCP. *Geophysical Research Letters*, **39**, 1–6, doi:10.1029/2012GL053385.

Cesana, G., D. E. Waliser, X. Jiang, and J. L. F. Li, 2015: Multimodel evaluation of cloud phase transition using satellite and reanalysis data. *Journal of Geophysical Research D: Atmospheres*, **120**, 7871–7892, doi:10.1002/2014JD022932.

Chen, Q.-s., D. H. Bromwich, and L. Bai, 1997: Precipitation over greenland retrieved by a dynamic method and its relation to cyclonic activity. *Journal of Climate*, **10**, 839–870, doi:10.1175/1520-0442(1997)010<0839:POGRBA>2.0.CO;2.

Chepfer, H., S. Bony, D. Winker, G. Cesana, J. L. Dufresne, P. Minnis, C. J. Stubenrauch, and S. Zeng, 2010: The gcm-oriented calipso cloud product (calipso-goccp). *Journal of Geophysical Research: Atmospheres*, **115**, doi:10.1029/2009JD012251.

URL <https://agupubs.onlinelibrary.wiley.com/doi/abs/10.1029/2009JD012251>

Church, J. A., J. M. Gregory, P. Huybrechts, M. Kuhn, K. Lambeck, M. Nhuan, D. Qin, and P. L. Woodworth, 2001: *Climate Change 2001: The Scientific Basis*, Cambridge University Press, chapter 11. 639–693.

Clark, P. U., J. D. Shakun, S. A. Marcott, A. C. Mix, M. Eby, S. Kulp, A. Levermann, G. A. Milne, P. L. Pfister, B. D. Santer, D. P. Schrag, S. Solomon, T. F. Stocker, B. H. Strauss, A. J. Weaver, R. Winkelmann, D. Archer, E. Bard, A. Goldner, K. Lambeck, R. T. Pierrehumbert, and G.-K. Plattner, 2016: Consequences of twenty-first-century policy for multi-millennial climate and sea-level change. *Nature Climate Change*, **6**, 360–369, doi:10.1038/nclimate2923.

Cullather, R. I., S. M. J. Nowicki, B. Zhao, and M. J. Suarez, 2014: Evaluation of the surface representation of the greenland ice sheet in a general circulation model. *Journal of Climate*, **27**, 4835–4856, doi:10.1175/JCLI-D-13-00635.1.

Dai, A., 2006: Precipitation characteristics in eighteen coupled climate models. *Journal of Climate*, **19**, 4605–4630, doi:10.1175/JCLI3884.1.

URL <https://doi.org/10.1175/JCLI3884.1>

Danabasoglu, G., 2019: The community earth system model version 2 (cesm2). *JAMES*, **(submitted)**.

Dines, W. H., 1917: The heat balance of the atmosphere. *F. R. Met. Soc.*.

DuVivier, A. K., M. M. Holland, S. Tilmes, A. Gettelman, D. Bailey, and J. E. Kay, 2019: Impact of cloud physics on the greenland ice sheet surface climate: a study with the community atmosphere model. *Journal of Geophysical Research: Atmospheres*, **submitted**.

Enderlin, E. M., I. M. Howat, S. Jeong, M.-J. Noh, J. H. van Angelen, and M. R. van den Broeke, 2014: An improved mass budget for the Greenland ice sheet. *Geophysical Research Letters*, **41**, 866–872, doi:10.1002/2013GL059010.

URL <http://doi.wiley.com/10.1002/2013GL059010>

English, J. M., J. E. Kay, A. Gettelman, X. Liu, Y. Wang, Y. Zhang, and H. Chepfer, 2014: Contributions of clouds, surface albedos, and mixed-phase ice nucleation schemes to arctic radiation biases in cam5. *Journal of Climate*, **27**, 5174–5197, doi:10.1175/JCLI-D-13-00608.1.

URL <https://doi.org/10.1175/JCLI-D-13-00608.1>

Ettema, J., M. R. van den Broeke, E. van Meijgaard, W. J. van de Berg, J. L. Bamber, J. E. Box, and R. C. Bales, 2009: Higher surface mass balance of the greenland ice sheet revealed by high-resolution climate modeling. *Geophysical Research Letters*, **36**, doi:10.1029/2009GL038110.

URL <https://agupubs.onlinelibrary.wiley.com/doi/abs/10.1029/2009GL038110>

Forbes, R. M. and M. Ahlgrim, 2014: On the representation of high-latitude boundary layer mixed-phase cloud in the ECMWF global model. *Monthly Weather Review*, 3425–3446, doi:10.1175/MWR-D-13-00325.1.

Francis, J. A., E. Hunter, J. R. Key, and X. Wang, 2005: Clues to variability in Arctic minimum sea ice extent. *Geophysical Research Letters*, **32**, 1–4, doi:10.1029/2005GL024376.

Frei, A., M. Tedesco, S. Lee, J. Foster, D. K. Hall, R. Kelly, and D. A. Robinson, 2012: A review of global satellite-derived snow products. *Advances in Space Research*, **50**, 1007 – 1029, doi:<https://doi.org/10.1016/j.asr.2011.12.021>.

URL <http://www.sciencedirect.com/science/article/pii/S0273117711008611>

Gettelman, A., C. Hannay, J. T. Bacmeister, R. B. Neale, A. G. Pendergrass, G. Danabasoglu, J.-F. Lamarque, J. T. Fasullo, D. A. Bailey, D. M. Lawrence, and M. J. Mills, 2019: High climate sensitivity in the community earth system model version 2 (cesm2). *Geophysical Research Letters*, **46**, 8329–8337, doi:10.1029/2019GL083978.

URL <https://agupubs.onlinelibrary.wiley.com/doi/abs/10.1029/2019GL083978>

Gupta, S., N. Ritchey, A. Wilber, C. Whitlock, G. Gibson, and P. Stackhouse, 1999: A climatology of surface radiation budget derived from satellite data. *Journal of Climate*, **12**, 2691–2710, doi:10.1175/1520-0442(1999)012<2691:ACOSRBj2.0.CO;2.

Hakuba, M. Z., D. Folini, M. Wild, and C. Schär, 2012: Impact of greenland's topographic height on precipitation and snow accumulation in idealized simulations. *Journal of Geophysical Research: Atmospheres*, **117**, doi:10.1029/2011JD017052.

URL <https://agupubs.onlinelibrary.wiley.com/doi/abs/10.1029/2011JD017052>

Hanna, E., T. E. Cropper, R. J. Hall, and J. Cappelen, 2016: Greenland blocking index 1851-2015: a regional climate change signal. *International Journal of Climatology*, **36**, 4847–4861, doi:10.1002/joc.4673.

URL <https://rmets.onlinelibrary.wiley.com/doi/abs/10.1002/joc.4673>

Hanna, E., F. J. Navarro, F. Pattyn, C. M. Domingues, X. Fettweis, E. R. Ivins, R. J. Nicholls, C. Ritz, B. Smith, S. Tulaczyk, P. L. Whitehouse, and H. J. Zwally, 2013: Ice-sheet mass balance and climate change. *Nature*, **498**, 51–59, doi:10.1038/nature12238.

Henderson, D. S., T. L'Ecuyer, G. Stephens, P. Partain, and M. Sekiguchi, 2013: A multisensor perspective on the radiative impacts of clouds and aerosols. *Journal of Applied Meteorology and Climatology*, **52**, 853–871, doi:10.1175/JAMC-D-12-025.1.

- Jakobson, E. and T. Vihma, 2010: Atmospheric moisture budget in the arctic based on the era-40 reanalysis. *International Journal of Climatology*, **30**, 2175–2194, doi:10.1002/joc.2039.
- Kapsner, W. R., R. B. Alley, C. A. Shuman, S. Anandakrishnan, and P. M. Grootes, 1995: Dominant influence of atmospheric circulation on snow accumulation in greenland over the past 18,000 years. *Nature*, **373**, 52–54, doi:10.1038/373052a0.
- Kay, J. E., L. Bourdages, N. Miller, A. Morrison, V. Yettella, H. Chepfer, and B. Eaton, 2016a: Evaluating and improving cloud phase in the community atmosphere model version 5 using spaceborne lidar observations. *Journal of Geophysical Research: Atmospheres*, doi:10.1002/2015JD024699, 2015JD024699.
- Kay, J. E., C. Deser, A. Phillips, A. Mai, C. Hannay, G. Strand, J. Arblaster, S. Bates, G. Danabasoglu, J. Edwards, M. Holland, P. Kushner, J.-F. Lamarque, D. Lawrence, K. Lindsay, A. Middleton, E. Munoz, R. Neale, K. Oleson, L. Polvani, and M. Vertenstein, 2015: The Community Earth System Model (CESM) Large Ensemble Project: A Community Resource for Studying Climate Change in the Presence of Internal Climate Variability. *Bulletin of the American Meteorological Society*, **96**, 1333–1349, doi:10.1175/BAMS-D-13-00255.1.
- Kay, J. E., B. R. Hillman, S. A. Klein, Y. Zhang, B. Medeiros, R. Pincus, A. Gettelman, B. Eaton, J. Boyle, R. Marchand, and T. P. Ackerman, 2012: Exposing global cloud biases in the Community Atmosphere Model (CAM) using satellite observations

and their corresponding instrument simulators. *Journal of Climate*, **25**, 5190–5207, doi:10.1175/JCLI-D-11-00469.1.

Kay, J. E., T. L’Ecuyer, A. Gettelman, G. Stephens, and C. O’Dell, 2008: The contribution of cloud and radiation anomalies to the 2007 Arctic sea ice extent minimum. *Geophysical Research Letters*, **35**, 1–5, doi:10.1029/2008GL033451.

Kay, J. E., T. L’Ecuyer, A. Pendergrass, H. Chepfer, R. Guzman, and V. Yettella, 2018: Scale-aware and definition-aware evaluation of modeled near-surface precipitation frequency using cloudsat observations. *Journal of Geophysical Research: Atmospheres*, **123**, 4294–4309, doi:10.1002/2017JD028213.

URL <https://agupubs.onlinelibrary.wiley.com/doi/abs/10.1002/2017JD028213>

Kay, J. E., C. Wall, V. Yettella, B. Medeiros, C. Hannay, P. Caldwell, and C. Bitz, 2016b: Global climate impacts of fixing the Southern Ocean shortwave radiation bias in the Community Earth System Model (CESM). *Journal of Climate*, 0–53, doi:10.1017/CBO9781107415324.004.

Knutti, R., D. Masson, and A. Gettelman, 2013: Climate model genealogy: Generation cmip5 and how we got there. *Geophysical Research Letters*, **40**, 1194–1199, doi:10.1002/grl.50256.

URL <https://agupubs.onlinelibrary.wiley.com/doi/abs/10.1002/grl.50256>

Knutti, R. and J. Sedláček, 2012: Robustness and uncertainties in the new cmip5 climate model projections. *Nature Climate Change*, **3**, 369 EP –.

URL <https://doi.org/10.1038/nclimate1716>

Korolev, A. V., G. A. Isaac, and J. Hallett, 1999: Ice particle habits in arctic clouds. *Geophysical Research Letters*, **26**, 1299–1302, doi:10.1029/1999GL900232.

URL <https://agupubs.onlinelibrary.wiley.com/doi/abs/10.1029/1999GL900232>

Kulie, M. S., R. Bennartz, T. J. Greenwald, Y. Chen, and F. Weng, 2010: Uncertainties in microwave properties of frozen precipitation: Implications for remote sensing and data assimilation. *Journal of the Atmospheric Sciences*, **67**, 3471–3487, doi:10.1175/2010JAS3520.1.

L’Ecuyer, T. and J. Jiang, 2010: Touring the atmosphere aboard the a-train. *Physics Today*, **63**, doi:10.1063/1.3653856.

L’Ecuyer, T. S., H. K. Beaudoin, M. Rodell, W. Olson, B. Lin, S. Kato, C. A. Clayson, E. Wood, J. Sheffield, R. Adler, G. Huffman, M. Bosilovich, G. Gu, F. Robertson, P. R. Houser, D. Chambers, J. S. Famiglietti, E. Fetzer, W. T. Liu, X. Gao, C. A. Schlosser, E. Clark, D. P. Lettenmaier, and K. Hilburn, 2015: The observed state of the energy budget in the early twenty-first century. *Journal of Climate*, **28**, 8319–8346, doi:10.1175/JCLI-D-14-00556.1.

L’Ecuyer, T. S., Y. Hang, A. V. Matus, and Z. Wang, 2019: Reassessing the effect of cloud type on earth’s energy balance in the age of active spaceborne observations. part i: Top

of atmosphere and surface. *Journal of Climate*, **32**, 6197–6217, doi:10.1175/JCLI-D-18-0753.1.

URL <https://doi.org/10.1175/JCLI-D-18-0753.1>

L’Ecuyer, T. S., N. B. Wood, T. Haladay, G. L. Stephens, and P. W. Stackhouse, 2008: Impact of clouds on atmospheric heating based on the r04 cloudsat fluxes and heating rates data set. *Journal of Geophysical Research: Atmospheres*, **113**, n/a–n/a, doi:10.1029/2008JD009951, d00A15.

Lenaerts, J. T. M., M. D. Camron, and J. E. Kay, 2019a: Present-day and future greenland ice sheet precipitation frequency from satellite observations and an earth system model. *in prep.*

Lenaerts, J. T. M., A. Gettelman, K. Van Tricht, L. van Kampenhout, and N. B. Miller, 2019b: Impact of cloud physics on the greenland ice sheet surface climate: a study with the community atmosphere model. *Journal of Geophysical Research: Atmospheres*, **submitted**.

Liu, G. and J. Curry, 1997: Precipitation characteristics in greenland-iceland-norwegian seas determined by using satellite microwave data. *Journal of Geophysical Research: Atmospheres*, **102**, 13987–13997, doi:10.1029/96JD03090.

URL <https://agupubs.onlinelibrary.wiley.com/doi/abs/10.1029/96JD03090>

Liu, X., S. Xie, J. Boyle, S. A. Klein, X. Shi, Z. Wang, W. Lin, S. J. Ghan, M. Earle, P. S. K. Liu, and A. Zelenyuk, 2011: Testing cloud microphysics parameterizations

in NCAR CAM5 with ISDAC and M-PACE observations. *Journal of Geophysical Research*, **116**, D00T11, doi:10.1029/2011JD015889.

Maahn, M., C. Burgard, S. Crewell, I. V. Gorodetskaya, S. Kneifel, S. Lhermitte, K. Van Tricht, and N. P. M. Van Lipzig, 2014: How does the spaceborne radar blind zone affect derived surface snowfall statistics in polar regions? *Journal of Geophysical Research D: Atmospheres*, **119**, 13604–13620, doi:10.1002/2014JD022079.

Manabe, S. and R. J. Stouffer, 1980: Sensitivity of a global climate model to an increase of co2 concentration in the atmosphere. *Journal of Geophysical Research: Oceans*, **85**, 5529–5554, doi:https://doi.org/10.1029/JC085iC10p05529.

Marchand, R., G. G. Mace, T. Ackerman, and G. Stephens, 2008: Hydrometeor detection using Cloudsat - An earth-orbiting 94-GHz cloud radar. *Journal of Atmospheric and Oceanic Technology*, **25**, 519–533, doi:10.1175/2007JTECHA1006.1.

Matus, A. V. and T. S. L'Ecuyer, 2017: The role of cloud phase in earth's radiation budget. *Journal of Geophysical Research: Atmospheres*, **122**, 2559–2578, doi:10.1002/2016JD025951.

URL <https://agupubs.onlinelibrary.wiley.com/doi/abs/10.1002/2016JD025951>

McIlhattan, E. A., 2016: *Powder Days in the Arctic: A proposed physical mechanism behind a known model bias*. Master's thesis, University of Wisconsin - Madison, Madison, WI, USA.

- McIlhattan, E. A., T. S. L'Ecuyer, and N. B. Miller, 2017: Observational evidence linking arctic supercooled liquid cloud biases in cesm to snowfall processes. *Journal of Climate*, **30**, 4477–4495, doi:10.1175/JCLI-D-16-0666.1.
- Milani, L., M. S. Kulie, D. Casella, S. Dietrich, T. S. L'Ecuyer, G. Panegrossi, F. Porcù, P. Sanò, and N. B. Wood, 2018: CloudSat snowfall estimates over Antarctica and the Southern Ocean: An assessment of independent retrieval methodologies and multi-year snowfall analysis. *Atmospheric Research*, **213**, 121–135, doi:10.1016/j.atmosres.2018.05.015.
- Milani, L., F. Porcù, D. Casella, S. Dietrich, G. Panegrossi, M. Petracca, and P. Sanò, 2015: Analysis of long-term precipitation pattern over Antarctica derived from satellite-borne radar. *The Cryosphere Discussions*, **9**, 141–182, doi:10.5194/tcd-9-141-2015.
URL <http://www.the-cryosphere-discuss.net/9/141/2015/>
- Miller, N. B., M. D. Shupe, C. J. Cox, V. P. Walden, D. D. Turner, and K. Steffen, 2015: Cloud Radiative Forcing at Summit, Greenland. *Journal of Climate*, **28**, 6267–6280, doi:10.1175/JCLI-D-15-0076.1.
- Moran, K. P., B. E. Martner, M. J. Post, R. A. Kropfli, D. C. Welsh, and K. B. Widener, 1998: An unattended cloud-profiling radar for use in climate research. *Bulletin of the American Meteorological Society*, **79**, 443–456, doi:10.1175/1520-0477(1998)079<0443:AUCPRF>2.0.CO;2.
- Morrison, A. L., J. E. Kay, H. Chepfer, R. Guzman, and V. Yettella, 2018: Isolating the liquid cloud response to recent arctic sea ice variability using spaceborne

lidar observations. *Journal of Geophysical Research: Atmospheres*, **123**, 473–490, doi:10.1002/2017JD027248.

URL <https://agupubs.onlinelibrary.wiley.com/doi/abs/10.1002/2017JD027248>

Morrison, H., G. de Boer, G. Feingold, J. Harrington, M. D. Shupe, and K. Sulia, 2012: Resilience of persistent Arctic mixed-phase clouds. *Nature Geoscience*, **5**, 11–17, doi:10.1038/ngeo1332.

Mouginot, J., E. Rignot, A. A. Bjørk, M. van den Broeke, R. Millan, M. Morlighem, B. Noël, B. Scheuchl, and M. Wood, 2019: Forty-six years of greenland ice sheet mass balance from 1972 to 2018. *Proceedings of the National Academy of Sciences*, **116**, 9239–9244, doi:10.1073/pnas.1904242116.

URL <https://www.pnas.org/content/116/19/9239>

Norin, L., A. Devasthale, T. S. L'Ecuyer, N. B. Wood, and M. Smalley, 2015: Inter-comparison of snowfall estimates derived from the CloudSat Cloud Profiling Radar and the ground-based weather radar network over Sweden. *Atmospheric Measurement Techniques*, **8**, 5009–5021, doi:10.5194/amt-8-5009-2015.

Onarheim, I. H., T. Eldevik, L. H. Smedsrud, and J. C. Stroeve, 2018: Seasonal and regional manifestation of arctic sea ice loss. *Journal of Climate*, **31**, 4917–4932, doi:10.1175/JCLI-D-17-0427.1.

URL <https://doi.org/10.1175/JCLI-D-17-0427.1>

- Palerme, C., C. Claud, N. B. Wood, T. L'Ecuyer, and C. Genthon, 2019: How Does Ground Clutter Affect CloudSat Snowfall Retrievals over Ice Sheets? *IEEE Geoscience and Remote Sensing Letters*, **16**, 342–346, doi:10.1109/LGRS.2018.2875007.
- Palerme, C., C. Genthon, C. Claud, J. Kay, N. B. Wood, and T. L'Ecuyer, 2016: Evaluation of current and projected antarctic precipitation in cmip5 models. *Climate Dynamics*, **48**, doi:10.1007/s00382-016-3071-1.
- Palerme, C., J. Kay, C. Genthon, T. L'Ecuyer, N. B. Wood, and C. Claud, 2014: How much snow falls on the antarctic ice sheet? *The Cryosphere*, **8**, doi:10.5194/tc-8-1577-2014.
- Pettersen, C., R. Bennartz, M. S. Kulie, A. J. Merrelli, M. D. Shupe, and D. D. Turner, 2016: Microwave signatures of ice hydrometeors from ground-based observations above summit, greenland. *Atmospheric Chemistry and Physics*, **16**, 4743–4756, doi:10.5194/acp-16-4743-2016.
URL <https://www.atmos-chem-phys.net/16/4743/2016/>
- Pettersen, C., R. Bennartz, A. J. Merrelli, M. D. Shupe, D. D. Turner, and V. P. Walden, 2018: Precipitation regimes over central greenland inferred from 5 years of icecaps observations. *Atmospheric Chemistry and Physics*, **18**, 4715–4735, doi:10.5194/acp-18-4715-2018.
URL <https://www.atmos-chem-phys.net/18/4715/2018/>
- Pettersen, C. and A. Merrelli, 2018: Microwave radiometer snow categorization tool for summit, greenland, 2010 - 2015. *Arctic Data Center*, doi:10.18739/A2R28Q.

Petty, G. W., 2006: *A First Course in Atmospheric Radiation*. Sundog Publishing, second edition edition, 458 pp.

Pithan, F., B. Medeiros, and T. Mauritsen, 2014: Mixed-phase clouds cause climate model biases in Arctic wintertime temperature inversions. *Climate Dynamics*, **43**, 289–303.

Rogers, J. C., D. J. Bathke, E. Mosley-Thompson, and S.-H. Wang, 2004: Atmospheric circulation and cyclone frequency variations linked to the primary modes of greenland snow accumulation. *Geophysical Research Letters*, **31**, doi:10.1029/2004GL021048.

URL <https://agupubs.onlinelibrary.wiley.com/doi/abs/10.1029/2004GL021048>

Schuenemann, K. C., J. J. Cassano, and J. Finnis, 2009: Synoptic Forcing of Precipitation over Greenland: Climatology for 1961-99. *Journal of Hydrometeorology*, **10**, 60–78, doi:10.1175/2008jhm1014.1.

Schuur, E. A. G., A. D. McGuire, C. Schädel, G. Grosse, J. W. Harden, D. J. Hayes, G. Hugelius, C. D. Koven, P. Kuhry, D. M. Lawrence, S. M. Natali, D. Olefeldt, V. E. Romanovsky, K. Schaefer, M. R. Turetsky, C. C. Treat, and J. E. Vonk, 2015: Climate change and the permafrost carbon feedback. *Nature*, **520**, 171 EP –.

URL <https://doi.org/10.1038/nature14338>

Serreze, M. C. and A. P. Barrett, 2008: The summer cyclone maximum over the central arctic ocean. *Journal of Climate*, **21**, 1048–1065, doi:10.1175/2007JCLI1810.1.

- Serreze, M. C. and R. G. Barry, 2011: Processes and impacts of Arctic amplification: A research synthesis. *Global and Planetary Change*, **77**, 85–96, doi:10.1016/j.gloplacha.2011.03.004.
- Shupe, M. D., 2011: Clouds at arctic atmospheric observatories. Part II: Thermodynamic phase characteristics. *Journal of Applied Meteorology and Climatology*, **50**, 645–661, doi:10.1175/2010JAMC2468.1.
- Shupe, M. D., D. D. Turner, V. P. Walden, R. Bennartz, M. P. Cadetdu, B. B. Castellani, C. J. Cox, D. R. Hudak, M. S. Kulie, N. B. Miller, R. R. Neely, W. D. Neff, and P. M. Rowe, 2013: High and dry: New observations of tropospheric and cloud properties above the greenland ice sheet. *Bulletin of the American Meteorological Society*, **94**, 169–186.
URL <http://www.jstor.org/stable/26219494>
- Skofronick-Jackson, G., M. Kulie, L. Milani, S. J. Munchak, N. B. Wood, and V. Levizzani, 2019: Satellite estimation of falling snow: A global precipitation measurement (gpm) core observatory perspective. *Journal of Applied Meteorology and Climatology*, **58**, 1429–1448, doi:10.1175/JAMC-D-18-0124.1.
- Souvereinjs, N., A. Gossart, S. Lhermitte, I. V. Gorodetskaya, J. Grazioli, A. Berne, C. Duran-Alarcon, B. Boudevillain, C. Genthon, C. Scarchilli, and N. P. M. van Lipzig, 2018: Evaluation of the cloudsat surface snowfall product over antarctica using ground-based precipitation radars. *The Cryosphere*, **12**, 3775–3789, doi:10.5194/tc-12-3775-2018.

URL <https://www.the-cryosphere.net/12/3775/2018/>

Steffen, K. and J. Box, 2001: Surface climatology of the Greenland Ice Sheet: Greenland Climate Network 1995-1999. *Journal of Geophysical Research*, **106**, 33951, doi:10.1029/2001JD900161.

Stephens, G. L., T. L'Ecuyer, R. Forbes, A. Gettelmen, J.-C. Golaz, A. Bodas-Salcedo, K. Suzuki, P. Gabriel, and J. Haynes, 2010: Dreary state of precipitation in global models. *Journal of Geophysical Research: Atmospheres*, **115**, doi:10.1029/2010JD014532.

URL <https://agupubs.onlinelibrary.wiley.com/doi/abs/10.1029/2010JD014532>

Stephens, G. L., J. Li, M. Wild, C. A. Clayson, N. Loeb, S. Kato, T. L'Ecuyer, P. W. Stackhouse, M. Lebsock, and T. Andrews, 2012: An update on Earth's energy balance in light of the latest global observations. *Nature Geoscience*, **5**, 691–696, doi:10.1038/ngeo1580.

URL <http://dx.doi.org/10.1038/ngeo1580>

Stroeve, J. and D. Notz, 2015: Insights on past and future sea-ice evolution from combining observations and models. *Global and Planetary Change*, **135**, 119 – 132, doi:<https://doi.org/10.1016/j.gloplacha.2015.10.011>.

URL <http://www.sciencedirect.com/science/article/pii/S092181811530093X>

Tan, I. and T. Storelvmo, 2016: Sensitivity Study on the Influence of Cloud Microphysical Parameters on Mixed-Phase Cloud Thermodynamic Phase Partitioning in CAM5. *Journal of the Atmospheric Sciences*, **73**, 709–728, doi:10.1175/JAS-D-15-0152.1.

- Tanelli, S., S. L. Durden, E. Im, K. S. Pak, D. G. Reinke, P. Partain, J. M. Haynes, and R. T. Marchand, 2008: Cloudsat's cloud profiling radar after two years in orbit: Performance, calibration, and processing. *IEEE Transactions on Geoscience and Remote Sensing*, **46**, 3560–3573, doi:10.1109/TGRS.2008.2002030.
- Terai, C. R., P. M. Caldwell, S. A. Klein, Q. Tang, and M. L. Branstetter, 2018: The atmospheric hydrologic cycle in the ACME v0.3 model. *Climate Dynamics*, **50**, 3251–3279, doi:10.1007/s00382-017-3803-x.
- Trenberth, K. E., J. T. Fasullo, and J. Kiehl, 2009: Earth's global energy budget. *Bulletin of the American Meteorological Society*, **90**, 311–323, doi:10.1175/2008BAMS2634.1.
- van den Broeke, M. R., E. M. Enderlin, I. M. Howat, P. Kuipers Munneke, B. P. Y. Noël, W. J. van de Berg, E. van Meijgaard, and B. Wouters, 2016: On the recent contribution of the greenland ice sheet to sea level change. *The Cryosphere*, **10**, 1933–1946, doi:10.5194/tc-10-1933-2016.
URL <https://www.the-cryosphere.net/10/1933/2016/>
- Van Tricht, K., S. Lhermitte, J. T. M. Lenaerts, I. V. Gorodetskaya, T. S. L'Ecuyer, B. Noel, M. R. van den Broeke, D. D. Turner, and N. P. M. van Lipzig, 2016: Clouds enhance Greenland ice sheet meltwater runoff. *Nat Commun*, **7**, doi:10.1038/ncomms10266.
- Vaughan, D., J. Comiso, I. Allison, J. Carrasco, G. Kaser, R. Kwok, P. Mote, T. Murray, F. Paul, J. Ren, E. Rignot, O. Solomina, K. Steffen, and T. Zhang, 2013: *Observations: Cryosphere*, Cambridge University Press, Cambridge, United Kingdom and New York,

NY, USA, book section 4. 317–382.

URL www.climatechange2013.org

Vernon, C. L., J. L. Bamber, J. E. Box, M. R. van den Broeke, X. Fettweis, E. Hanna, and P. Huybrechts, 2013: Surface mass balance model intercomparison for the greenland ice sheet. *The Cryosphere*, **7**, 599–614, doi:10.5194/tc-7-599-2013.

URL <https://www.the-cryosphere.net/7/599/2013/>

Vihma, T., J. Screen, M. Tjernström, B. Newton, X. Zhang, V. Popova, C. Deser, M. Holland, and T. Prowse, 2016: The atmospheric role in the Arctic water cycle: A review on processes, past and future changes, and their impacts. *Journal of Geophysical Research G: Biogeosciences*, **121**, 586–620, doi:10.1002/2015JG003132.

Vonder Haar, T. H. and V. E. Suomi, 1971: Measurements of the Earth's Radiation Budget from Satellites During a Five-Year Period. Part I: Extended Time and Space Means. *Journal of the Atmospheric Sciences*, **28**, 305–314, doi:10.1175/1520-0469(1971)028<0305:MOTERB>2.0.CO;2.

URL [http://journals.ametsoc.org/doi/abs/10.1175/1520-0469\(1971\)028<0305:MOTERB>2.0.CO;2](http://journals.ametsoc.org/doi/abs/10.1175/1520-0469(1971)028<0305:MOTERB>2.0.CO;2)

Wang, P. K., 2013: *Physics and Dynamics of Clouds and Precipitation*. Cambridge University Press, 1ed edition.

Wang, Z., D. Vane, and G. Stephens, 2012: Level 2 combined radar and lidar cloud scenario classification product process description and interface control document. *NASA JPL CloudSat project document Version 1.0, 61 pp.*

Wielicki, B. A., B. R. Barkstrom, E. F. Harrison, R. B. Lee, G. L. Smith, and J. E.

Cooper, 1996: Clouds and the earth's radiant energy system (ceres): An earth observing system experiment. *Bulletin of the American Meteorological Society*, **77**, 853–868, doi:10.1175/1520-0477(1996)077<0853:CATERE>2.0.CO;2.

URL [https://doi.org/10.1175/1520-0477\(1996\)077<0853:CATERE>2.0.CO;2](https://doi.org/10.1175/1520-0477(1996)077<0853:CATERE>2.0.CO;2)

Winker, D. M., W. H. Hunt, and M. J. McGill, 2007: Initial performance assessment of caliop. *Geophysical Research Letters*, **34**, doi:10.1029/2007GL030135.

URL <https://agupubs.onlinelibrary.wiley.com/doi/abs/10.1029/2007GL030135>

Wood, N. B. and T. S. L'Ecuyer, 2018: Level 2C Snow Profile Process Description and Interface Control Document, Product Version, P1_R05. *NASA JPL CloudSat project document revision 0, 26 pp.*

URL http://www.cloudsat.cira.colostate.edu/sites/default/files/products/files/2C-SNOW-PROFILE_PDICD.P1_R05.rev0_.pdf

Zhang, X., J. E. Walsh, J. Zhang, U. S. Bhatt, and M. Ikeda, 2004: Climatology and interannual variability of arctic cyclone activity: 1948–2002. *Journal of Climate*, **17**, 2300–2317, doi:10.1175/1520-0442(2004)017<2300:CAIVOA>2.0.CO;2.

Zwally, H. J., M. B. Giovinetto, M. A. Beckley, and J. L. Saba, 2012: Antarctic and greenland drainage systems, gsfc cryospheric sciences laboratory.

URL http://icesat4.gsfc.nasa.gov/cryo_data/ant_grn_drainage_systems.php

Zwally, H. J., J. Li, A. C. Brenner, M. Beckley, H. G. Cornejo, J. D. Marzio, M. B. Giovinetto, T. A. Neumann, J. Robbins, J. L. Saba, D. Yi, and W. Wang, 2011: Greenland ice sheet mass balance: Distribution of increased mass loss with climate warming; 2003-07 versus 1992-2002. *Journal of Glaciology*, **57**, 88–102, doi:10.3189/002214311795306682.